UNDERSTANDING OF NO-LOAD POWER IN LOW CONSISTENCY REFINING

by

Nina Rajabi Nasab

B.Sc., Sharif University of Technology, Tehran, Iran, 2005
M.Sc., Chalmers University of Technology, Goteborg, Sweden, 2007

A THESIS SUBMITTED IN PARTIAL FULFILLMENT OF
THE REQUIREMENTS FOR THE DEGREE OF

DOCTOR OF PHILOSOPHY

in

The Faculty of Graduate and Postdoctoral Studies

(Mechanical Engineering)

THE UNIVERSITY OF BRITISH COLUMBIA
(Vancouver)

August 2013

Abstract

Low Consistency (LC) refining is the primary means of improving the strength and smoothness of paper by imparting energy to fibres through repeated fibre-bar interactions. The useful part of the energy modifies the morphology of the fibres and the remaining, no-load power, mainly overcomes the hydraulic, pumping and mechanical losses in the refiner. This thesis is aimed to explore the no-load power in LC refining both experimentally and computationally. The contribution of this thesis comes in three parts.

Firstly, the effect of consistency, operational and plate design parameters on no-load power was experimentally determined on two pilot scale LC refiners with different plate diameters. The obtained data were used to provide a statistical model for prediction of no-load power. To study the effect of diameter and groove depth, the no-load power consumption of some mills corresponding to their operating conditions, and the specifications of the relevant refiner discs were collected. Based on this model, no-load power is described in terms of two main components, hydraulic and pumping powers, and an empirical equation is proposed.

Secondly, we numerically examined the two-dimensional flow of a Newtonian fluid in the gap formed between two opposing cavities which represent the cross-sectional flow in LC refiner. A large number of unsteady simulations were conducted to characterize the effect of gap size on the flow field over the range of velocities. Then, we examined material transport between the cavities by introducing a passive scalar to

represent the motion of tracer particles. Over the range of parameters studied, we identify two characteristic flow fields, defined as either steady or unsteady. We also find that particles are transported to the region near the leading edges of the bars only under the conditions of unsteady flow.

Thirdly, we extended the numerical study by characterizing the effect of cavity depth on the flow field over the range of velocities. We find that the aspect ratio of the cavity dictates three characteristic flow fields based on the number of vortices formed within cavity and we propose criteria for cavity aspect ratio in terms of the refiner application.

Preface

In this section, we briefly explain the contents of the papers that have been accepted, submitted or will be submitted for publication from this thesis and clarify the contributions of co-authors in the papers. We also include the list of conference contributions.

Journal Papers

- **Rajabi Nasab, N.**, Olson, J.A., Heymer, J. & Martinez, D.M. (2013) Understanding of No-load Power in Low Consistency Refiners. Canadian Journal of Chemical Engineering.

  This publication has focused on understanding the no-load power in Low Consistency refiners using experiments. Chapter 3 includes the contents of this publication. The author of the thesis was the principal contributor to this publication. Dr. Jens Heymer has designed the experimental flow loop and assisted with writing the paper. Professors James Olson and Mark Martinez supervised the research and assisted with writing the paper.

- **Rajabi Nasab, N.**, Mithrush, T., Olson, J.A. & Martinez, D.M. (2013), Turbulent flow between two parallel corrugated walls: The case with motion of one wall perpendicular to the corrugation cavities, Submitted.

  In this publication, we present results of a computational study of the flow field in the cross section of refiner. Chapter 4 includes the contents of this

publication. The author of this thesis was the principal contributor to this publication. T. Mithrush assisted with the simulations and Professors James Olson and Mark Martinez supervised the research. All the co-authors assisted with writing the paper.

Contributions to refereed conference proceedings

- **Rajabi Nasab, N.**, J.A. Olson, J. Heymer & D.M. Martinez, "Experimental Study of Low Consistency Refiner No-load Power", PAPERCON Conference Proceedings, New Orleans, LA, April 21-25, pp. 1539-1551 (2012).

Conference posters

- **Rajabi Nasab, N.**, Mithrush, T., Olson, J.A. & Martinez, D.M., "Insight into the Flow Field of LC Refiners: The Relationship to the Beating Effect", January 29-31, Are, Sweden (2013).

- **Rajabi Nasab, N.**, Olson, J.A. & Martinez, D.M., "Understanding no-load power in LC refining", PacWest Conference, June 10-13, Sun Peaks, BC, Canada (2009)

- **Rajabi Nasab, N.**, Olson, J.A. & Martinez, D.M., "Understanding no-load power in LC refining", Pulp and Paper Technical Association of Canada (PAPTAC) Conference, February 4-5, Montreal, Canada (2009)

- **Rajabi Nasab, N.**, Olson, J.A.& Martinez, D.M., "Understanding no-load power in LC refining", Pulp and Paper Technical Association of Canada (PAPTAC) Conference, February 5-7, Montreal, Canada (2008)

Table of Contents

Appendices

List of Tables

List of Figures

Nomenclature

Symbols

A, K	Constant values depend on inner and outer diameters, and also bars and grooves geometry
A^*	Normalized bar crossing area
B	Bar width, mm
BEL	Bar edge length, km/rev
C	Consistency of pulp, %
C_q	Dimensionless flow rate, $\frac{Q}{\omega {R_o}^3}$
D_i	Inner diameter of disc
D_o	Outer diameter of disc
G	Gap between rotor and stator, mm
G^*	Dimensionless gap, G/R_o
k	the height of roughness
k_1, k_2	Empirical constants
L	Cavity pitch, $B + W$
M	Constant value which covers sector and bar angles
N	Number of grid points
P_n	No-load power number, $\frac{Power_n}{\rho\omega^3 {R_o}^5}$
${P_n}^*$	Hydraulic power number, $\frac{{Power_n}^*}{\rho\omega^3 {R_o}^5}$

$Power_M$	Mechanical loss, kW
$Power_n$	Total no-load power excluding mechanical loss, kW
$Power_n{}^*$	Hydraulic no-load power, kW
$Power_{NL}$	Total no-load power, kW
$Power_P$	Pumping no-load Power, kW
$Power_r$	Refining power, kW
$Power_t$	Total power, kW
Q	Flow rate, lpm
R_i	Inner radius of disc
R_o	Outer radius of disc
Re	Reynolds number, $\frac{\omega {R_o}^2}{\nu}$
Re_l	Reynolds number based on the cavity pitch, $\frac{UL}{\nu}$
T	Groove depth, mm
U	Velocity of moving wall, m/s
W	Groove width, mm

Greek

α	Correlation constant
β^*	Ratio of the rotational speed of core flow between rotor and stator to the rotational speed of rotor
λ_{turb}	Empirical turbulent flow parameter, $C_q Re^{\frac{1}{5}}$
ϕ	Bar angle, [°]
θ	Sector angle, [°]
ω	Rotational speed, rpm

Acknowledgments

In the first place, I would like to express my sincere gratitude to my supervisors, Professor James A. Olson and Professor D. Mark Martinez for their leadership and continual support during my research. Above all and the most needed, they provided me support and friendly help in various ways. I am deeply grateful to Professor Richard J. Kerekes for his guidance, suggestions and valuable discussions throughout the course of this research.

In addition, I am deeply thankful to Dr. Ali Vakil for his helpful discussions and critical comments. His passion for scientific problems has taught me a lot.

I would like to thank my colleagues and the staff at the Pulp and Paper Center for their valuable insights on the various works we did together, specially Ali Elahimehr, Dr. Pirooz Darabi and Dr. Jens Heymer. This work would not be done without the help of George Soong.

I gratefully acknowledge financial support of the Natural Sciences and Engineering Research Council of Canada through the Collaborative Research and Development program and through the support of our partners BC Hydro, FP Innovations, Catalyst Papers, Howe Sound Pulp and Paper, West Fraser Quesnel River Pulp, Canfor, Andritz, Arkema, Honeywell, WestCan Engineering, Advanced Fiber Technologies, Ontario Power Authority and CEATI international.

I am grateful to my committee members Professor Richard J. Kerekes, Dr. Dana Grecov and Dr. Rodger Beatson for their great comments and input about my re-

search.

And finally, I would like to specially thank:

- My brother, Mazdak: Thanks for your unconditional love. You are the best gift of my life. No matter how far we are apart, I never stop loving, missing and caring about you.

- My husband, Farzad: Thanks for your love, patience and kindness. Thank you for always being by my side and for giving me the sweetest moments of my life. You are a constant comfort to me.

Dedication

To my parents,

Mahnaz & Mansour

for their endless love and support;

Chapter 1

Introduction

During the mechanical pulping process, multiple stages of high consistency (HC) refiners are used to convert wood chips into fibres. Pre-washed wood chips are fed into the HC refiners at a consistency of $20-40\%$, and are broken into individual fibres by the forces imposed by the bars of the opposing rotor and stator surfaces. Consistency is defined as the ratio of the mass of fibres to the total mass of pulp suspension. The refining action is continued further by a low consistency (LC) refiner after diluting the pulp suspension to a consistency of about $3-4\%$. A mechanical process where fibres are treated at consistencies under 6% is defined as low consistency (LC) refining [1, 2].

HC refining is an energy intensive process. About 60% of the total electrical energy in mechanical pulping process is consumed by the HC refiners [3]. To reduce energy consumption, mechanical pulp producers are increasingly using energy efficient LC refining to offset the total energy consumed in the process. However, LC refiners, unlike HC refiners, have substantial no-load power, that is, the power to mostly overcome the hydraulic, pumping and mechanical losses in the refiner. At best, the no-load power is 20% of the total applied power and depending on the refiner technology, can be as high as 50% for larger refiners [4, 5, 6]. Understanding the no-load power and how it is consumed during refining is the first step in enhancing the refining efficiency. Finding ways to decrease the no-load power would allow more energy to be transferred to the fibres thus increasing net LC refining power.

In this work, a new correlation to estimate the no-load power in the LC refining is presented. The proposed correlation provides guidelines to evaluate the effect of both operational and geometrical parameters on the no-load power. In addition, a series of numerical simulations are presented which obtain detailed insight into the LC refiner flow field. This methodology helps to better understand the no-load power.

This thesis is presented in 5 chapters. The motivation for this work is given in chapter 1. Chapter 2 introduces LC refiners, no-load power and flow fields in LC refiners and more relevant literature in details. Following this, Chapter 3 presents the experimental methodology that leads to better understand the no-load power in LC refiner and the affecting parameters. In chapters 4 and 5, the numerical methodology is explained that results to explore the flow field in the cross section of refiner. The highlights of this work are summarized in Chapter 6 as well as recommendations for future research.

Chapter 2

Background

In this thesis, we study the no-load power consumed in low consistency (LC) refiners in an attempt to minimize it. It is evident that the subject area, although quite specialized, touches on many related areas and as such, are reviewed in this chapter. First, we introduce LC refiner in §2.1 and survey the literature on no-load power. Then, we provide an overview of studies related to the power consumption due to the flow field between roughened rotor-stator discs in §2.2. The flow field in refiner is similar to the flow field between two roughened rotating discs, which have been studied in detail, both experimentally and numerically.

Moreover, there are numerous works that considered the turbulent flow in the channel formed between two periodic corrugated walls which resembles the cross-sectional flow field of refiner. To better understand the flow field inside the refiner, in §2.3, we try to summarise only those that appear to be most relevant.

2.1 Low consistency refiner

LC refiners are mechanical devices employed to modify papermaking fibre morphology. They are rotary devices having bar patterns on both the rotor and stator (Figure 2.1). The rotor and stator are either disc or conical in shape and, during refining, are separated by a gap of about three-ten fibre diameters. Papermaking fibres are pumped axially through the hub of the stator, flow radially through the grooves of

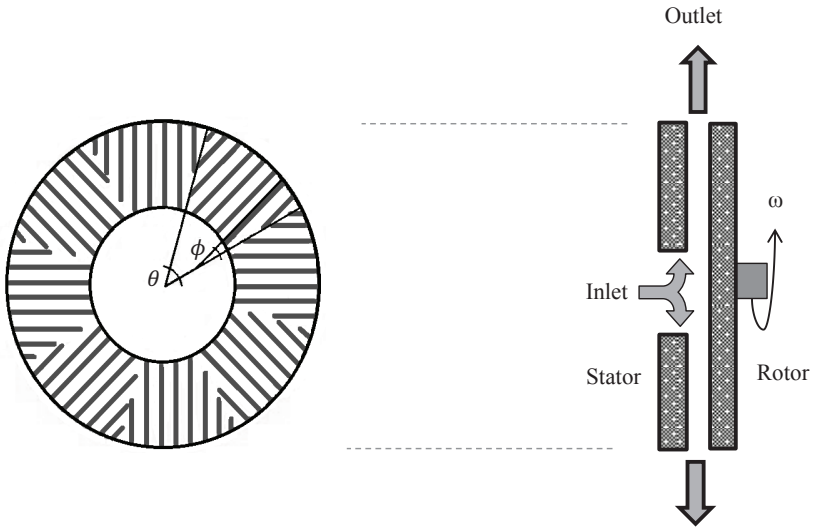

(a)

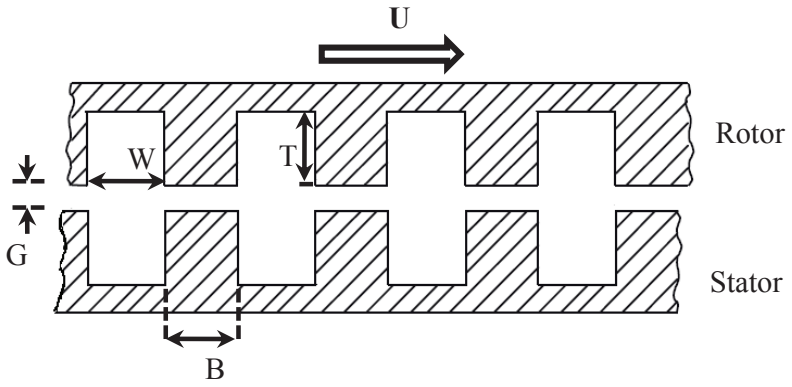

(b)

Figure 2.1: (a) Illustration of the configuration of a LC disc refiner and schematic of the grinding surface of an LC disc refiner. One disc is stationary in which a dilute papermaking fibre suspension is fed into the machine. Patterns are machined on to the surface of the plate. (b) cross section of the topography

the discs, and are trapped between bars in the narrow gap between the rotor and stator. The fibres are "beaten" or "refined" by repeated impacts with the bars. They then leave the refiner radially and are subjected to further processing. Comprehensive details regarding the action of refiners on the changes in morphology of the papermaking fibre can be found in the review by Page [7].

This investigation focuses solely on disc refiners. Each disc is specified by a typical arrangement of bars and grooves with constant sectional and grinding angles. The main design parameters for disc refiners are inner and outer diameters (D_i, D_o), bar width (B), groove width (W), groove depth (T), sector angle (θ), and bar angle (ϕ). Plate designs are typically characterized by Bar Edge Length (BEL) which is the total length of bar during a single rotation of the refiner disc and is estimated using TAPPI standard TIP 0508-05 (1994). Later in 2009, Roux et al. [8] modified the definition proposed by TAPPI as follows:

$$BEL = (2\pi)^2 \left(\frac{{R_o}^3 - {R_i}^3}{3(W+B)^2} \right) \tag{2.1}$$

where R_o and R_i are the outer and inner radii of refiner disc, respectively.

LC refiners have substantial "no-load" power, that is, power to overcome the hydraulic, pumping and mechanical losses in the refiner. Generally, no-load power refers to the power used by the refiner for purposes other than changes in fibre morphology. Some researchers state that no-load power is the energy threshold at which the papermaking fibre undergoes changes in its morphology. Others define no-load power as the minimum energy required to rotate the rotor in a pulp suspension [9, 10]. Both definitions are correct, but clarity is needed to understand where each one plays a role.

To help distinguish these concepts, the schematic power curve of refining is shown

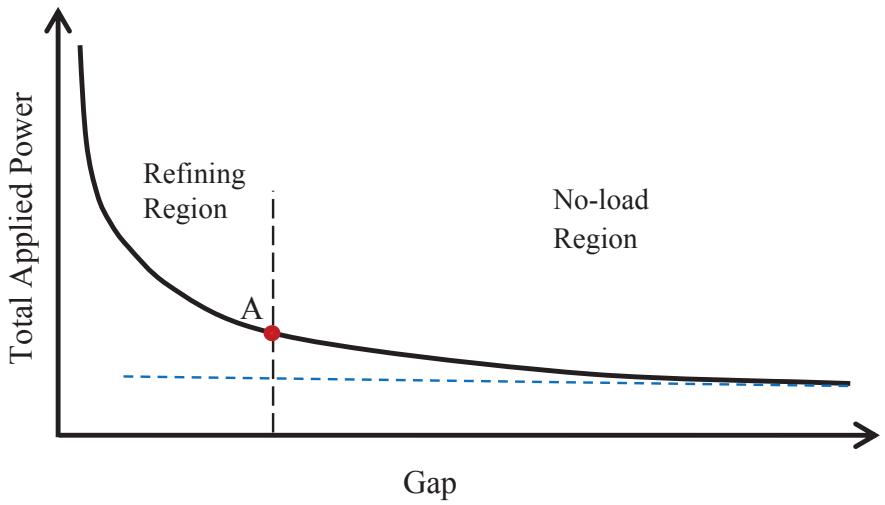

Figure 2.2: Schematic graph of power vs. gap size

in Figure 2.2. This figure can be interpreted according to the two different definitions of no-load power. The refining region is defined to be the region where energy increases rapidly with decreasing gap size. In this area the rapid increase in slope is caused by changes in fibre morphology. At the lower limit of this region, the point marked "A" is considered to be the no-load definition as determined by changes in fibre morphology, and is the starting point of refiner loading. The point of refiner loading, where the variations in pulp properties are evident, occurs at different gap sizes depending on pulp type [11]. As gap increases, the curve asymptotically approaches a constant value. This limit is defined to be the second definition of no-load power, i.e. the minimum energy required for free disc rotation in pulp suspension.

Based on these different definitions, no-load power can be measured either at the fully open position or at the smaller gaps with pulp [12, 13] or with water [14]. In industry, either the total applied power measured for a pulp suspension at a gap of $2.5\,mm$, which is close to point "A" on the right or the backed-off power is considered

to be the no-load power. As it is reported, the difference in no-load power obtained from each of these definitions can be as much as 35% [15].

Many authors have advanced scaling laws to correlate the power consumed to operating conditions in order to understand the mechanism of refining [16, 17, 18, 19, 5, 20, 21]. In essence, the following form has been proposed:

$$Power_t = Power_r + Power_{NL} \tag{2.2}$$

where $Power_t$ is the total power consumed, $Power_r$ is the net power consumed to modify the morphology of the fibre, and $Power_{NL}$ is the no-load power. Most of these researchers have separated no-load power into three different contributions:

- Hydraulic losses ($Power_n{}^*$): required energy to rotate the refiner disc in pulp suspension close to the stationary disc.
- Pumping losses ($Power_P$): required energy consumed by refiner when pumping pulp suspension from inlet to outlet of refiner.
- Mechanical losses ($Power_M$): loss due to shaft and bearings friction.

Based on this classification, a number of these research groups indicate that $Power_{NL}$ is related primarily to flow rate Q, rotational velocity ω , and the inner and outer diameters of the refiner plates, i.e. D_i and D_o, respectively. In 1967, Banks [22] proposed the following relationship to express the no-load power consumed by a disc refiner:

$$Power_{NL} = k_1\omega^3 {D_o}^5 + k_2\omega^2 {D_o}^2 + Power_M \tag{2.3}$$

where k_1 and k_2 are empirical constants and $Power_M$ represents the mechanical losses. The first term in Equation 2.3 represents the power losses due to the turbulent

rotating motion of the disc in the stock and the second term represents the power losses due to pumping effect. Subsequently, Herbert et al. [5] suggested a similar formula for no-load power; however, the pumping term has included volumetric flow rate, Q:

$$Power_{NL} = k_1\omega^3 \left({D_o}^5 - \frac{2}{3}{D_i}^5 \right) + k_2 Q \omega^2 {D_o}^2 + Power_M \tag{2.4}$$

The most recently used formula to calculate the no-load power in industry [23] is as follows, however this empirical formula does not dimensionally sound correct:

$$Power_{NL} = 102 \left(\frac{\omega}{100} \right)^3 \left(\frac{D_o}{100} \right)^{4.3} \left(\frac{2W}{W+B} \right) \left(\frac{T}{4} \right) \tag{2.5}$$

Other relationships can be found in review given by Ebeling [18]. What is clear from these proposed formulas and others found in the literature is that there is no evidence of gap dependency in no-load power, and not all of the important operating and design parameters are considered.

In a recent work, Batchelor et al. [24] showed the relationship between power and gap size. According to their study, shown schematically in Figure 2.2, by increasing the gap size, the applied power decreases and then approaches an asymptotic value at wide gaps. In their study, they proposed a negative exponential function to predict the net power and a linear function to estimate the no-load power respect to the gap size variations. For the smaller gaps, Luukkenen and Mohlin [25, 26, 27] demonstrate that the power is proportional to $1/G$.

These scaling laws however are rather incomplete as factors known to be important are not considered in these descriptions. Several studies have been undertaken in an attempt to understand how various parameters affect the operation of refiners and the amount of energy consumed in the refining process. Dietemann et al. [4] and Rihs [9]

found that increasing flow rate increases the no-load power slightly. Their work also introduced rotational speed as the main parameter and showed that no-load power is proportional to the rotational speed cubed.

Lundin [11] compared both mechanical and chemical pulp with water. Comparison of measured no-load power under similar operating conditions using water and mechanical pulp, in which the fibers are shorter than in chemical pulp, showed less than 10% change in the no-load power. Contrary to this, a significant difference was found between the no-load power of water and chemical pulp with long fibres. The same result has been reported by Dietemann et al. [4], Rihs [9] and Luukkenen [27]. In mechanical pulping the average length of fibres is shorter compared to chemical pulps and it is assumed to not influence the fluids turbulent viscosity. For long fibres pulps there can be an increase in power consumption due to the higher viscosity [28].

The refiner plate outer diameter has a significant effect on no-load power [5, 22]. Studies investigating the effect of groove depth showed that no-load power increased with deeper bars [29, 30]. In the most recent work, Dietemann et al. [4] postulate that the no-load power increases with increasing the number of bars and grooves on the plates.

2.2 Flow field between two rotating discs

In order to understand no-load power in refining, it is instructive to understand the flow field inside the rotor-stator system. A wide range of studies has been conducted on turbulent flow confined between both stationary and rotating discs enclosed by a shroud [31, 32, 33, 34] and Launder et al. [35] published an extensive review on this complex flow field.

In addition, a comprehensive theoretical and experimental study of the flow inside

Regime	Gap	Description	Best equation
Regime 1	Small	Laminar Flow, merged boundary layer	${P_n}^* = \pi G^* Re$
Regime 2	Large	Laminar Flow, separate boundary layer	${P_n}^* = 1.85 {G^*}^{\frac{1}{10}} Re^{-\frac{1}{2}}$
Regime 3	Small	Turbulent flow, merged boundary layer	${P_n}^* = 0.04 {G^*}^{-\frac{1}{6}} Re^{-\frac{1}{4}}$
Regime 4	Large	Turbulent flow, separate boundary layer	${P_n}^* = 0.051 {G^*}^{\frac{1}{10}} Re^{-\frac{1}{5}}$

Table 2.1: Different flow regimes inside an enclosed smooth rotor-stator

an enclosed rotor-stator system has been carried out by Daily and Nece [36, 37] for both smooth and rough surfaces. They have classified flow in four different regimes based on Reynolds number and gap size between two plates. In their study, torque data have been collected over a range of disc Reynolds numbers ($Re = \omega {R_o}^2/\nu$) from 10^3 to 10^7 for different gap sizes. It is worth mentioning that Reynolds number ranges from 10^6 to 5×10^7 for most refiners used in industry. Table 2.1 gives a brief description of all four flow regimes where ${P_n}^*$ is the dimensionless power number in the absence of pumping effects, and G^* represents the non-dimensional gap size. For a given G^*, all four regimes may or may not be experienced for the practical range of Reynolds number, Re.

They also reported a similar experiment for rough discs with relative roughnesses of $\frac{R_o}{k} \approx 1000, 2000$ and 3200 for three different gap sizes and for $4{\times}10^3 < Re < 6{\times}10^6$. k is the height of the roughness and R_o is the outer radius. The similar four flow regimes were that were originally obtained for smooth discs when roughness was added. It was reported that roughness had no significant effect on the ${P_n}^*$ in the laminar regimes (1) and (2); while in the turbulent regimes (3) and (4), ${P_n}^*$ increased as roughness increased. The point that the effects of roughness are apparent first has been approximated by the below expression:

$$Re\sqrt{{P_n}^*} = 0.55 \times 10^3 \left(\frac{R_o}{k}\right)^{2/5} \tag{2.6}$$

Beyond this critical Reynolds number, ${P_n}^*$ becomes greater than for corresponding smooth discs. The zone of fully rough flow starts from:

$$Re\sqrt{{P_n}^*} = 0.575 \times 10^4 \left(\frac{R_o}{k}\right)^{1/10} \tag{2.7}$$

and the suggested formula to predict ${P_n}^*$ at a fully rough flow zone is given by:

$$\frac{1}{\sqrt{{P_n}^*}} = 7.6log\left(\frac{R_o}{k}\right) - 4.8{G^*}^{\frac{1}{4}} \tag{2.8}$$

Daily et al. [38] looked into the effect of superposed radial outflow on the total power number (P_n) of a rotating disc and proposed the following expression for turbulent flow $2 \times 10^6 < Re < 10^7$ when outflow is small:

$$P_n = {P_n}^*(1 + 13.9\beta^*\lambda_{turb}{G^*}^{-\frac{1}{8}}) \tag{2.9}$$

In this formula, β^* is the ratio of the rotational speed of core flow between rotor and stator to the rotational speed of rotor. λ_{turb} is the empirical turbulent flow parameter which relates the superposed flow rate to the rotational speed. This parameter is defined by Owen and Rogers based on a 1/7-power-law assumption for the turbulent case: $\lambda_{turb} = C_q Re^{\frac{1}{5}}$ where $C_q = \frac{Q}{\omega {R_o}^3}$ is the non-dimensional flow rate [39, 33].

2.3 Turbulent flow between two parallel corrugated walls

Understanding the flow field in the cross section of LC refiners is difficult. The difficulty stems from the complexity of the moving boundary. There are a number of geometries in the literature which mimic aspects of the flow considered in LC refiners and insight into the industrial case can be gained by considering these first. We categorize these geometries into four groups which will be summarized below (see Figure 2.3). The major works for category I (see Figure 2.3a) are for *pressure-driven Stokes flow* between two stationary corrugated walls [40, 41, 42, 43, 44]. This is a slight generalization of the unidirectional problem of pressure driven 2D Poiseuille laminar flow between two flat parallel plane boundaries. This case has received considerable attention in the literature because of the potential that corrugated walls have for increasing the heat and mass transfer efficiencies in various transport processes. In general, most authors consider the limiting case in which the amplitude of the corrugations are small in comparison to the spacing of the channel walls, i.e. when $T/G \to 0$ and estimate the flow field using asymptotic methods. As expected, at lowest order, the solution approximates that of Poiseuille flow. At higher order, the solution displays quite complicated behavior in which the flow decelerates where the channel expands and accelerates where it contracts. An adverse pressure gradient is evident during deceleration. This may subsequently lead to flow separation and transition.

In the second category II are pressure-driven *turbulent* flows over rough walls (Figure 2.3b). Like category I, we find a substantial amount of literature in this area related to boundary layer control. This literature begins with an understanding of

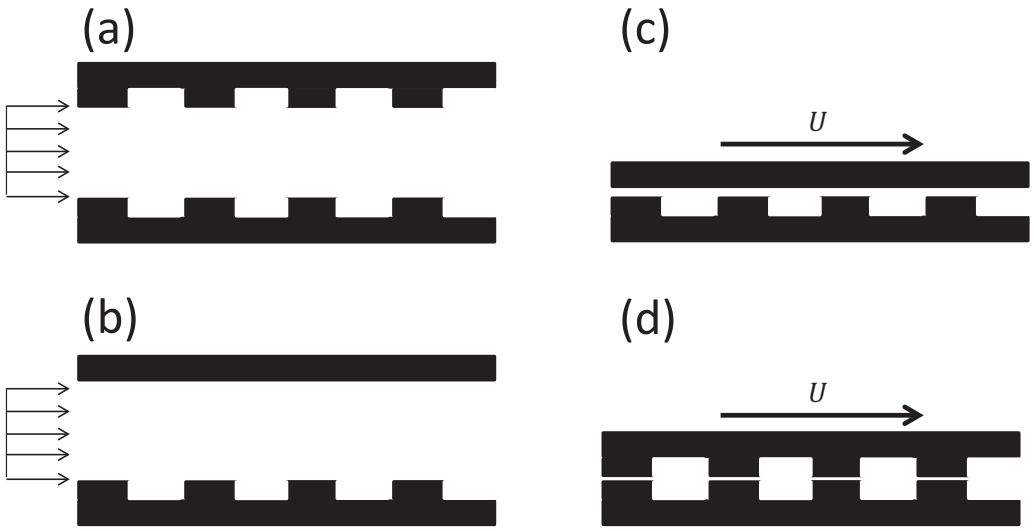

Figure 2.3: Schematic of the different geometries found in the literature which approximate the case considered. (a) Pressure-driven *laminar* flow over corrugated walls. (b) Pressure-driven *turbulent* flow over one corrugated wall. (c) Lid driven cavity flow. This case can be either laminar or turbulent. (d) Lid-driven flow over opposing corrugated walls. This geometry represents the case considered in this work.

the turbulent boundary layer formed over a smooth plate. Nikuradse [45] gives the following correlation for the velocity near the wall

$$u^+ = \frac{1}{\kappa} \ln y^+ + B_o \tag{2.10}$$

where u^+ is the dimensionless velocity defined by $u\sqrt{\rho/\tau_w}$; y^+ is the dimensionless distance normal to the wall defined by $y\sqrt{\tau_w/\rho\nu^2}$; κ is the Von Karman constant; B_o is a empirically-determined constant; and ρ and ν are the density and kinematic

viscosity of the fluid. Zanoun et al. [46] and Jimenez [47] have summarized the literature and shown that κ and B_o vary in the range of $[\kappa, B_o] \in [0.38, 0.45] \times [3.5, 6.1]$. With roughness elements Nikuradse [45] has shown that the velocity field near the wall is given by an equation of the form

$$u^+ = \frac{1}{\kappa} \ln y^+ + B_o - \Delta B_o(k_s^+) \tag{2.11}$$

where k_s^+ is a roughness Reynolds number defined by $k_s \sqrt{\tau_w / \rho \nu^2}$. The roughness function, ΔB_o, depends on type of roughness such as sand, sand mixture, threads, spheres etc. Examples of the form of ΔB_o are given by Mokamati et al. [48].

A number of authors have examined the local flow field *within* the roughness elements either by direct flow visualization or through computation [49, 50, 51, 52, 53, 54]. With flow over square-ribbed roughness elements, [55] phenomenologically characterized two distinct flow fields, *i.e.* $d-$ or $k-$ type. This is illustrated in Figure 2.4. Simpson [56] advances that the the transition from $d-$type to $k-$type occurs when the aspect ratio of the cavity is $T/W \approx 0.25$ and later, this value reported by other researchers [47, 57, 58]. With $d-$type roughness, $T/W > 0.25$, the cavity is occupied primarily by a single vortex, with two minor vortices found in the lower corners. This flow is usually considered to be steady. With $k-$type roughness, i.e. $T/W < 0.25$, the central vortex is absent and there is penetration of the streamlines from the outer flow into the cavity. In contrast to $d-$type, this flow displays some time dependent behavior as Keshmiri et al. [59] indicate the potential for vortex shedding.

In the third category III are driven cavity flows (Figure 2.3c). Driven cavity flows, by definition, are bounded internal flows resulting from the motion of a boundary. Most studies have been performed on rectangular cavities with the upper boundary

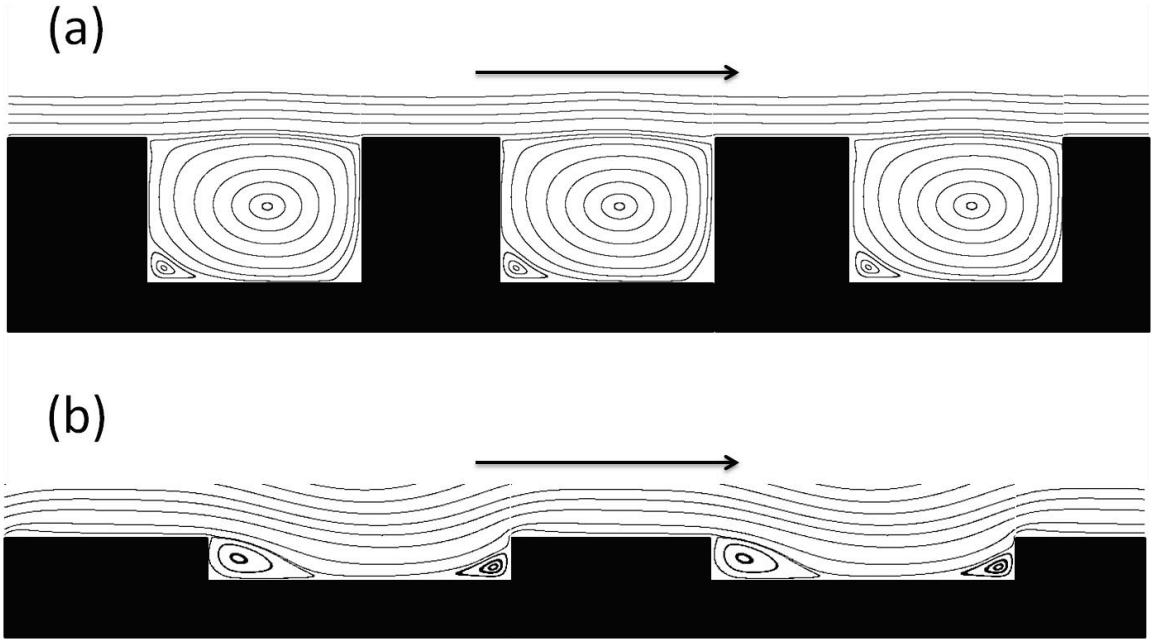

Figure 2.4: Schematic of the phenomenological flow fields found over ribbed roughness elements: (a) d-type flow; (b) k-type flow.

translating at a constant velocity [60, 61, 62]. The case where $G = 0$ represents an important flow that has been a benchmark for fundamental fluid mechanics studies in all aspects of experimental, theoretical and numerical work. The flow contained in this geometry is similar to that described for the d-type classification in category II flows: an internal bounded vortex exists with corner vortices in the lower corners. It has been shown by Pan and Acrivos [62] and Hellou and Coutanceau [63] that for Stokes flow as the ratio T/W increases above unity a transition occurs where the corner vortices grow progressively larger and coalesce into a second primary vortex. Further increasing T/W, this process continues and it has been proven mathematically by Moffat [64] that an infinitely deep cavity would have an infinite number of equally spaced vortices. Exploring higher Reynolds numbers lid-driven cavity flow has been observed to become quasi-periodic above Reynolds number of 7400 and chaotic above Reynolds number of approximately 11000 [65, 66]. A comprehensive review of fluid

mechanics in the driven cavity is provided by Shankar and Deshpande [67].

The case where $G > 0$ is of interest, because it represents a geometry similar to that found in a LC refiner. Wittberg et al. [68] and Khohkar [69] simulated a three-dimensional cavity with an imposed pressure gradient along the cavity axis. The formation of multiple primary vortices under T/W ratio of 1.5 was observed, as in the case of $G = 0$ above. Note that these works lack any description of time-dependency in cases where Reynolds exceeds the onset of periodic/chaotic behavior.

In recent years, the flow field in periodically temporal lid-driven cavity has been extensively examined for both laminar and turbulent flows [70, 71, 72] where the flow in the cavity is driven by a flat lid with oscillatory motion, e.g. sinusoidal motion. Although this oscillatory motion causes the periodic time-dependent behaviours in the flow field, it can not describe the time-dependent flow field in the refiner cross section. In the refiner, motion of a spatially periodic boundary leads to the temporal variation in the flow.

There are only a limited number of studies in category IV (see Figure 2.3d) and these have been found within the Pulp & Paper literature. These studies have focussed on high-speed photography and describe the flow field qualitatively [68, 73, 74, 75]. For very dilute suspensions, Fox et al. [76, 77] reported that the suspension flows inward in the stationary and outward in the moving cavities (see Figure 2.5). Minor recirculation currents, called secondary and tertiary flows, have also been observed. Note that all descriptions of the refiner flow field mentioned above lack any description of time dependency. Clearly this flow geometry resembles driven cavity flow where the shear imposed on the top of each cavity acts impulsively, i.e. it is not a uniform driving force. Nissan [74] is one of a few researchers who has mentioned that chaotic behavior inside the refiner arises in a time-dependent driven cavity flow.

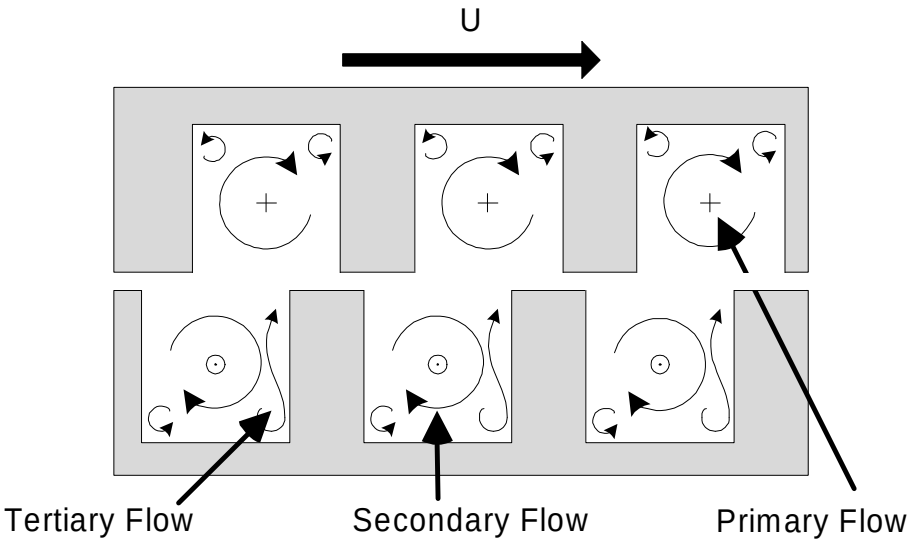

Figure 2.5: Schematic of the flow in the cavities of a refiner plate. "+" and "⊙" represent opposing flow fields in z-direction.

In the most recent work, Kondora and Asendrych [78] numerically simulated and investigated the effect of pulp consistency for the three-dimensional unsteady flow in LC refiner. Their results demonstrated the general flow pattern reported by Fox [76, 77] and most importantly, identified the inward flow in the stator grooves.

2.4 Effect of groove depth in refining

Based on the literature [79, 30, 22], Groove depth is expected to be high enough to let the proper amount of pulp suspension pumped in the refiner and low enough to refine the large amount of fibres. Excessive groove depth results in more fibres passing through the refiner untreated; while decreased groove depth brings the fibers to the bar edges and promoting refining action, but restricting flow rate and reducing hydraulic capacity.

On the other hand, it was found that hydrodynamic losses in refiner increases

with the deeper bars [29, 30]. In 1976, Siewert and Selder [80] reported a linear relationship between groove depth and no-load power. Antku and Ludwig [79] found that reducing a groove depth from 6 mm to 3 mm alters no-load power about 40%.

2.5 Summary of literature

Although pervious researchers have made huge number of advances, as listed above, there are some limitations and unanswered questions that we are willing to focus on them in this thesis:

- The present descriptions of refiners by scaling laws are by no means a comprehensive measure of the no-load power consumed during operating. They reflect the fact that energy is consumed and is related to factors such as diameter and rotational speed, but other factors known to be important are not considered in these descriptions.

- The flow patterns within the refiner are complex and have yet to be understood. In general, flow is observed to occur radially outward in the grooves of the rotor and inward in the grooves of the stator. Secondary and tertiary flows have been reported. Neither the effect of gap size nor groove dimension have been considered in this analysis.

2.6 Objectives of the thesis

The overall goal of this study is to minimize the no-load power consumption during the pulping process in low consistency refining. As a result, the specific objectives of this study include the following:

- To develop a correlation to estimate the no-load power by determining the effect of pulp suspension rheology, plate design and refiner operating conditions individually.

- To extend our understanding of time-dependent flow field in LC refining, specifically, for various gap sizes and groove aspect ratios.

2.7 Approaches of the thesis

Given these objectives, our research approaches are focused on targeting each one of these objectives separately:

- *Chapter 3*: A series of experimental studies is conducted to measure the no-load power for a number of laboratory and industrial LC refiners. We measure the power consumed as a function of gap size, flow rate, and rotational speed for both water and mechanical pulp with different consistencies. A dimensional analysis is performed on this data set to develop a scaling law.

- *Chapter 4*: A deeper understanding of the no-load power is studied computationally in this chapter. Simulation of this problem is particulary difficult as it involves the time-dependent, three-dimensional flow of a multiphase suspension in a swirling turbulent flow. Due to this complexity, the geometry is reduced to a simpler geometry, i.e. two-dimensional flow field in the cross section of a LC refiner. A large number of unsteady simulations are conducted over the range of velocities and gap sizes considering water as the fluid inside the refiner.

- *Chapter 5*: The two-dimensional numerical study is extended to investigate the effect of groove aspect ratio for a wide range of velocities. All results in this study are obtained from the steady-state simulations.

Chapter 3

Experimental Measurement of the No-load Power in LC Refining

In this chapter, we experimentally measure the effect of most of the affecting parameters on no-load power in LC refiners and ultimately, we aim to develop a correlation for no-load power. Despite the literature contains a large number of experimental and theoretical studies of the no-load power in LC refining and also different correlations have been proposed, but there is no comprehensive experimental investigation of the effect of all significant parameters and the suggested formulas just cover a few of these parameters.

The chapter proceeds as follows. Below in §3.1 we introduce the experimental setup for the laboratory refiners. Then, in §3.2 we qualitatively introduces the main results for the effect of gap size, rotational speed, flow rate, rotational speed, pulp suspension consistency and bar and groove widths on the pilot scale refiners. In §3.3, we propose a new correlation for our laboratory refiners based upon our findings of the previous section and then, by collecting data of inner and outer diameters and groove depth for various mill refiners, we will be able to extend our correlation to industrial scales. Finally, the chapter ends with conclusion in §3.4.

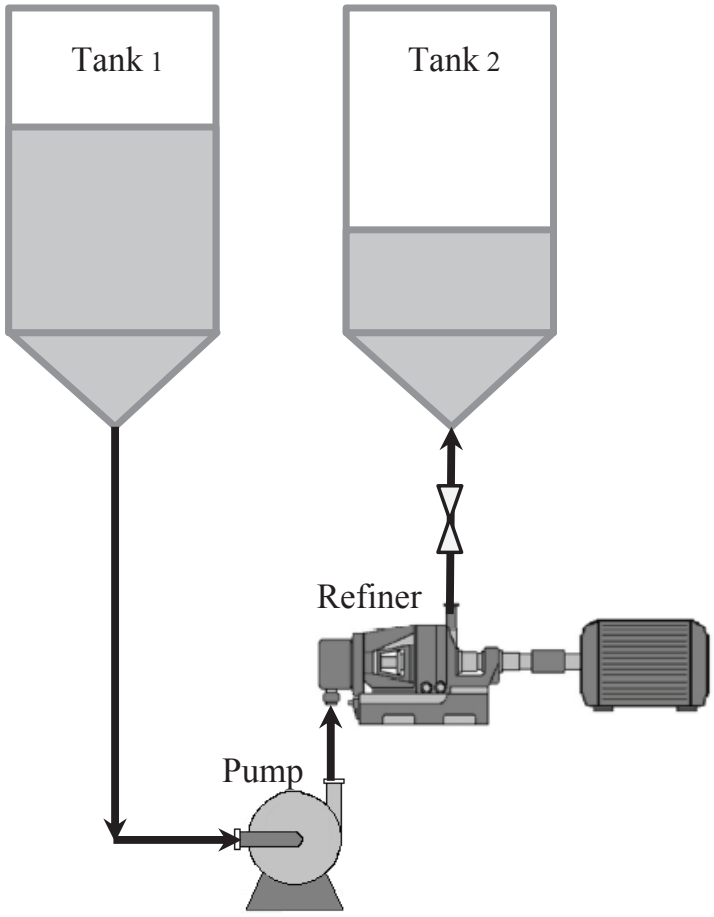

Figure 3.1: Illustration of the LC refiner loop used for all trials

3.1 Experimental setup

In this work, we used a series of refiner plates with constant inner and outer diameters (D_i, D_o) and constant groove depth (T) to experimentally understand the effect of some parameters on no-load power. Experiments were performed in two flow loops with two different refiners varying in size; a $12''(0.305\,m)$ Sprout-Waldron single disc as well as a $16''(0.406\,m)$ Aikawa single disc refiner. Both flow loops consist of two large tanks, a centrifugal pump, and a single disc LC refiner (Figure 3.1). Fluid is pumped from the first tank to the refiner; then passes through the center of sta-

	D_o (in)	D_i (in)	B (mm)	W (mm)	T (mm)	Angle $[^\circ]$	BEL (km/rev)
Plate 1	16	8.75	1.0	2.4	4.8	15	5.59
Plate 2	16	8.75	1.6	3.2	4.8	15	2.74
Plate 3	16	8.75	3.2	4.8	4.8	15	0.99
Plate 4	16	8.75	2.0	3.6	4.8	15	2.01
Plate 5	16	8.75	1.0	1.6	4.8	15	10.1
Plate 6	16	8.75	1.0	1.3	4.8	15	12.9
Plate 7	12	6.5	3.2	4.8	3.2	15	0.417
Plate 8	12	6.5	1.6	3.2	3.2	15	1.159
Plate 9	12	6.5	1.0	2.8	3.2	15	1.85

Table 3.1: Specifications of all nine lab refiner plates

tor, is forced outward from refiner and then returns back to the second tank. The outer diameter of refiner disc in one loop is $12''(0.305\,m)$ and in the other loop is $16''(0.406\,m)$. The experiments were carried out in six pairs of rotor and stator discs with different bar and groove widths and constant groove depth of $4.8\,mm$ for the $16''$ diameter refiner and three different pairs of rotor and stator discs with different bar and groove widths and identical groove depth of $3.2\,mm$ for $12''$ diameter refiner. Table 3.1 includes the geometrical characteristics of each pair of the discs.

Each refiner loop is instrumented such that for a given gap size, rotational speed, flow rate, and the total power can be recorded using LABVIEW software. A large number of trials were conducted to measure no-load power as a function of these variables for both water and low consistency pulp suspension as the circulating fluids. The pulp used was a Chemi-Thermo-Mechanical-Pulp (CTMP) which is being produced by a combination of the mechanical and chemical processes [81, 82].

For experiments conducted with plates $7-9$, the rotational speed was varied from 400 to $1200\,rpm$ while the gap size was changed from 0.2 to $5\,mm$. Measurements were obtained with both water and pulp for $300, 600$ and $900\,lpm$ flow rates for all

$12''$ plates	$16''$ plates-Water	$16''$ plates-Pulp
$9.4 \times 10^5 < Re < 2.8 \times 10^6$	$1.6 \times 10^6 < Re < 6.3 \times 10^6$	$1.6 \times 10^6 < Re < 6.3 \times 10^6$
$0.0013 < G^* < 0.035$	$0.005 < G^* < 0.045$	$0.0001 < G^* < 0.045$
$0.011 < C_q < 0.1$	$0.007 < C_q < 0.075$	$0.007 < C_q < 0.075$

Table 3.2: Range of operating variables for the experimental setup

$12''$ plates. Likewise, for the plates $1-6$, the rotational speed was varied from 400 to $1500\,rpm$ while the gap size changes from $0.5\,mm$ to maximum possible size of $9\,mm$ for water and from very small gap, i.e. $0.02\,mm$ to $9\,mm$ for pulp experiments. The range of flow rate changes from 600 to $1500\,lpm$ for all $16''$ plates. A summary of the range of the non-dimensional variables for two series of plates is shown in Table 3.2.

Some experiments were repeated $3-4$ times which yields error for all these cases of less than 6%. One source of error in these measurements was the variation of temperature for each case since the water/suspension re-circulated a closed loop numerous times. It was difficult to keep a constant fluid temperature for each trial. Temperature in the $12''$ refiner loop had been varying between $25°C$ to $40°C$ for water and $55°C$ to $65°C$ for pulp suspension. Likewise, fluid temperature in the $16''$ refiner loop had been changing between $30°C$ to $45°C$ for water and $55°C$ to $65°C$ for pulp suspension.

Figure 3.2 compares both the mechanical loss and the total no-load power for the $16''$ disc refiner. Total no-load power has measured for water at $Q = 1000\,lpm$ and $G = 9\,mm$. Shaft and bearing losses (i.e. mechanical power) are measured by rotating refiner disc in the absence of water at various rotational speeds. This power is mainly the function of rotor speed and increases slowly as the motor speed grows up. Furthermore, as shown in this figure, plate design and gap size between rotor and stator have no effect on the measured mechanical losses. In comparison with the total no-load power, the ratio of the mechanical loss to the total no-load power

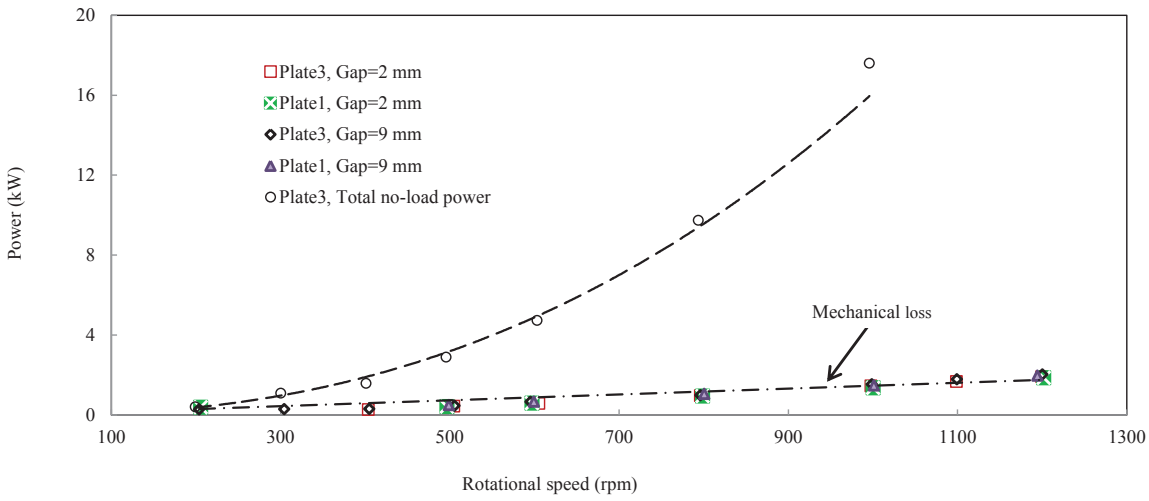

Figure 3.2: Comparison of mechanical loss respect to the total no-load power for two 16″ plates ($Q = 1000\,lpm$ and $G = 9\,mm$)

decreases as the motor speed goes up.

Since the aim of the study is to gain knowledge about the hydraulic/pumping losses, the mechanical power consumption has been deducted from all reported powers from here on. The experimental results obtained for the 16″ plates were collected in two steps; for the first step, the hydraulic power ($Power_n{}^*$) due to the rotation of the rotor in fluid was measured and then at the next step, the total no-load power ($Power_n$) which covers both hydraulic and pumping powers, was measured. To measure the hydraulic power, the valve was closed, no flow was allowed to pump through the refiner and water was confined between rotor and stator. It should be warned that closing the valve while under power may result in steam generation and dangerous pressurization of the refiner casing. The power data was collected by varying gap size and rotational speed. The total no-load power was measured when there was flow through the refiner. By collecting data for six 16″ plates, the obtained data is used to provide a statistical model for prediction of no-load power based on all operational variables, say rotational speed (ω), flow rate (Q) and gap size (G) and

also geometrical parameters, bar width (B), and groove width (W). To do this, the model will be presented in terms of these non-dimensional variables:

$$P_n = \frac{Power_n}{\rho\omega^3 {R_o}^5}, C_q = \frac{Q}{\omega {R_o}^3}, Re = \frac{\omega {R_o}^2}{\nu}, G^* = \frac{G}{R_o} \tag{3.1}$$

This form of formula can be applied to plates with constant R_i, R_o and T. Finally, collected data for both $16''$ and $12''$ lab refiners and also a series of mill data reported in the literature [27] has been used to generalize the correlation to a wide range of refiner sizes.

3.2 Results

The pulp used in all experiments is a Chemi-Thermo-Mechanical-Pulp (CTMP) consisting of spruce, pine and fir (SPF) tree species. Initial length-weighted average fibre length of these fibres is about $1.9\,mm$. To study the effect of consistency of pulp on no-load power, one plate with $16''$ diameter (Plate 2) and another plate with $12''$ diameter (Plate 7) have been chosen and experiments were run for both pulp and water. For Plate 2, pulps with consistencies of 1.5% and 3.5% have been used and for Plate 7, the consistency of pulp was chosen to be around 3%. The density of low consistency pulp suspension is approximated as the density of water.

By comparison of power for both water and mechanical pulp for the $16''$ plate, it was initially observed that at wide gaps there is almost no significant difference between the measured power for water and for pulp suspensions with 1.5% and 3.5% consistencies. Figure 3.3a and Figure 3.3b show the hydraulic and total no-load powers, respectively, as a function of rotational speed for these three different fluids at wide gaps. The total no-load power was collected for constant flow rate of $600\,lpm$.

A strong correlation for rotational speed can be seen; while under similar conditions, almost the same hydraulic and total no-load powers were measured for both pulp and water. As mentioned in §2.1, the difference of less than 10% in the no-load power of water and mechanical pulp has been reported previously [4, 9, 11, 27]. The identical behaviours of these two fluids in the no-load region may also be explained by the range of temperatures that each of them have been measured at. As mentioned earlier, experiments of 16″ refiner loop with pulp suspension have been performed in the higher temperature of $55°C$ to $65°C$; while the temperature of experiments with water was ranged between $30°C$ to $45°C$.

Figure 3.4a and Figure 3.4b shows the comparison of water with 3% pulp for the 12″ plate and two different rotational speeds. Based on these figures, the behaviours of both pulp and water are almost the same at wide gaps and by closing the gap between rotor and stator, from a specific gap (G_l) around $2\,mm$, their trends start separating.

Likewise, Figure 3.5 reveals trends of power as a function of gap size of Plate 2 with 16″ diameter for water, 1.5% and 3.5% pulps. Gap varies from closed distance to the wide gap of $9\,mm$. By decreasing the gap from $9\,mm$ down to the gap around $2\,mm$, the behaviors of all fluids are similar to each other and there is only about $6-7\%$ variation which is in the range of experimental errors. For the gaps smaller than $2\,mm$, a sudden separation happens in trends of pulp and water.

Lets introduce the starting point of separation as point of refiner loading, G_l. To investigate the reason behind the sudden change in the slope of pulp curve, pulp properties were examined for $G < G_l$. Figure 3.6 to Figure 3.8 display freeness, fibre length and tensile variations of fibres by gap size, respectively. Results represent data for the 16″ refiner at a constant flow rate of $Q = 500\,lpm$ and three different rotational

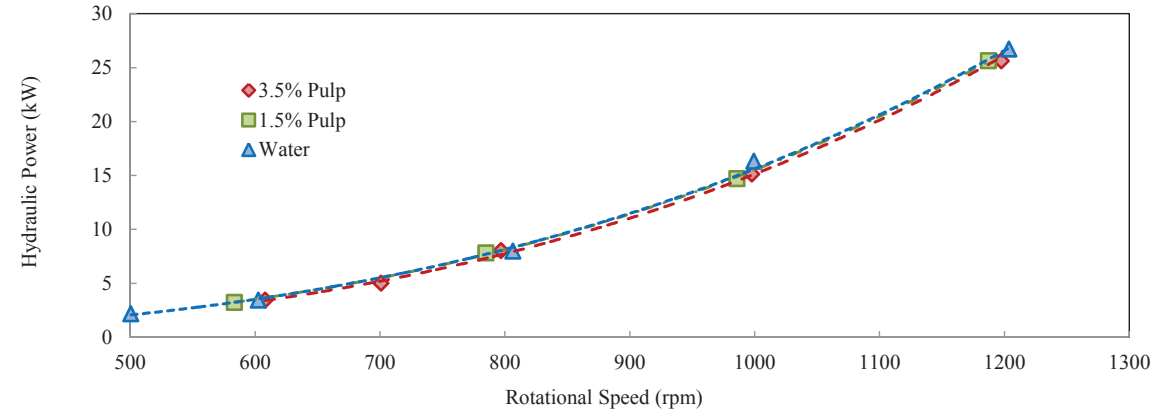

(a)

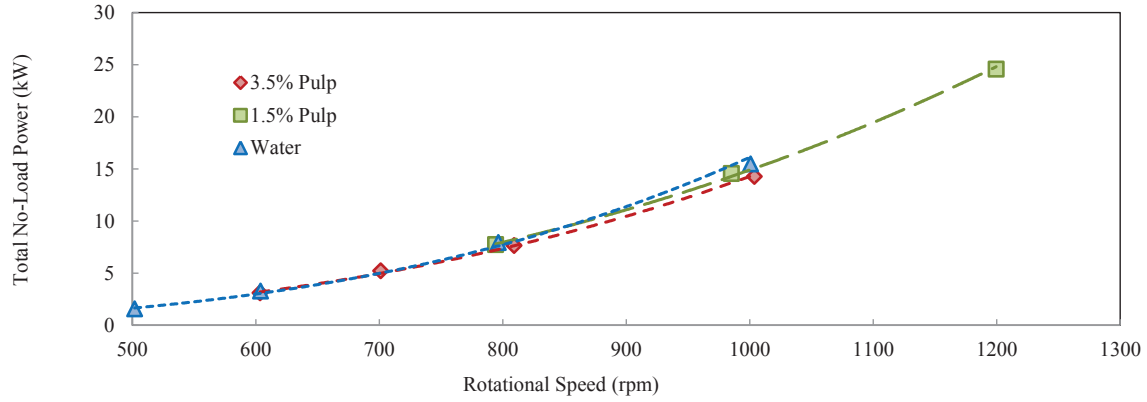

(b)

Figure 3.3: Comparison between power of water and pulp with two different consistencies for Plate 2: (a) Hydraulic power, (b) Total no-load power when $Q = 600\,lpm$.

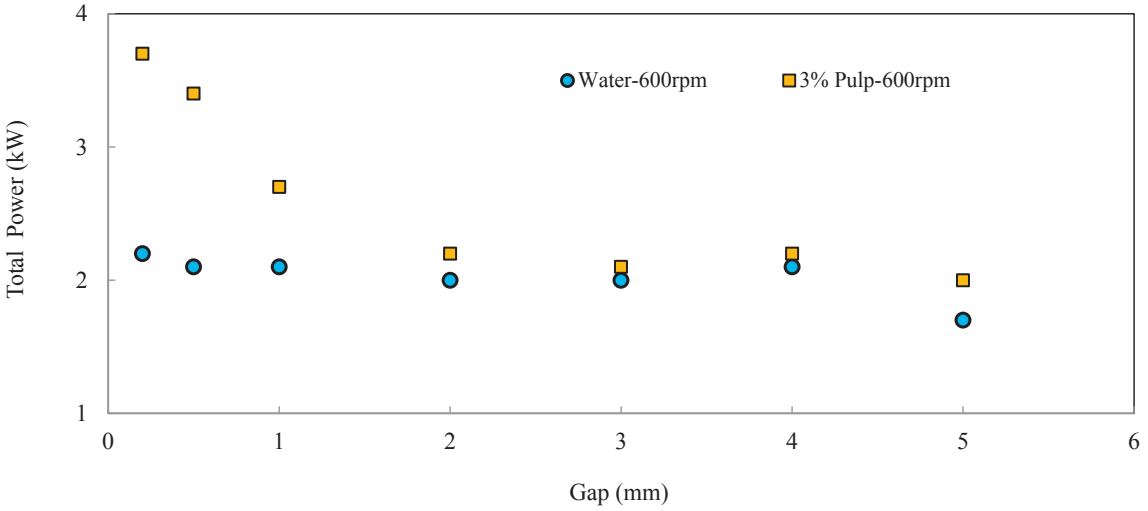

(a)

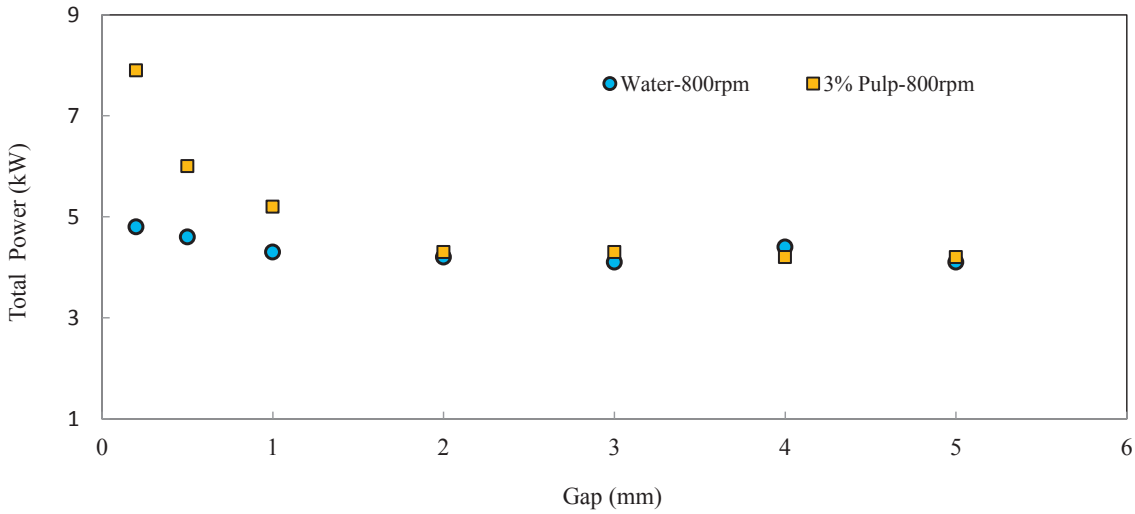

(b)

Figure 3.4: Total power vs. gap for Plate 7: (a) $Q = 600\,lpm, \omega = 600\,rpm$, (b) $Q = 600\,lpm, \omega = 800\,rpm$

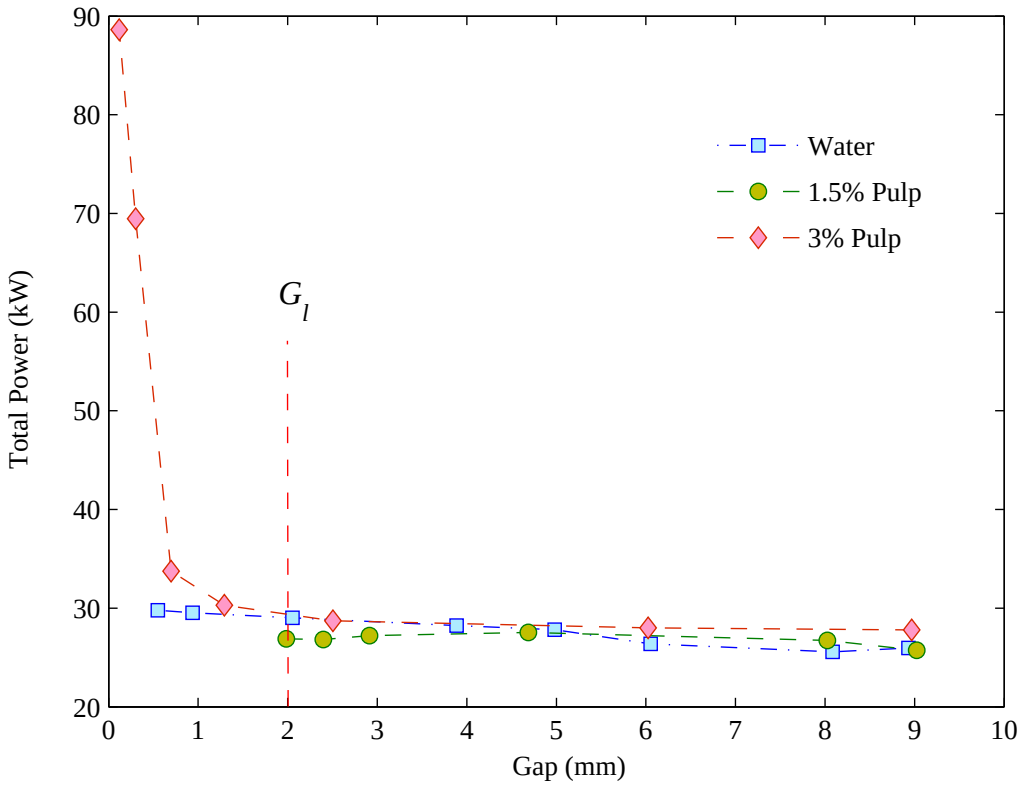

Figure 3.5: Total power vs. gap for Plate 2: $Q = 500\,lpm$ and $\omega = 1200\,rpm$

speeds. Figure 3.6 shows the effect of gap size on freeness (standard measure for the ability for water to drain through the pulp). By decreasing the gap between rotor and stator, freeness starts dropping for $G < 2\,mm$. As it is shown in Figure 3.7, the length of fibres starts shortening for $G < 2\,mm$ as well. Figure 3.8 shows that the increase in tensile strength of the paper has a similar behavior as the other properties with decreasing gap.

From all three figures above, it appears that at higher rotational speeds the refiner starts to change properties of fibre at larger gaps, but the point of refiner loading (G_l) does not go further than $2\,mm$ for all three rotational speeds. It may be concluded that the value of $G_l \approx 2\,mm$ relates to the initial length-weighted average fibre length

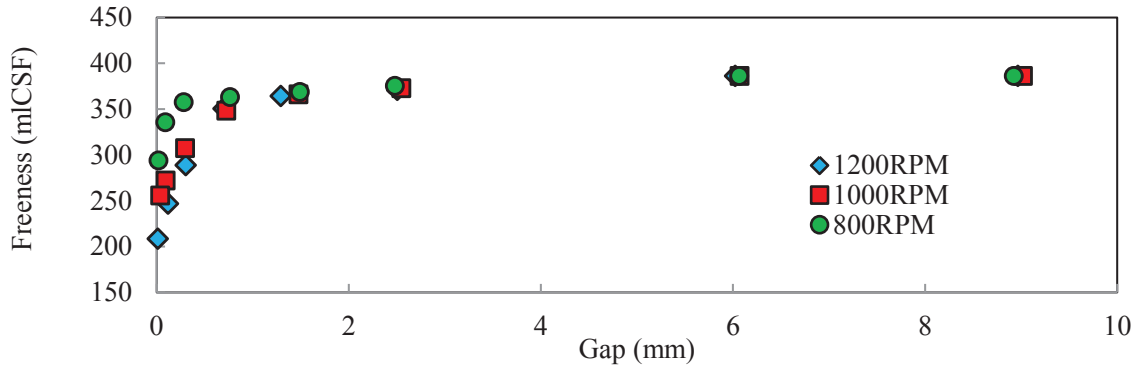

Figure 3.6: Freeness of fibers at various gap sizes between rotor and stator for Plate 2 and $Q = 500\,lpm$

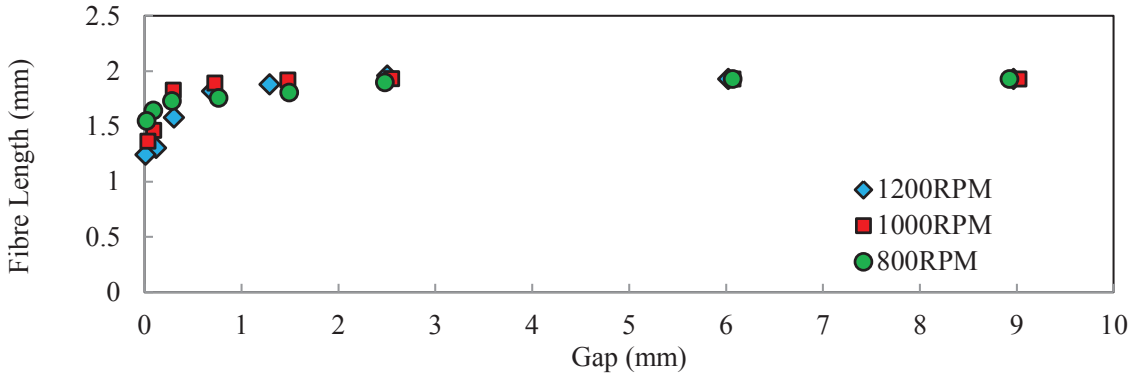

Figure 3.7: Length-weighted (L_W) average length of fibers at various gap sizes between rotor and stator for Plate 2 and $Q = 500\,lpm$

of these fibres which is about $1.9\,mm$. Beyond this point, the behavior of both water and pulp are identical for $G_l < G$. Figure 3.9a and Figure 3.9b include the graphs of power respect to the gap for two $16''$ plates. Each figure shows power for two different rotational speeds and different flow rates. The trends in each figure are categorized to two groups; one for $600\,rpm$ and the other for $800\,rpm$. The trends at each group represent hydraulic power and also total no-load power obtained for different flow rates of $600\,lpm, 800\,lpm$ and $1000\,lpm$.

Since the total no-load power shown for different flow rates consists of both hy-

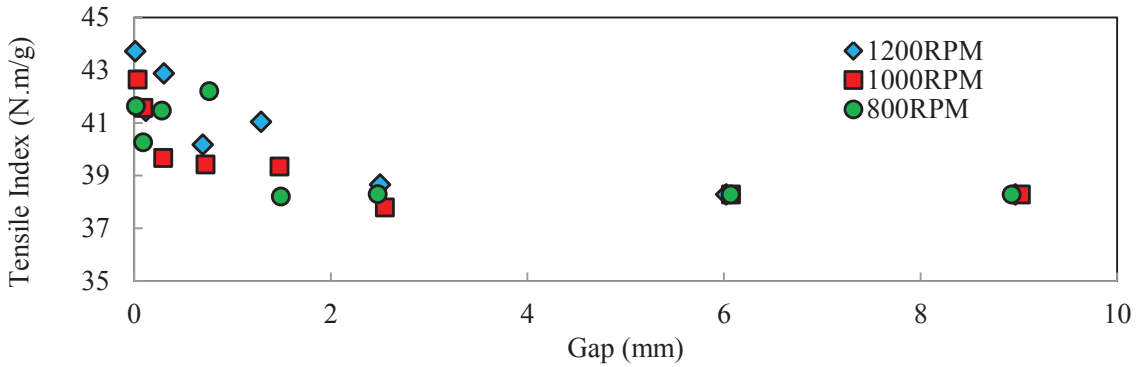

Figure 3.8: Tensile of fibers at various gap sizes between rotor and stator for Plate 2 and $Q = 500\,lpm$

draulic and pumping powers, it can be seen that for a constant flow rate of $800\,lpm$ at wide gaps, say $9\,mm$, about 10% of total no-load power consumption goes to the pumping power; while for the same flow rate and smaller gaps, say $2\,mm$, the pumping power covers about 25% of the total no-load power and this value is higher for smaller gap sizes. From these figures, we see that hydraulic power is dependent on rotational speed. Pumping power, which is the difference between the total no-load power and hydraulic power, depends on gap size, rotational speed and flow rate. Hydraulic power can be interpreted as the total no-load power when $Q = 0\,lpm$ and is independent of gap size; while by increasing the flow rate, the amount of total no-load power increases slowly. Further, the data suggests that the total no-load power decreases by increasing the gap.

The hydraulic power and gap for all trials is plotted in Figure 3.10 as non-dimensional hydraulic power ($P_n{}^* = \frac{Power_n{}^*}{\rho\omega^3 R_o{}^5}$) and non-dimensional gap size. It should be noted that error bar on each data point shows the standard deviation of hydraulic power numbers collected for a wide range of rotational speeds at a specific gap. As indicated in this figure, $P_n{}^*$ does not vary by changing the gap size for all six plates and trends show straight lines for all gap sizes from small gaps to wide gaps. $P_n{}^*$s

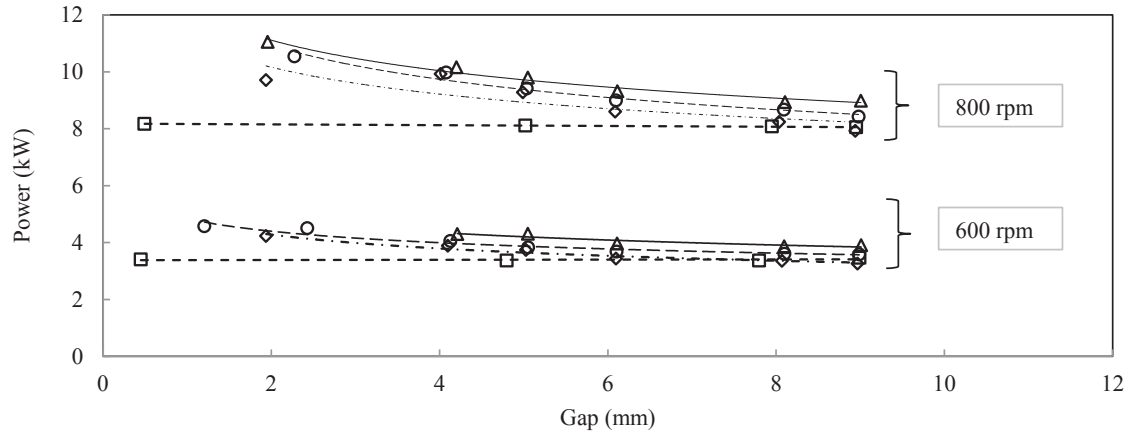

(a)

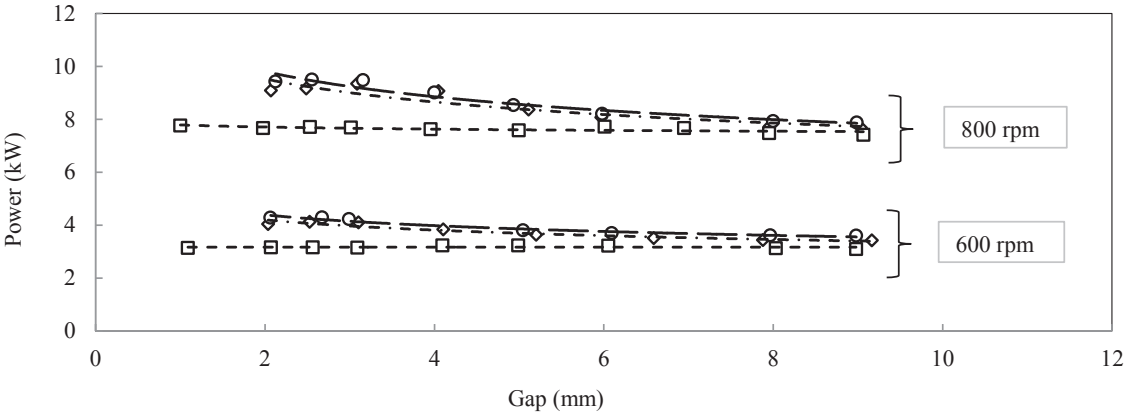

(b)

Figure 3.9: Graphs of total no-load power collected for water vs. gap for two different rotational speeds and various flow rates for two 16″ plates (a) Plate 2 and (b) Plate 5. At no flow case (hydraulic power), the no-load power is independent of gap. ($\square : Q = 0\,lpm; \diamondsuit : Q = 600\,lpm; \circ : Q = 800\,lpm; \triangle : Q = 1000\,lpm$)

for all plates are close to each other and the difference between the upper $P_n{}^*$ which allocated to Plate 1 and the lower one for Plate 6 is about 10% and can be explained by the difference in bar and groove widths. Later, it will be explained how $P_n{}^*$ can be related to the geometry of plates.

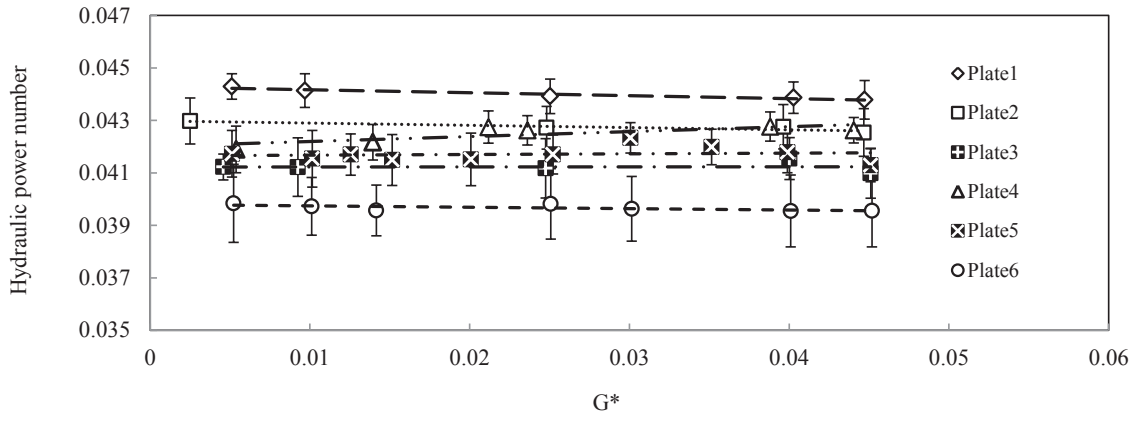

Figure 3.10: Correlation between hydraulic power number and dimensionless gap for all 16″ plates

Figure 3.9 shows that the total no-load power decreases with increasing gap. In the other word, since experimental data indicates that hydraulic power is independent of gap size, the only term that can vary by gap is pumping power. Following Nece and Daily [37], we propose that $Power_P \propto G^{-\frac{1}{8}}$ which stands in good agreement with our observations. Figure 3.11 shows the relation between hydraulic power and rotational speed for all plates at wide gaps, e.g. 8 or 9 mm. It indicates that hydraulic power depends on ω^3, which means that $P_n{}^*$ is independent of Reynolds Number, Re.

The collected data show a slight dependency of total no-load power number on Reynolds number which means that pumping power number is dependent on Reynolds number. Results indicate that pumping power is proportional to $\omega^{2.2}$ or pumping power number is proportional to $Re^{0.2}$. This finding is in good agreement with what Daily et al. found [38].

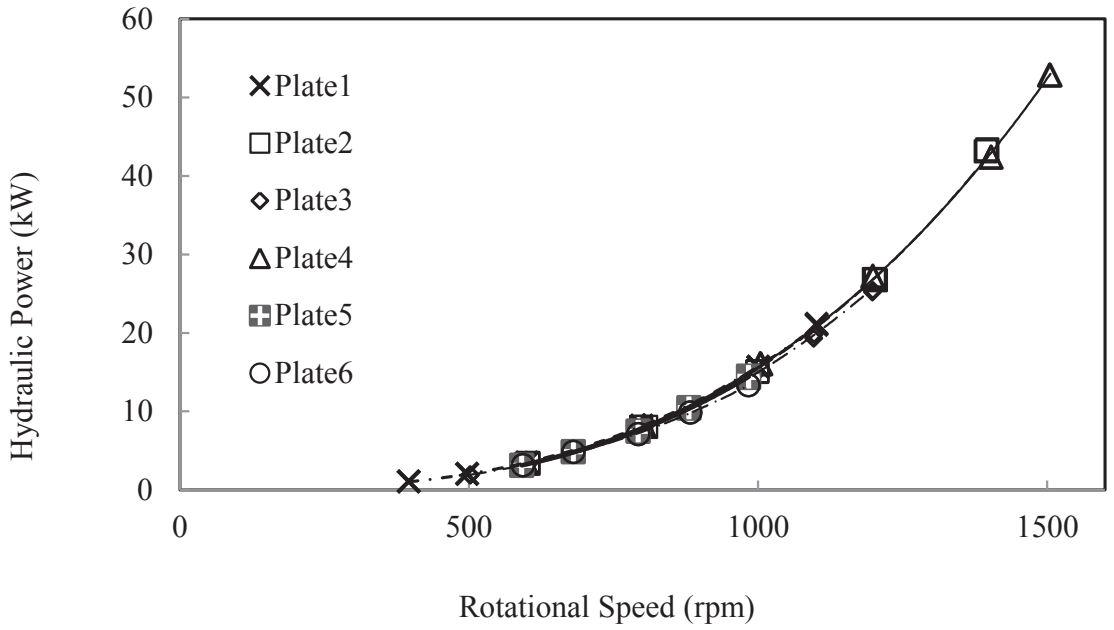

Figure 3.11: Cubic dependency of hydraulic power on rotational speed shown for all $16''$ plates at $G = 9\,mm$

Figure 3.12 shows how no-load power increases by flow rate. This figure represents power as a function of flow rate for Plate 4 for three rotational speeds at wide gap of $9\,mm$. Power at $Q = 0\,lpm$ represents hydraulic power where there is no evidence of pumping effect. Graphs show a slight and linear relation between total no-load power and flow rate. Based on the obtained data, 20% increase in the flow rate makes a 5% change in no-load power.

As mentioned earlier, there is a difference in the measured ${P_n}^*$ of all six plates that is a function of bar and groove width variations. First, we examine the three plates with bar width of $B = 1\,mm$. As it is shown in Table 3.3, Plate 1 with the widest groove width consumes more hydraulic power. Therefore, for the plates with the identical bar width, the wider the groove width is, the higher energy consumes.

A study to relate the values of ${P_n}^*$ to plates geometry is indicated that the difference between the hydraulic powers of the plates cannot be explained by BEL of

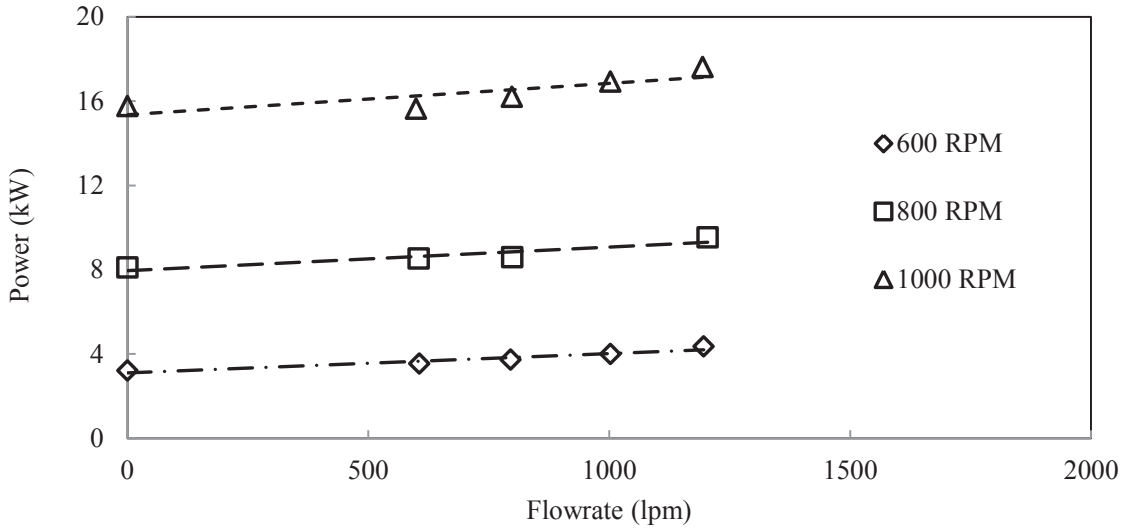

Figure 3.12: Increase in total no-load power as a function of flow rate for Plate 4 at $G = 9\,mm$

	$W(mm)$	$P_n{}^*$
Plate 1	2.4	0.0439
Plate 5	1.6	0.0417
Plate 6	1.3	0.0396

Table 3.3: Comparison of $P_n{}^*$ for three plates with $B = 1\,mm$ and different groove widths

plates but by a new parameter:

$$\varepsilon = \frac{W}{W + B} \tag{3.2}$$

where ε is called "Roughness density". Figure 3.13 shows how $P_n{}^*$ relates to ε.

Roux et al. [83] define $n = \frac{2\pi R_o}{W+B}$ as the total number of bars and grooves that can potentially exist on refiner disc in radial direction without any angle. Based on this definition, ε generally represents ratio of area of grooves to the total area of refiner disc. In other words, for the refiner plates with a constant groove depth, ε is the ratio of the total grooves area to the total area of both grooves and bars. Increasing

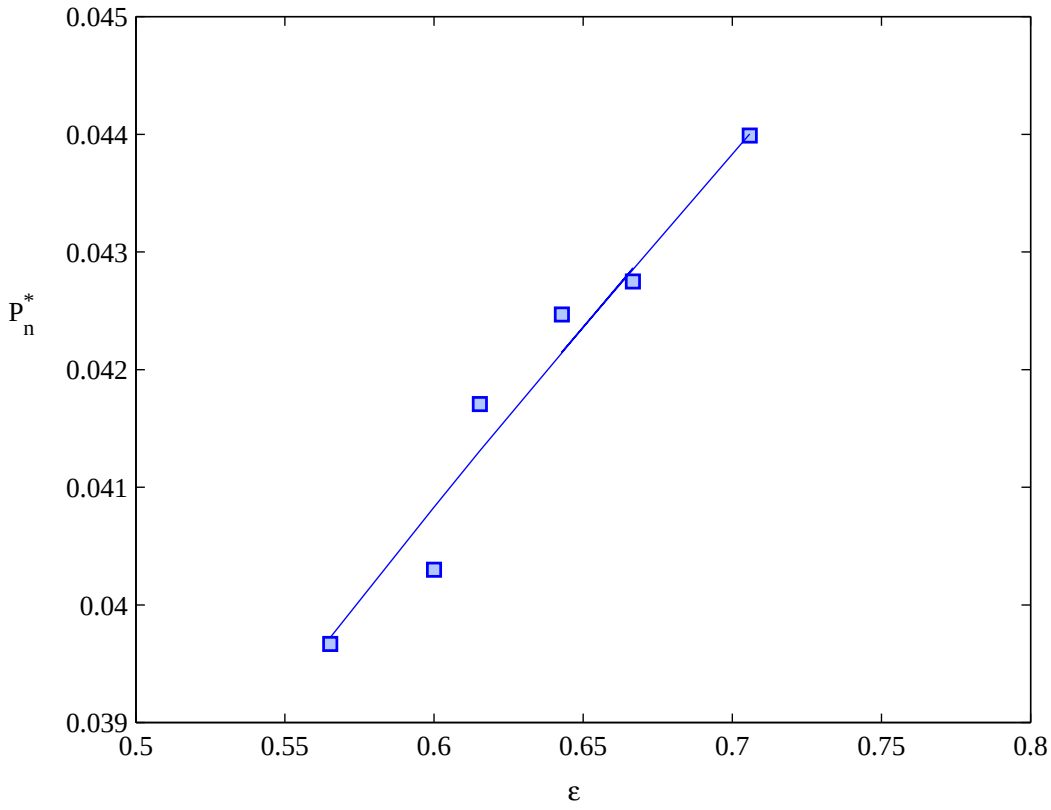

Figure 3.13: Correlation between hydraulic power number and ε for all 16″ lab plates

ε leads to smaller surface between bars and greater groove volume and consequently to the more energy dissipation.

In a most recent work, Elahimehr et al. [84] are shown that:

$$A^* = 1.14 \left(\frac{B}{W+B}\right)^2 \left(\frac{\theta}{2\pi}\right)^{0.4} \left(\frac{1}{\sin\phi}\right)^{0.5} \tag{3.3}$$

where A^* presents the normalized bar crossing area and θ and ϕ are sector and bar angles, respectively. Combining this relation with our new roughness density parameter, ε, gives:

$$A^* = M(1-\varepsilon)^2 \tag{3.4}$$

where M is a constant value and covers both sector and bar angles which are constant for all 16″ plates.

3.3 Discussion

In the previous sections, the effect of consistency (C), operating parameters (ω, G, Q) and some geometrical parameters (W, B) on no-load power was qualitatively and individually studied. By combining the formats of the previous formulas proposed to predict the no-load power (see Equations 2.3 and 2.4) and the equation proposed by Daily et al. [38] (see Equation 2.9), we propose a new correlation to quantitatively relate all six parameters to no-load power:

$$Power_n = A_0\omega^3\left(\frac{W}{W+B}\right)^{\alpha} + K_0\omega^{2.2}QG^{-\frac{1}{8}} \tag{3.5}$$

Applying non-dimensional parameters changes the formula to:

$$P_n = A\varepsilon^{\alpha} + KC_qRe^{0.2}G^{*-\frac{1}{8}} \tag{3.6}$$

where A and K are constant values and depend on inner and outer diameters, and also bars and grooves geometry. This form of formula is applicable to all plates with constant R_i, R_o and T.

The first term represents the hydraulic power number where there is no effect of pumping power. Hydraulic power is the major part of no-load power consumption. ${P_n}^*$ is independent of Re and G^*. Since the only differences between the plates are bar and groove widths, what makes variation in hydraulic power is roughness density, ε. From Least-Square curve fitting method, α was calculated as $\alpha = 0.478 \pm 0.005$.

The second term is the pumping power and shows the required power to pump

fluid from inlet to outlet. Based on the findings, it varies linearly by flow rate. On the other hand, experiments are shown that pumping power number is not independent of Re and as it is indicated in Figure 3.9, this power is dependent on gap size. The form of non-dimensional parameters in this correlation is in good agreement with what suggested by Daily et al. [38].

Figure 3.14 shows the measured power numbers versus the predicted power numbers calculated by the proposed correlation of Equation 3.6 for all trials of 16″ plates and as it can be seen, the predicted values are in good agreement with the experimental data. The values of all coefficients corresponding to the correlation for the 16″ plates are summarized in Table 3.4.

Plate	A	α	K	R^2
All 16″ plates	0.0515 ± 0.0002	0.478 ± 0.005	0.0115 ± 0.001	0.91

Table 3.4: Coefficients of the proposed correlation for all plates with 16″ diameters

Based on the literatures, a few studies has been done on the effect of groove depth on no-load power. The common conclusion of all these literatures is that no-load power is dependent on the groove depth and decreasing the groove depth restricting flow rate and reducing hydraulic and pumping capacity [29, 30] and therefore reduces no-load power consumption. In the more general case of rotor-stator confined by a stationary housing, some empirical equations have been proposed for the power consumption as a function of roughness for the turbulent flow between rotor and stator [37, 85]. Based on these studies, power increases by increasing the roughness for the fully rough surfaces and this dependency can be described either by logarithmic or power laws.

On the other hand, analyses of losses due to the rotation of a smooth disc in a fluid indicate that disc friction is a function of diameter to the 5^{th} power [86, 87]. For

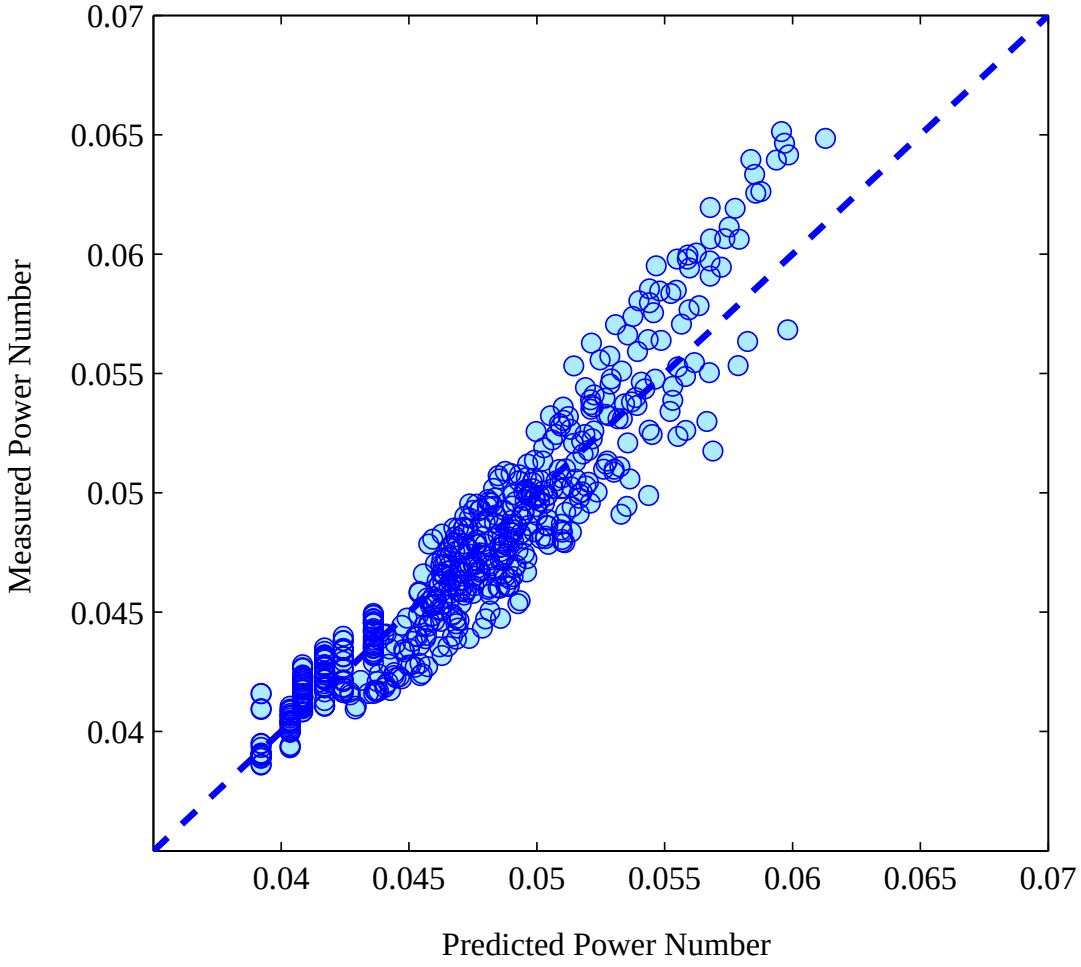

Figure 3.14: Correlation between predicted and measured no-load powers for all plates with 16″ diameters

the discs with roughness, it is shown that the power does not consume exactly with the diameter to the 5^{th} power and this value is a little smaller than 5 [85, 37].

Table 3.5 is summarized all data for different sizes of disc refiners collected from lab and mill refiner machines. Mill data are collected from mechanical pulp and paper mills. The refiner operational variables were controlled and recorded by the mills Distributed Control system (DCS).

Figure 3.15 indicates $\frac{P^*}{\rho\omega^3}$ respect to outer diameter of various disc refiners col-

Refiners	D_o (in)	BEL (km/rev)	W (mm)	B (mm)	T (mm)	ω (rpm)	${Power_n}^*$ (kW)
Mill 1	58	486.00	3	1.45	5.2	425	473
Mill 2	55	377	2.6	1.15	4	425	307
Mill 3	42	96.72	3.1	2.05	6.1	509	308
Mill 4	58	368	3.77	2.375	6.5	400	350
Mill 5	26	15	3.4	3.4	7.45	900	203
Mill 6	52	410	2.4	1	5	425	420
Mill 7	58	320	2.29	1.52	6.1	425	660
Mill 8	72	414	3.21	1.6	7.35	320	800
Mill 9	24	16	3.2	2	6.4	900	100
Mill 10	34	30	3.175	3.175	6.35	600	159
Plate 1	16	5.59	2.4	1	4.8	1200	30.2
Plate 2	16	2.74	3.2	1.6	4.8	1200	29.3
Plate 3	16	0.99	4.8	3.2	4.8	1200	27.7
Plate 4	16	2.01	3.6	2	4.8	1200	29.2
Plate 5	16	10.1	1.6	1	4.8	1200	28.6
Plate 6	16	12.9	1.3	1	4.8	1200	27.2
Plate 7	12	0.417	4.8	3.2	3.2	1200	11.2
Plate 8	12	1.159	3.2	1.6	3.2	1200	11.7
Plate 9	12	1.85	2.8	1	3.2	1200	12.1

Table 3.5: Plate design and operating conditions of both lab and mill refiners

lected from mill and lab refiner machines. The results presented here stand in good agreement with what Daily et al. [38] and Poullikkas [85] have found and $\frac{P^*}{\rho\omega^3}$ is not exactly but closely proportional to the outer diameter to the 5^{th} power. Moreover, as Herbert and Marsh [5] proposed $\frac{D_i}{D_o} \approx 0.6$ to have the optimum value of refining power, recently this ratio is considered in almost all the disc refiner designs.

From the observed relationships between different variables affecting on hydraulic power, correlation is sought for an exponential multiple regression form. A least square fit curve is applied on all data listed in Table 3.5 and the following values are obtained:

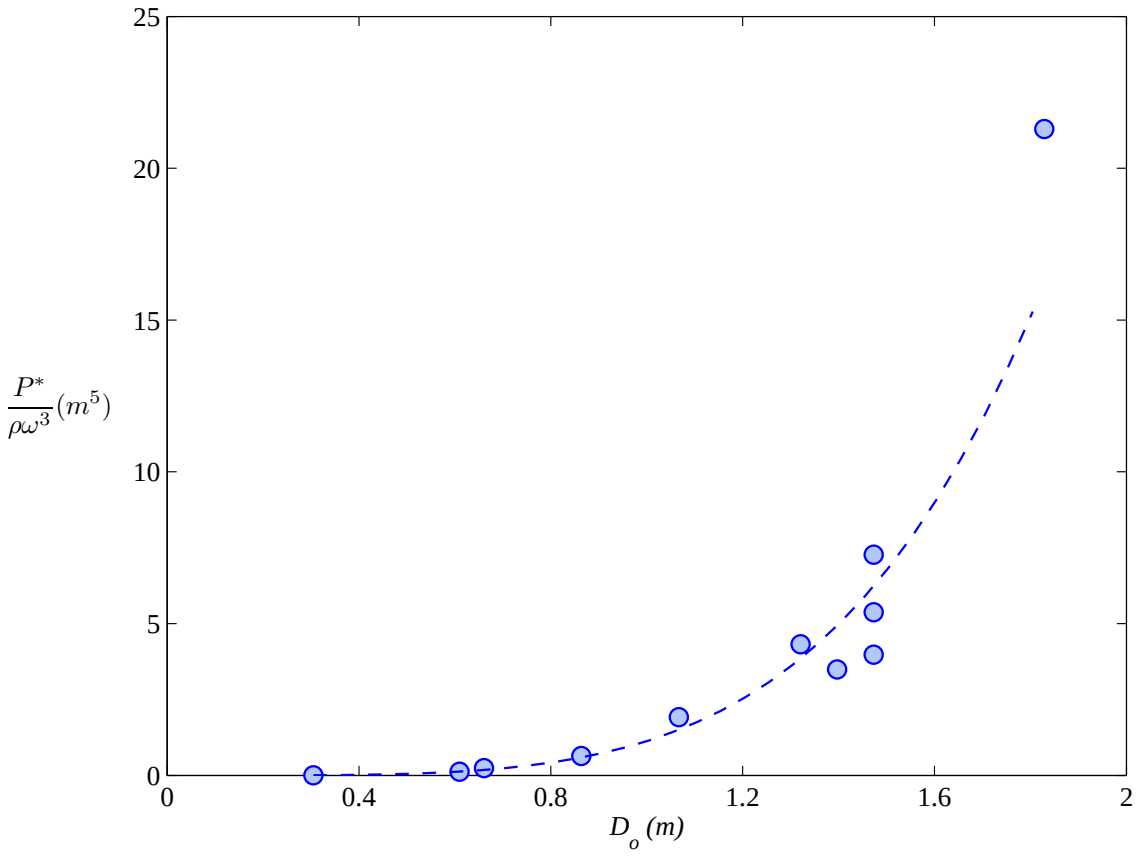

Figure 3.15: Correlation between hydraulic power and diameter for the range of lab and mill plates

$$P_n{}^* = (1.14 \pm 0.2) \left(\frac{T}{R_o}\right)^{0.716\pm0.050} \left(\frac{W}{W+B}\right)^{0.478\pm0.005} \tag{3.7}$$

or

$$Power_n{}^* = (1.14 \pm 0.2)\rho\omega^3 \left(R_o\right)^{4.284\pm0.050} \left(T\right)^{0.716\pm0.050} \left(\frac{W}{W+B}\right)^{0.478\pm0.005} \tag{3.8}$$

Based on these equations, hydraulic power is proportional to $R_o{}^{4.284\pm0.050}$ which

is in good agreement with the formula proposed by AFT/Finebar^{TM} [23]. Both Equation 2.5 and the proposed correlation in Equation 3.8 show that the no-load power depends on T and $\frac{W}{W+B}$, however, in the former equation, the no-load power is linearly proportional to these two variables, but in the latter equation, the no-load power is proportional to $T^{0.716\pm0.050}$ and $\left(\frac{W}{W+B}\right)^{0.478\pm0.005}$.

To determine the quality of the proposed correlation, measured hydraulic power values are plotted with values calculated from the Equation 3.7 in Figure 3.16. The dash lines in the figure indicate a good correlation between both experimental and correlated values, $R^2 \approx 0.91$.

Although there is a good agreement between the measured and predicted values, this figure may occlude the dependence of the data on for all three $12''$ plates. Hence, in Figure 3.17, we present the hydraulic no-load power, for both predicted and measured, as a function of ε to magnify the disagreement, for instance, for a close-up window in the range of $0 < Power_n{}^* < 20$. As expected, $Power_n{}^*$ increases by increasing ε and both graphs follows the same trend. Deviation of measured data from the predicted values can be explained by the experimental errors.

3.4 Conclusion

In this chapter, no-load power was experimentally measured for two pilot refiners with $12''$ and $16''$ diameters for a wide range of gap sizes, groove widths, bar widths, rotational speeds and flow rates with the constant bar angles. The no-load power is considered to have two main components: hydraulic power and pumping power. Hydraulic power goes to overcome the hydraulic and viscous losses in the fluid and the pumping power goes to pumping fluid from the inlet to outlet. Hydraulic power is the dominant power with respect to the pumping power. The effect of the design

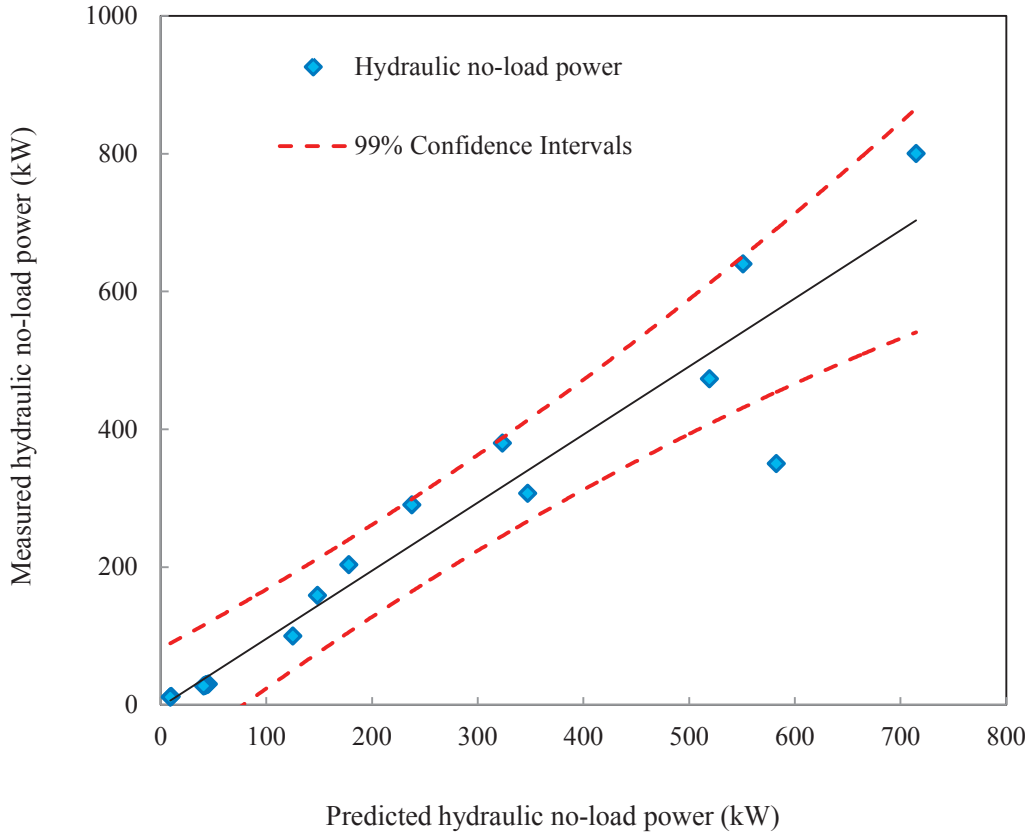

Figure 3.16: Correlation between predicted and measured hydraulic no-load powers for all plates including both lab and mill dimensions

and operating variables was experimentally investigated and the following correlation was proposed:

$$P_n = A\varepsilon^{\alpha} + KC_q Re^{0.2} G^{*-\frac{1}{8}} \tag{3.9}$$

where A and K are constant. The first term on the right presents the hydraulic power and the second term presents the pumping power. The effect of refiner diameter and groove depth on hydraulic power was determined from a series of mill trials and

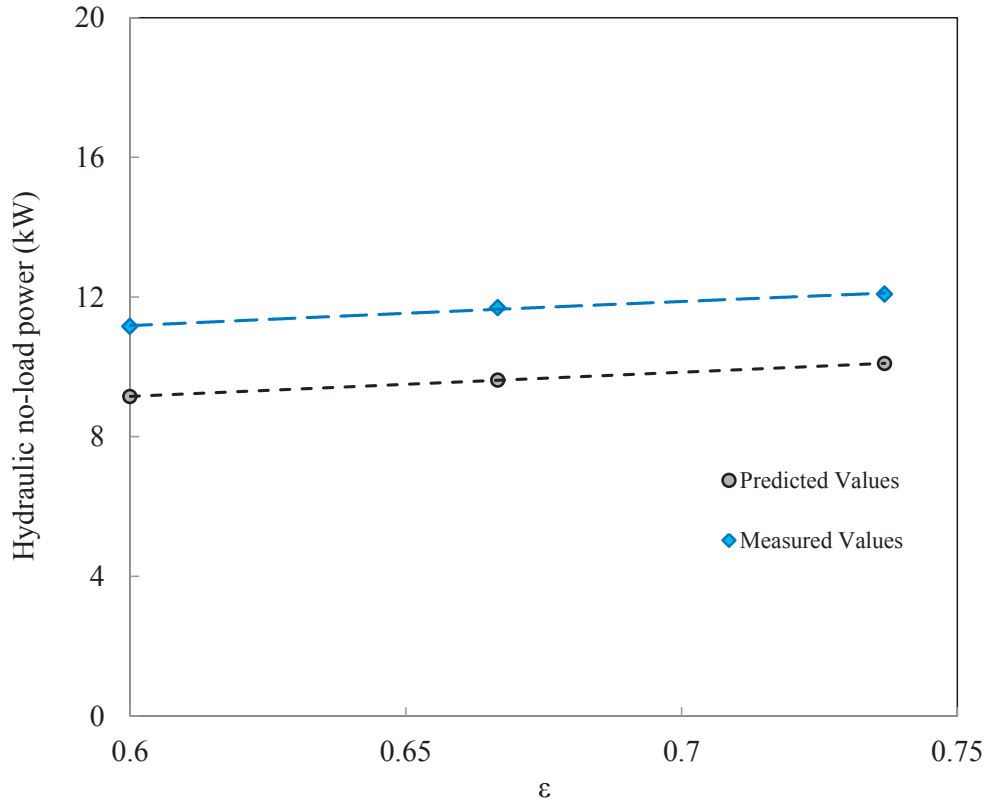

Figure 3.17: Comparison of predicted and measured hydraulic no-load power respect to ε for all 12″ plates

a predictive equation was proposed:

$$Power_n{}^* = (1.14 \pm 0.2)\rho\omega^3 \left(R_o\right)^{4.284\pm0.05} \left(T\right)^{0.716\pm0.05} \left(\frac{W}{W+B}\right)^{0.478\pm0.005} \tag{3.10}$$

It should be noted that these correlations should be applied to estimate the no-load power in LC refiners running with mechanical pulp in the range of our experimental data and they are not recommended to predict the no-load power in LC refiners

running with chemical pulp. The ranges of gap sizes and discs diameters for our date are limited to $1mm$ to $9mm$ and $12''$ to $72''$, respectively.

Based on the above empirical expressions and the obtained data, it can be concluded that:

- Hydraulic power is the dominant component and accounts for more than 90% of total no-load power at wide gaps, depending on the flow rate.

- The power consumption of a smooth disc is exactly proportion to ${R_o}^5$; while for the refiner discs with mounted bars and grooves, the effect of R_o decreases just a little bit (Hydraulic power is not exactly proportion to ${R_o}^5$) and instead, the effect of groove height (T) will be appear.

- The effect of plate pattern can be described by the non-dimensional parameter, $\varepsilon = \frac{W}{W+B}$, which indicates the plates roughness density.

- The no-load power depends on the gap between two discs. This implies that the net power at a specific gap requires that the no-load power is known at that gap.

- Almost no difference between the no-load power of water and low consistency mechanical pulp has been measured.

- The no-load power correlation shows that increase of 20% in $T, Q, \varepsilon, \omega$ and R_o makes about 13%, 5%, 10%, 50% and 62% change in no-load power. This result further suggests that rotational speed and outer diameter have the most significant effects on the no-load power.

Chapter 4

Time-Dependent Cross-Sectional Flow Field of LC Refiners

In this work, we consider the turbulent, time-dependent flow in the channel formed between two periodic corrugated walls (see Figure 4.1). The flow is driven by the steady translation of the upper wall at a rate U, in the direction perpendicular to the corrugations, while the lower wall is stationary. The corrugations in this work are rectangular cavities of depth T and width W with a spacing of B between adjacent cavities. Although this flow occurs in a number of natural and industrial settings, the motivation of this work stems from a Pulp & Paper application, namely, an understanding of the flow field in a low consistency (LC) refiner. One of the open remaining questions in this area is the effect of the time-dependent flow on the efficiency of operation of these devices when the amplitude of the corrugations are large in comparison to the channel spacing G.

Therefore, we propose the following simulations to individually evaluate the effect of gap size on the flow field between the opposing corrugated walls. In §4.1, we present formally the geometry, the equations of motion and the corresponding dimensionless groups which govern the considered flow field. In this section, we describe the computational methodology as well as some validation cases to ensure that our predictions are reasonable. The results from our simulations are presented in §4.2. Here, we begin the discussion by characterizing the time dependent behavior as a

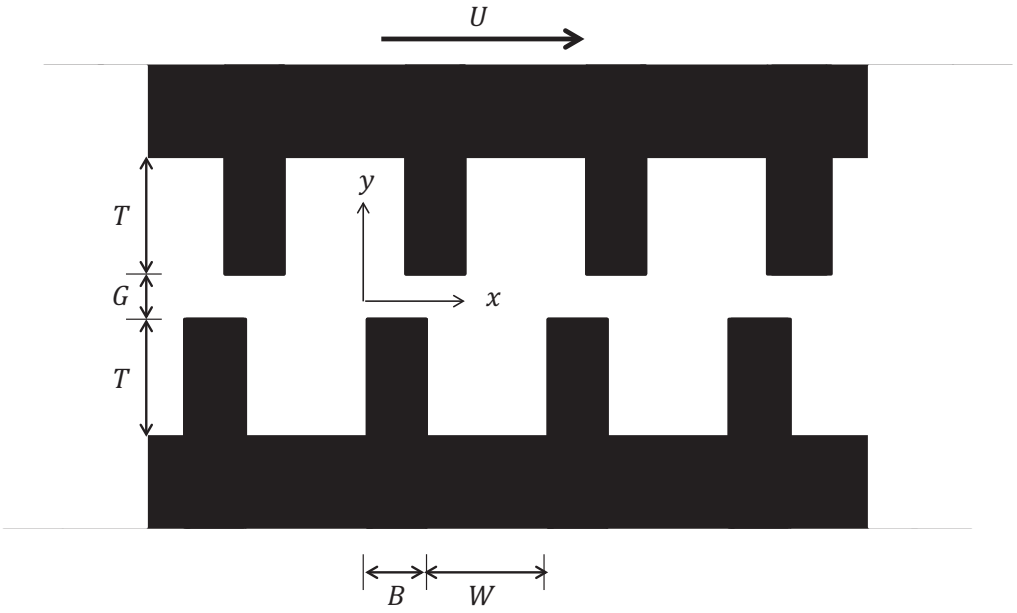

Figure 4.1: Schematic of the corrugated geometry considered. Here the upper wall translates at a constant velocity of U and is separated from the lower plate by a gap G. The corrugations are considered as repeated patterns of rectangular cavities of width $W = 4.8\,mm$ and depth T. The cavities are separated by a spacing of $B = 3.2\,mm$

function of gap size. The time dependent behavior is characterized through fluctuations in the drag coefficient in most simulations. In a number of cases, we further highlight this result through particle tracking using a one-way coupling. The chapter closes with the conclusion section in §4.3.

4.1 Computational framework

In this section, we present the numerical method used to solve the equations of motion for geometry shown in Figure 4.1. When the channel coordinates are scaled with $L = B + W$, the fluid velocity by U and time by L/U, the governing equations in dimensionless form reduce to:

$$\nabla \cdot \mathbf{u}^* = 0 \tag{4.1}$$

$$\frac{\partial u^*}{\partial t^*} + (u^* \cdot \nabla)u^* = -\nabla P^* + \frac{1}{Re_l}\nabla^2 u^* \tag{4.2}$$

where u^* and P^* represent the normalized fluid velocity and pressure; and Re_l is the Reynolds number based on L ($Re_l = UL/\nu$). The channel is bounded in the region

$$y_{max} = G\left(\frac{1}{2} + \frac{T}{G} f_t(x, t; W/L)\right) \qquad \text{Top Wall} \tag{4.3}$$

$$y_{min} = -G\left(\frac{1}{2} + \frac{T}{G} f_b(x; W/L)\right) \qquad \text{Bottom Wall} \tag{4.4}$$

where f_i are the functions describing the shape of the top and bottom walls. The no-slip conditions are applied on the upper and lower walls. Periodic conditions are applied on the left and right faces of the domain (see Figure 4.2).

The equations of motion were solved numerically using a commercially available CFD package, FLUENT, using a 2^{nd} order accurate finite volume method with a realizable $k-\varepsilon$ model as the closure equations for turbulence. There is some indication in the literature that this turbulence model should be adequate for our purposes as both Mesalhy et al. [88] and Shafiqul et al. [53] have used this for driven cavity flow. For all cases, the flow domain was discretized using a non-uniform structured mesh

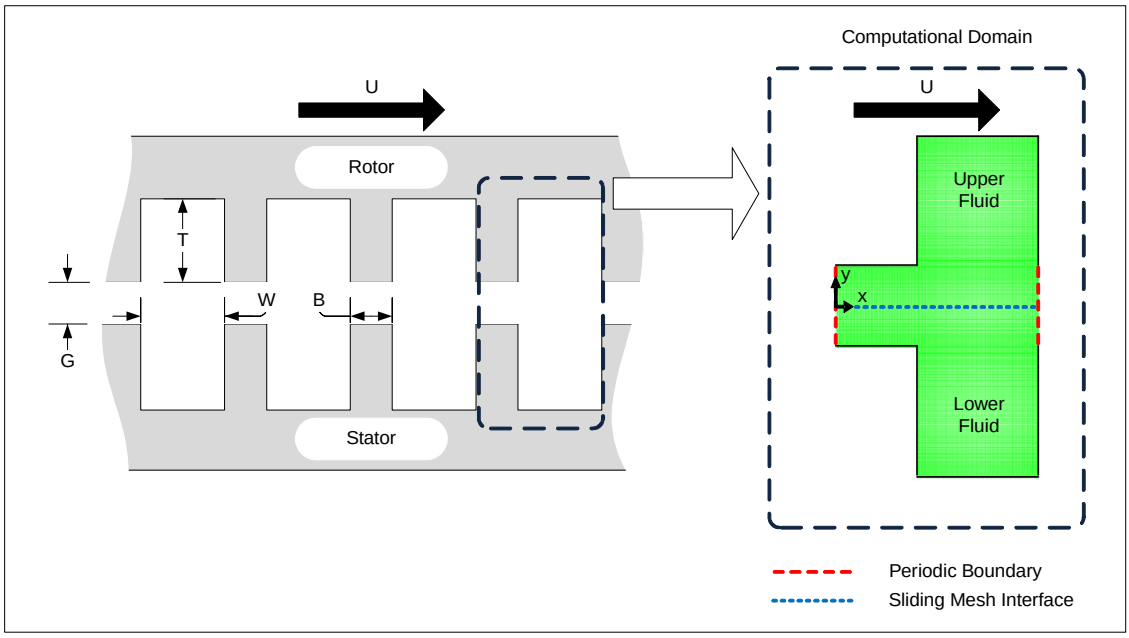

Figure 4.2: Schematic of the physical domain as well as the computational domain. The computational domain is limited to one repeating cavity pattern of length L. Periodic boundary conditions, highlighted by the red dashed lines, on the left and right sides of the domain are shown. A sliding mesh is used dividing the computational domain at $y = 0$

(see Figure 4.2). A sliding mesh was employed to help capture the time dependent components of the solution [89]. The sliding mesh model is the most accurate method to model unsteady cases in FLUENT. Here, the domain is divided in two regions that are treated separately: the moving cavity region and the stationary cavity region. The sliding interface applies to the edge between two zones and at each time step, the upper mesh moves and the fluxes at the sliding interfaces are recomputed. By running the sliding mesh model more computational time is required. The near-wall mesh spacing was set so that the distance away from the wall of the first node satisfied the criteria $y^+ < 1$. By doing so we were able to resolve the flow field in the laminar sublayer through an enhanced wall treatment method. To reduce the computational time, the steady-state solution was used to initialize the computation.

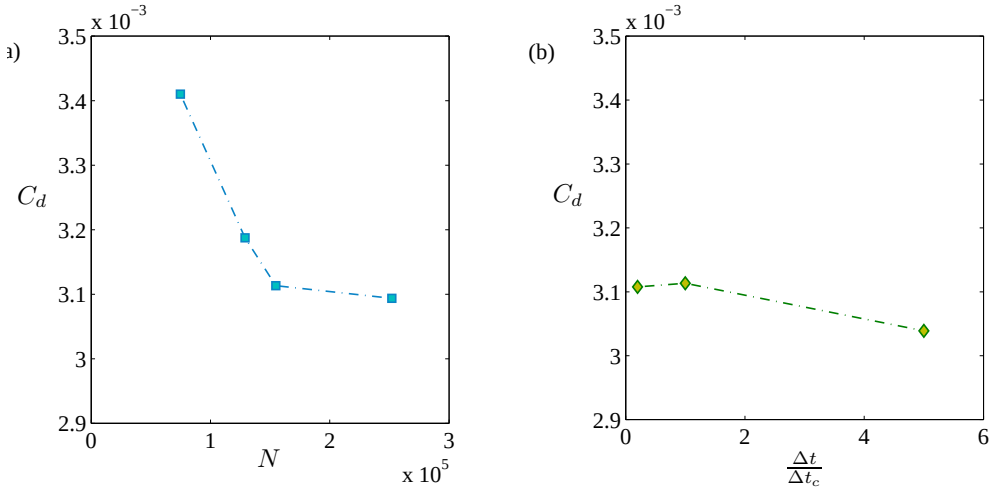

Figure 4.3: Characterizing the sensitivity of the solution to the mesh size and time steps. In (a), the mesh density dependency N is shown as a function of C_d using a time step of $\Delta t = 2 \times 10^{-7} s$. In (b), the effect of time step is shown for the case with $N = 154800$. Here $\Delta t_c = 2 \times 10^{-7}\, s$. In both simulations: $Re_l = 1.6 \times 10^5$, $B/L = 0.4$, $T/L = 0.4$ and $G/L = 0.25$.

Here, the SIMPLE [90] methodology was used for the pressure-velocity coupling. Once initialized, a pressure-implicit operator splitting (PISO) method [89, 90] was used for the unsteady calculations. Convergence was achieved when the residuals of all variables were less than 1×10^{-7} and periodic behavior was observed in the drag coefficient.

In chapter 3, we experimentally showed that the measured no-load power for LC refiner when running with mechanical pulp is almost the same as when it runs with water. Thus, in this study, we consider water as the fluid between two corrugated walls with the density of $998.3 kg/m^3$ and viscosity of $0.001003 kg/m.s$.

At this point, we turn our attention to the precision of the numerical estimates and characterize the dependency of the solution on mesh size and size of the time step. To do so a series of cases were considered in which we estimate drag coefficient C_d as a function of the number of grid points (N). Here, drag coefficient covers both

pressure drag and shear stress drag. As the drag coefficient varies both temporally and spatially, we report

$$C_d = \frac{U}{L^2} \int_0^{\frac{L}{U}} \int_0^{L} C_d(x, t; N) dx dt \tag{4.5}$$

In Figure 4.3, we consider the sensitivity of the solution to mesh size and show that C_d diminishes with an increasing number of grid points. With $N \geq 1.5 \times 10^4$, we consider the solution to be grid independent. In addition to this, it was important to choose the appropriate time step $\Delta t = \Delta x / U$ where Δx is the smallest grid size at the interface of moving and stationary regions in the direction of U. Here we set the characteristic time of the problem to $\Delta t_c = 2 \times 10^{-7}\, s$ for $Re_l = 1.6 \times 10^5$.

Using the method outlined by Celik [91], the numerical uncertainty in the fine grid solution was determined to be $\pm 0.18\%$. We attempt to further evaluate our numerical setup by comparing the results to experimental data of lid-driven cavity flow collected by Friesing [92](see Figure 4.4). The cavity in this case is three-dimensional and the ends are sealed. We compare the effect of varying the aspect ratio of the channel T/W in terms of the relative increase in the drag coefficient, in comparison to that over a flat plate, i.e. $C_d/C_f - 1$, where C_f is the drag coefficient for a flat plate. As shown, the numerical simulations approximate the experimental data reasonably well, especially when T/W is large. Larger discrepancies are evident with $T/W \approx 0.146$. We attribute the differences due the differences in the geometries simulated: we are conducting a 2D simulation with a corrugated wall passing over a system of cavities while Friesing [92] considers lid-driven flow in a long thin cavity.

Finally, with this numerical setup two separate studies were performed. In the first study we examine the effect of G and investigate the flow field at fixed L and T. In the second study, we examine the interaction between opposing cavities by

	G/L	T/L	W/L	Re_l
Series 1	$0.0625 - 1.25$	0.4	0.6	$0.4 - 6.4 \times 10^5$
Series 2	0.0625 & 1.25	0.4	0.6	3.2×10^5

Table 4.1: A summary of the numerical conditions tested. In Series 1, we examined the effect of Re and the spacing between the plates G/L on the flow field. The numerical simulations were conducted with $B/L = 0.4$. In total, 30 simulations were conducted. In series 2, we employed particle tracking, as a passive scalar, for 2 different gap sizes; $G/L = 0.0625$ and $G/L = 1.25$.

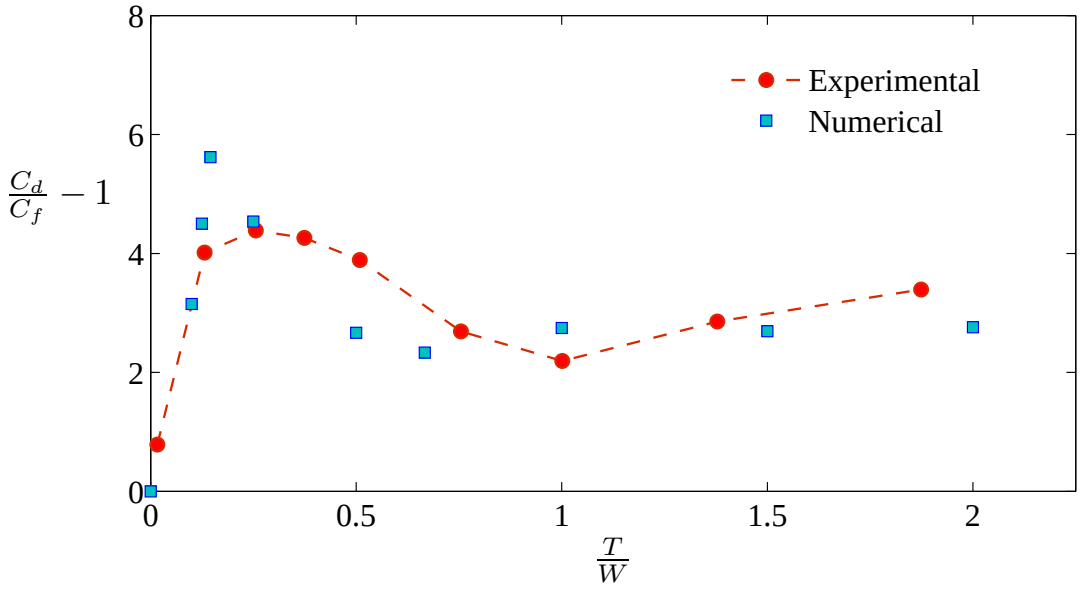

Figure 4.4: A comparison of the numerical solution of two opposing corrugated cavities passing over each other to that of flow in a 3D channel driven by a moving lid measured by Friesing in 1936. The numerical simulations were conducted with $Re_l = 4 \times 10^4$, $G/L = 0.25$ and $B/L = 0.4$.

introducing a passive scalar into the simulation, at a certain location, and examining it spread through the domain. A listing of the numerical studies conducted are given in Table 4.1.

4.2 Results and discussion

We begin the examination of the results and consider the effect of the gap size G on the flow field. The data that we will consider is given as Series 1 in Table 4.1 and as shown the aspect ratio of the cavity is held constant. Before we proceed to the main findings in this series of simulations, it is instructive to examine phenomenologically the time dependency created by opposing cavities. This is shown in Figure 4.5. The first observation that can be made from this figure is that the flow field in the cavities of the lower stationary wall is characterized by one dominant vortex. Seemingly, there appears to be no vortex on the top wall, but this observation is incorrect as the presence of the vortex is masked by the translation of the wall. If we examine the stream function (see Figure 4.6), we do indeed, find that a vortex is present on the top wall, with the same features of that on the bottom wall. If we continue to examine the velocity field as a function of non-dimensional time ($t^* = Ut/L$), we see that at $t^* = 0.2$, the vortex in the central horizontal plane deflects upwards and extends into the gap between the opposing cavities. The vortex in the cavity appears to be skewed to the right. Following this, and in particular at $t^* = 0.8$, a similar feature is apparent but in this case, the vortex extends into the central portion and is skewed somewhat to the left. The pressure field (see Figure 4.7) displays this unique behavior when the vortex is skewed left or right; it can be seen that a continuous connected low pressure region exists across the opposing cavities. Clearly, time-dependent behavior is apparent in this case.

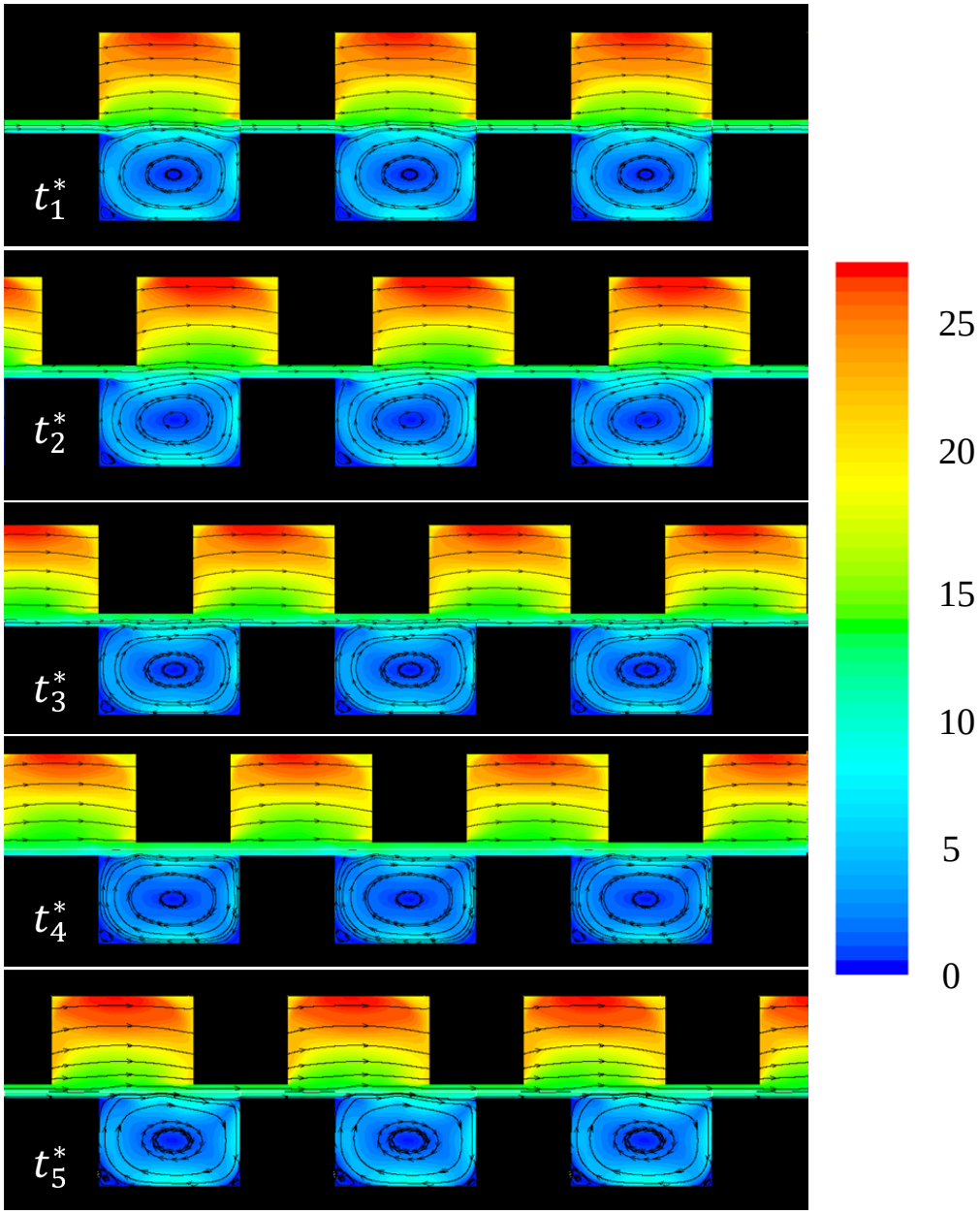

Figure 4.5: Estimates of flow field when $Re_l = 1.6 \times 10^5$, $G/L = 0.0625$, $T/L = 0.4$ and $B/L = 0.4$. The streamlines are shown superimposed on the norm of the velocity field. This is traditionally called the "speed" and the color map of the speed is dimensional with units of m/s. The upper wall is translating from left to right at a velocity of $20\,m/s$. The time steps have been scaled by the periodic time L/U and are presented at $t^* = [0, 0.2, 0.4, 0.6, 0.8]$.

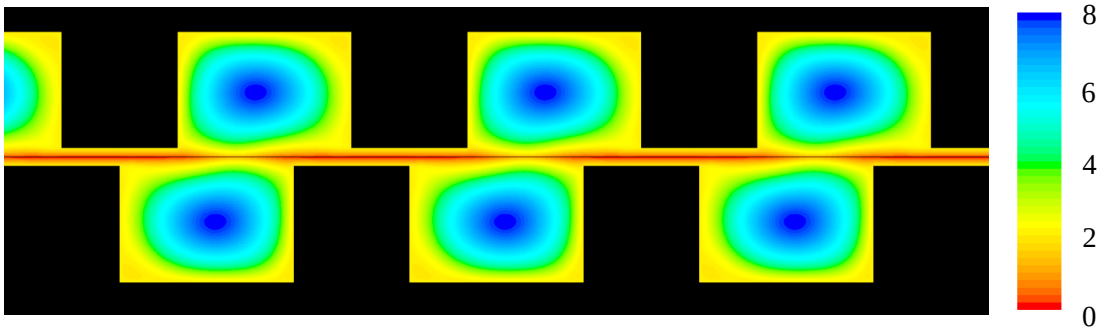

Figure 4.6: Estimates of the stream function when $Re_l = 1.6 \times 10^5$, $G/L = 0.0625$, $T/L = 0.4$ and $B/L = 0.4$. The upper wall is translating from left to right at a velocity of $20\,m/s$. The color map represents the stream function at $t^* = 0.2$ and is given in units of kg/s.

In contrast to this, we present another representative case in which we display another characteristic flow field (see Figure 4.8). This simulation was conducted at larger G and what is evident is that the flow field is steady. This is not unexpected upon examination of the governing equation. As shown in Equation 4.3, the term that causes the time-dependency in flow diminishes by increasing the gap and consequently, flow behaves as Couette flow between two parallel plates at wide gaps.

In order to characterize this effect in a more succinct manner, we examine the drag coefficient. We do so by examining the drag coefficient as a function of time, $C_d(t)$, defined as

$$C_d(t) = \frac{1}{L}\int_0^L C_d(x,t;N)dx \tag{4.6}$$

This is shown in Figure 4.9 where we see that the temporal variations increase with diminishing gap size and what is evident in this figure is that the variations are negligible with $G/L \geq 0.75$.

We define the flow field to be at steady-state when the coefficient of variation,

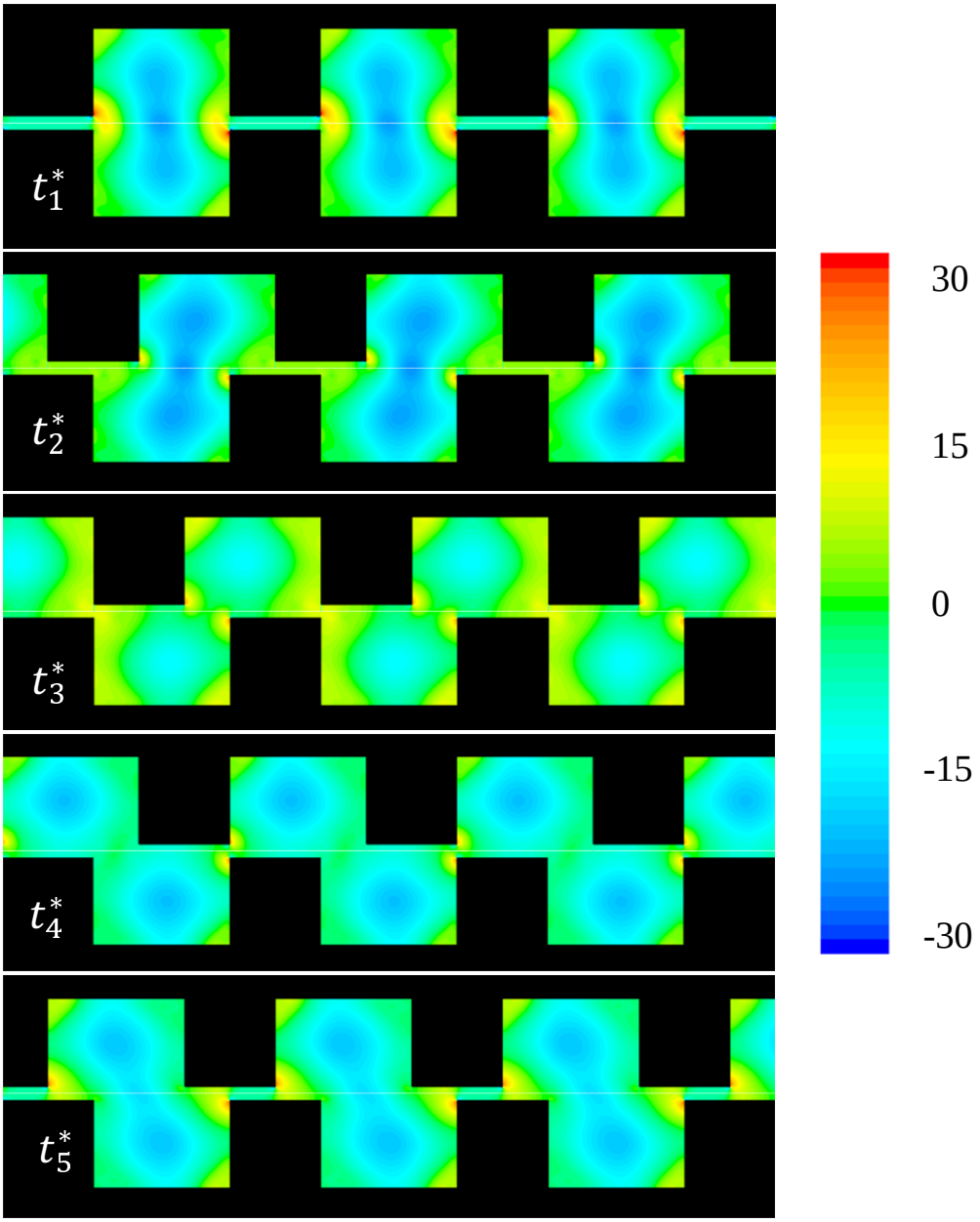

Figure 4.7: Estimates of the pressure field when $Re_l = 1.6 \times 10^5$, $G/L = 0.0625$, $T/L = 0.4$ and $B/L = 0.4$. The upper wall is translating from left to right at a velocity of $20\,m/s$. The color map represents the pressure field and is given in units of kPa (gage). The time steps have been scaled by the periodic time L/U and are presented at $t^* = [0, 0.2, 0.4, 0.6, 0.8]$.

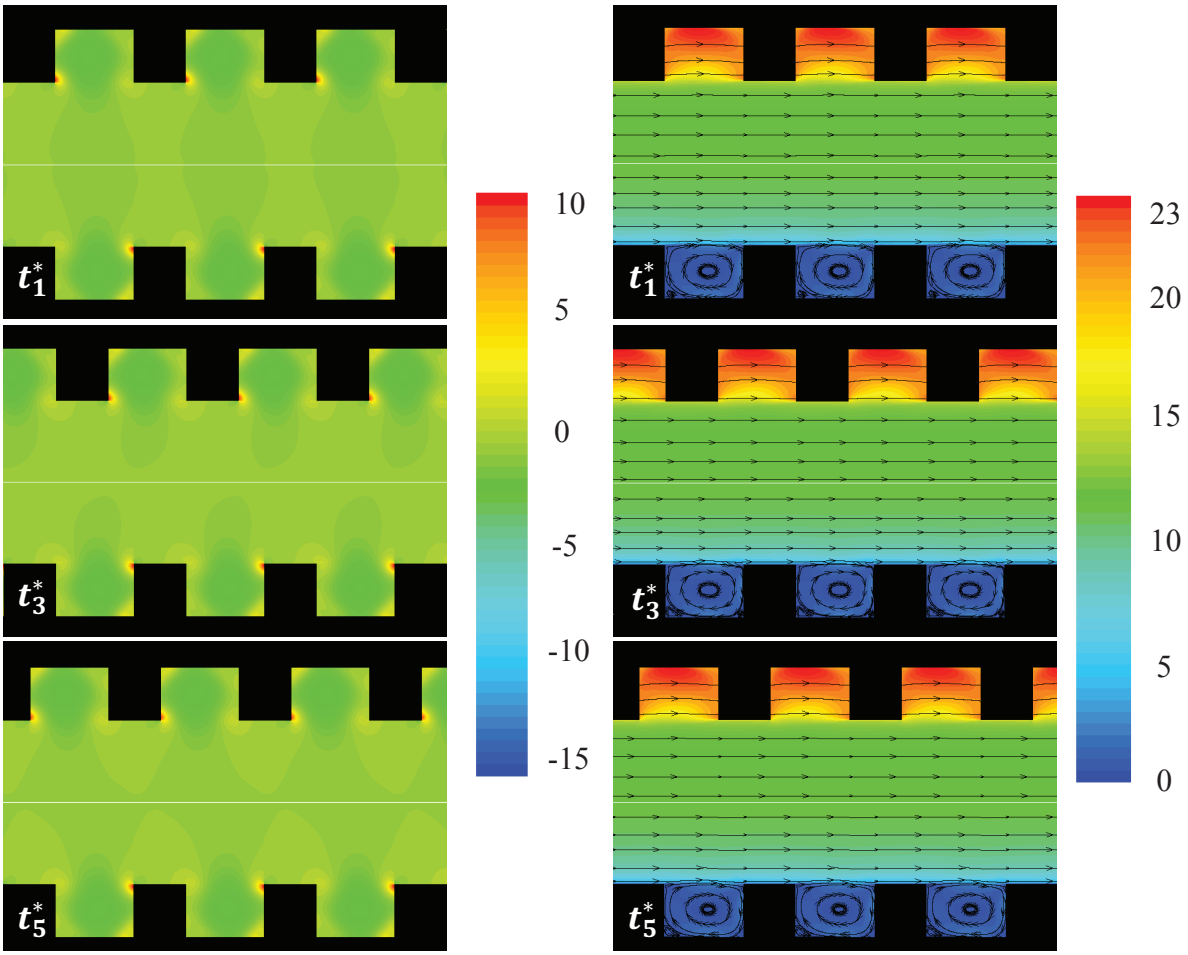

Figure 4.8: Estimates of flow and pressure fields when $Re_l = 1.6 \times 10^5$, $G/L = 1.25$, $T/L = 0.4$ and $B/L = 0.4$. The upper wall is translating from left to right at a velocity of $20\,m/s$. The color map of the velocity field and pressure distribution are respectively given in units of m/s and kPa (gage). The time steps have been scaled by the periodic time L/U and are presented at ${t_2}^* = 0.2$ and ${t_5}^* = 0.8$.

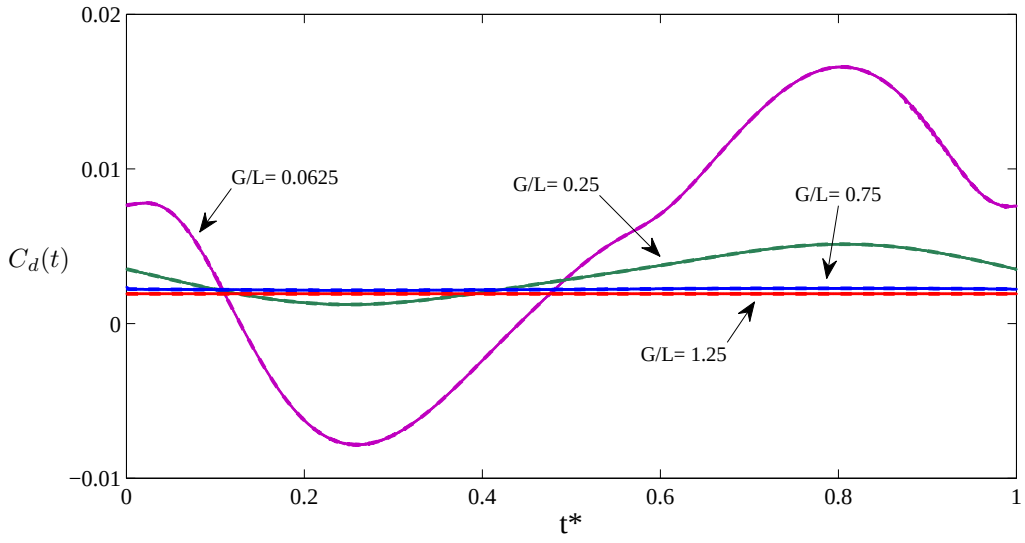

Figure 4.9: Estimates of drag coefficient as a function of time for various G/L. Here $Re_l = 1.6 \times 10^5$, $T/L = 0.4$ and $B/L = 0.4$.

i.e. the standard deviation (σ_{C_d}) divided by the mean (C_d), is less than 0.05. A large number of simulations were conducted in which we attempted to define the boundary between steady and unsteady flow. Figure 4.10 displays the contours of $\frac{\sigma_{C_d}}{C_d}$ as a function of both G/L and Re. The white line that divides the graph in two regions shows the conditions of gap size and the moving cavity velocity where flow is either steady or unsteady.

Depending on Reynolds number, transition from unsteady flow at small gaps to steady flow at wide gaps takes place at different values of G/L; i.e. transition for flow fields with Re of 0.4×10^5 and 6.4×10^5 appears at G/L of 0.67 and 0.75, respectively. In other words, in terms of time-dependent parameter shown in Equation 4.3, ($\frac{T}{G} f_t(x, t; W/L)$), the flow is defined as steady when the gap between the plates is greater than twice the depth of the cavity. Pulsating flow is established when the gap size diminishes below this limit.

At this point, we would like to examine the behavior of the flow field further

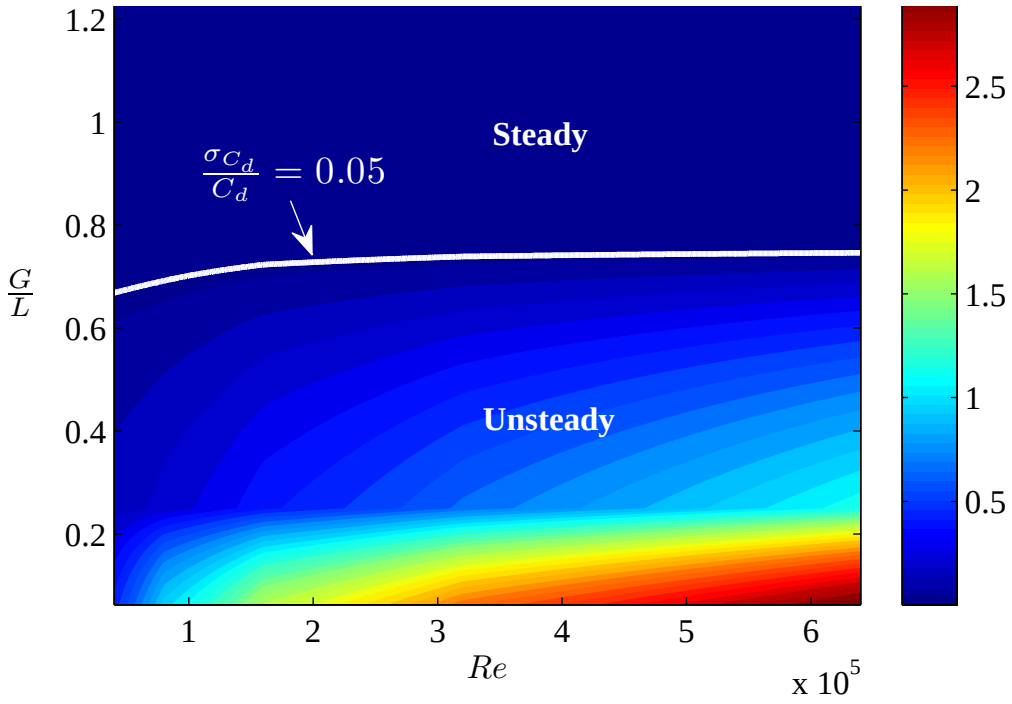

Figure 4.10: Estimate of the bound between steady and unsteady behavior. A listing of the range of the simulations is given as Series 1 in Table 4.1. The boundary between steady and unsteady is drawn as the white line in the figure and represents a threshold when the coefficient of variations diminishes below 0.05. The contour in this plot is coefficient of variation as defined by $\frac{\sigma_{C_d}}{C_d}$.

and address the question "is fluid exchanged between the rotating and stationary cavities?". To do so, we examine the evolution of a passive particle, introduced at different locations in either steady (large gaps) or unsteady (small gap) cases. In this one-way coupled simulation, we released particles at three different locations:

- Position 1 - in the channel formed between the two walls
- Position 2 - in the moving cavity on the upper wall
- Position 3 - in the stationary cavity on the lower wall

These positions are highlighted in Figure 4.11. Six simulations are reported and conditions under which they were performed are given in Table 4.1. We begin the discussion of these results by defining the order in which we will present the results. We discuss the results in the order of the position and present percentage of time the particles remained at a particular elevation $-1 \leq Y^* \leq 1$ in the domain where $Y^* = \frac{y}{T+G/2}$ (see Figures 4.12-4.14). For each figure, Y^* represents the normalized vertical positions of particles in one of these zones: moving cavity, stationary cavity or the area between two cavities. Table 4.2 summarizes the range of Y^* for each zone depends on the gap size. The total calculated time for tracking the location of each particle is $120L/U$.

Location of particles	$G/L = 0.0625$	$G/L = 1.25$
Moving cavity	$0.0725 \leq Y^* \leq 1$	$0.61 \leq Y^* \leq 1$
Spacing between two cavities	$-0.0725 \leq Y^* \leq 0.0725$	$-0.61 \leq Y^* \leq 0.61$
Stationary cavity	$-1 \leq Y^* \leq -0.0725$	$-1 \leq Y^* \leq -0.61$

Table 4.2: Range of Y^* for three different regions of moving cavity, stationary cavity and the spacing between these two cavities

As an example, in Figure 4.12, the particle was released at Position 1 and we see that under unsteady condition, the tracer particle diffuses over the entire domain. In

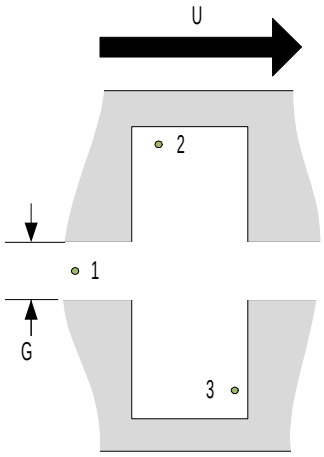

Figure 4.11: A schematic of the positions where the particles are released for the simulations.

contrast with this, under steady condition, we find that the tracer particles remain on a steady trajectory and at nearly the same elevation it was released. For the other two cases simulated we find somewhat similar results. As shown in Figures 4.13a and 4.14a, the particles spread over the entire domain under the unsteady conditions. At steady state (see Figures 4.13b and 4.14b), the particles remain in the cavity in which they were released. Here the particles follow the motion of the vortex in the cavity.

4.3 Conclusion

In this chapter, two-dimensional numerical simulations have been performed for a fully developed turbulent flow in the space between two opposing cavities; one cavity is moving and the other is stationary. This case resembles the flow field in the cross section of refiner. Due to complexity of three-dimensional flow in the refiner, this geometry can give insight into some features of tangential flow field inside the

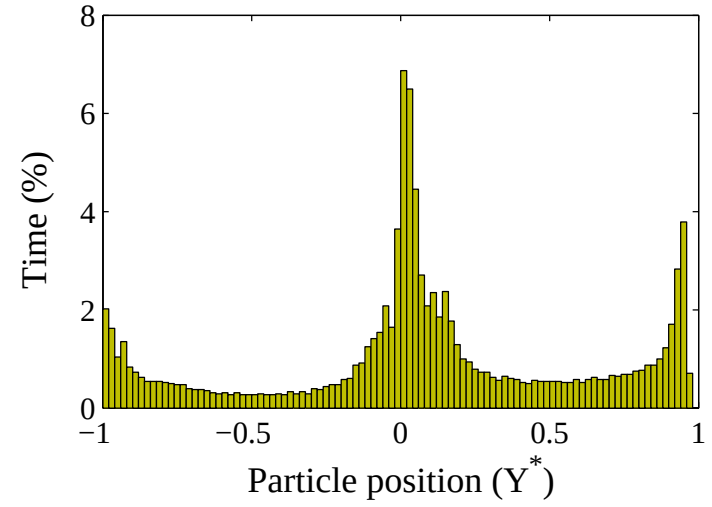

(a)

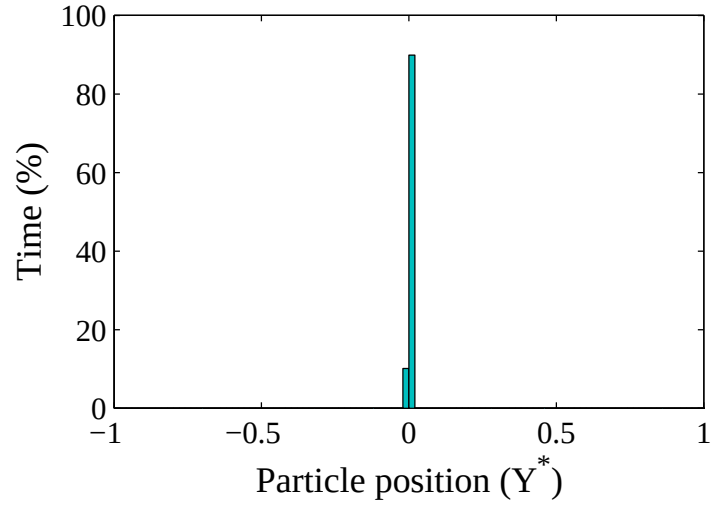

(b)

Figure 4.12: Histogram of the particle positions released from Position 1 in (a) unsteady and (b) steady flow fields.

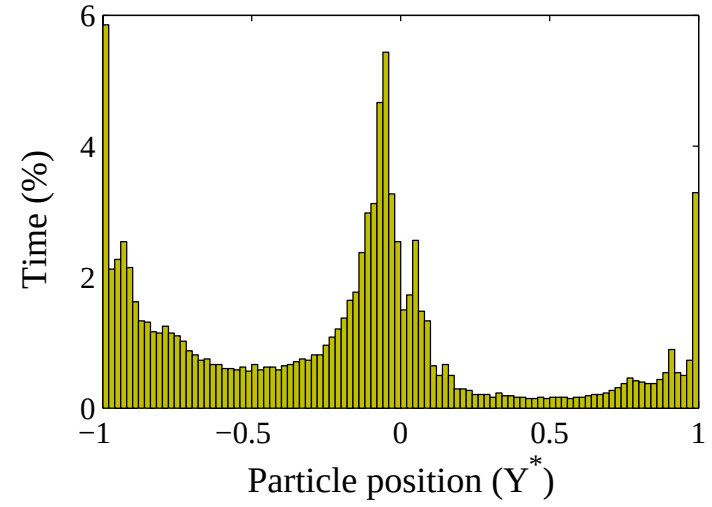

(a)

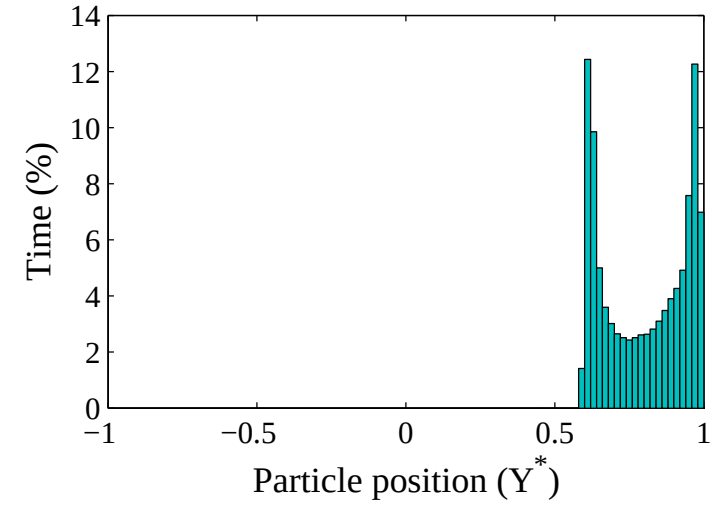

(b)

Figure 4.13: Histogram of the particle positions released from Position 2 in (a) unsteady and (b) steady flow fields.

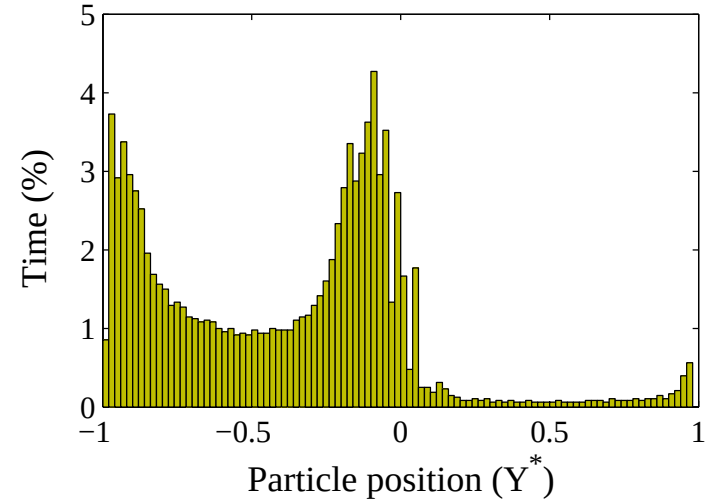

(a)

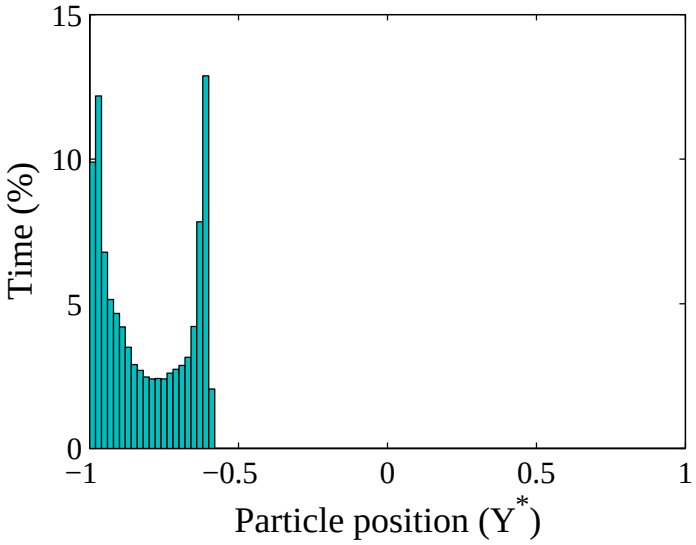

(b)

Figure 4.14: Histogram of the particle positions released from Position 3 in (a) unsteady and (b) steady flow fields.

cavities of a LC refiner. Unsteady simulations have been conducted to obtain details of flow field for different gap sizes and velocities. For the range of parameters studied, two characteristic flow fields were identified: unsteady and steady flows. Results demonstrated that the temporal variations which arise from the presence of repeated corrugations on the opposing walls, diminish with increasing gap size. We defined the flow field as steady-state when the coefficient of variation, i.e. the standard deviation (σ_{C_d}) divided by the mean drag coefficient (C_d), is less than 0.05. Also, we showed that the flow field is periodically unsteady when the gap size is small.

The most significant part of this work is found when we consider particle transport between the cavities. We find that particles are transported to the region near the leading edges of the bars only under the conditions of unsteady flow. Particle transport is enhanced by the presence of the large pressure gradients formed under the conditions of unsteady flow which arises by decreasing the gap size.

Chapter 5

Effect of Cavity Aspect Ratio on the Cross-Sectional Flow Field

Flow in a refiner is three-dimensional, and as such, is influenced by both radial and tangential flows. The radial flow accounts for flow in the longitudinal direction of bars and grooves whereas tangential flow is induced by the rotation of the rotor. The present chapter serves to extend our understanding of flow field in the tangential direction of refiners. Hence, we explore the effect of cavity depth and wall velocity on the flow field. The rest of geometrical parameters are kept constant in this study. In this chapter, as in chapter 4, two-dimensional simulations are performed of the flow in the channel formed between two periodic corrugated walls.

In the context of the existing refining literature (see chapter 2) our study is somewhat unique in that we examine the effect of groove depth on the hydrodynamic drag. These results lead us to extend our understanding of no-load power as many authors indicate that drag increases with depth. An outline of this chapter is as follows. Below, in §5.1 we give a brief outline of the the computational domain, boundary conditions and numerical schemes. We open up §5.2 by introducing the relevant governing equations, then present the results regarding the effect of cavity depth on both flow pattern and the drag coefficient and finally the chapter finishes with concluding remarks in §5.3.

	G/L	T/L	W/L	Re
Series 3	0.25	0-5	0.6	$0.4 - 6.4 \times 10^5$

Table 5.1: A summary of the numerical conditions tested. In Series 3, we examined the effect of Re and aspect ratio T/W on the flow field. In total 72 simulations were conducted.

5.1 Computational framework

Having fixed the gap size between two corrugated walls, a series of two-dimensional simulations are performed using FLUENT. The flow of interest passes through two opposing corrugated walls (see Figure 4.1). As explained in Chapter 4, a non-uniform structured grid with sliding mesh method and realizable $k - \varepsilon$ turbulent model are used. Numerous simulations are carried out for various depth size with upper wall velocity of U. Table 5.1 summarizes the specifications of computational domain in which the variables T/L and Re are varied. In total 72 simulations were conducted.

As shown in Figure 4.2, there are two walls confined flow and impose the no-slip conditions to the flow. The lower wall is stationary and the upper wall moves at a velocity, U. As a consequence, the grid in the stator remains stationary and the grid in the rotor moves by the same velocity as the moving wall. Periodic conditions are applied on the left and right faces of the domain.

With the above-mentioned numerical setup (more details in Chapter 4), a series of studies were performed to examine the effect of aspect ratio of the cavities (T/W) for the steady flow field and categorize the flow using a similar scheme to that outlined by Perry et al. [55].

5.2 Results and discussion

In this section, we present the numerical results to show the effect of cavity aspect ratio by keeping the bar and cavity widths constant; thus the only variable is the cavity depth. To study the effect of cavity depth on the flow field, it is convenient to show the dependent variables of the problem by normalizing the Navier-Stokes equation using the moving cavity velocity (U) and the domain dimensions (L, T). The Navier-Stokes equation in the x-dimension is given as:

$$u^* \frac{\partial u^*}{\partial x^*} + v^* \frac{\partial u^*}{\partial y^*} = -\frac{\partial P^*}{\partial x^*} + \frac{1}{Re_l} \left(\frac{\partial^2 u^*}{\partial x^{*2}} + \left(\frac{L}{T} \right)^2 \frac{\partial^2 u^*}{\partial y^{*2}} \right) \tag{5.1}$$

This normalized form of Navier-Stokes shows that the two affecting parameters on the flow field are Reynolds number, Re_l, and cavity ratio, $\frac{T}{L}$. Since bar width is constant, in this section all the results are presented with respect to the more conventional term of T/W where $0 \leq \frac{T}{W} \leq 5$. As described in §2.4, cavities with $\frac{T}{W} < 0.25$ are categorized as k-type cavities. Also, cavities with $0.25 < \frac{T}{W}$ are categorized as d-type cavities where all the laboratory and industrial scale refiners cavities have the aspect ratios that insert them in this type.

In term of energy consumption, Figure 4.4 depicts drag coefficient as a function of $\frac{T}{W}$ for $Re = 0.4 \times 10^5$. In the range of d-type cavities, drag coefficient decreases by increasing the cavity depth, up to $T/W \approx 0.5 - 1$ and then, after this range of cavity aspect ratio, C_d slightly goes up for higher cavity depths.

On the other hand, in term of flow field, Figure 5.1 depicts the flow pattern inside three different cavity geometries. Based on the number of vortices inside each cavity, lets introduce a new classification for cavities:

- Type I: This type covers all the k-type cavities that have no main vortex.
- Type II: This type includes all d-type cavity ratios that have just one primary vortex.
- Type III: All d-type cavity ratios that have more than one vortex.

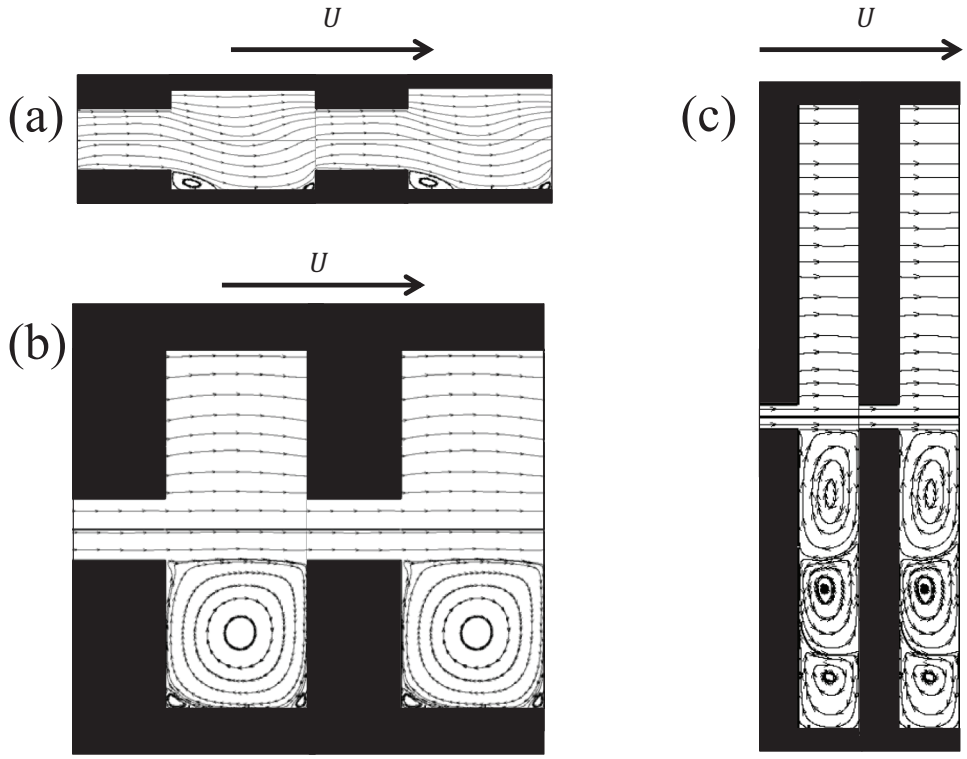

Figure 5.1: Flow pattern in three different cavity aspect ratios when $Re = 1.6 \times 10^5$. (a) k-type cavity with no vortex ($T/W = 0.146$). (b) d-type cavity with one main vortex ($T/W = 1$). (c) d-type cavity with more than one vortices ($T/W = 5$).

Based on the refining point of view, cavities are expected to be high enough to let the proper amount of flow pumped in the refiner and low enough to refine the large amount of fibres, while having the minimum drag coefficient. Therefore, if the cavity depth is too high, there may be multiple primary vortices inside the cavity. In

this case, in spite of increasing the hydraulic capacity, some fibres could be trapped in the lower vortices. It results in less fibres treated. If the groove depth is too low, then hydraulic capacity would be low and also it may result in high drag coefficient.

In order to better explain the characteristic of various types of refiner cavities in terms of drag coefficient, hydraulic capacity and fibers treatment, we would like to combine our knowledge regarding the energy consumption and flow pattern inside different cavities. In this regards, the domain of each type is distinguished by the dashed lines on the drag coefficient contours for different cavity ratios and Reynolds numbers (Figure 5.2):

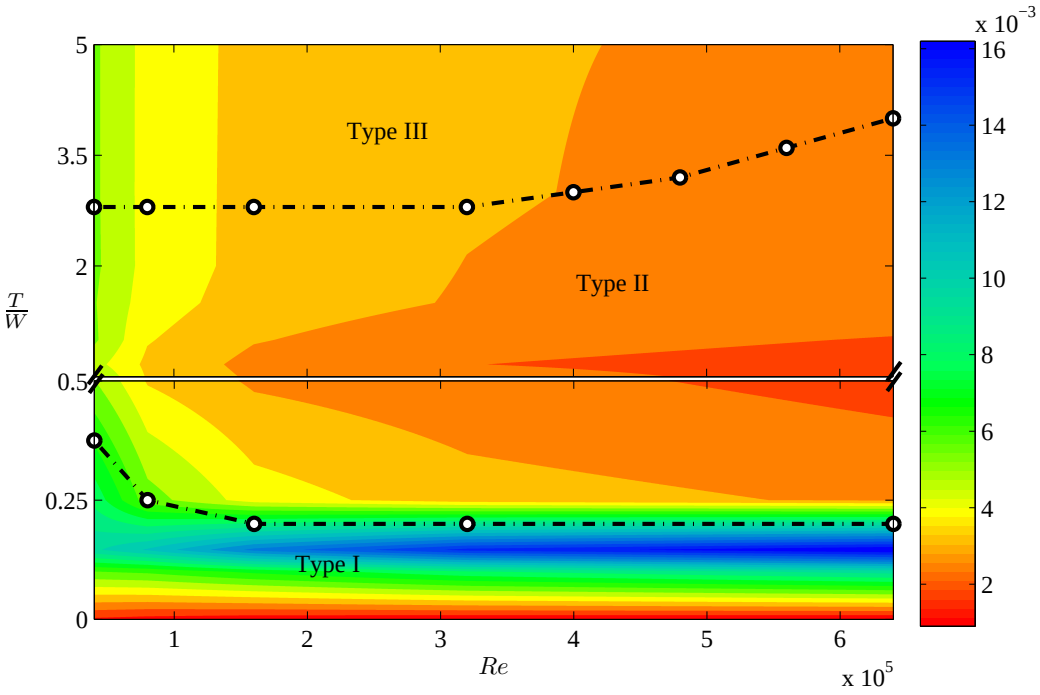

Figure 5.2: Contours of C_d respect to the variations of cavity depth and Reynolds number.

- Type I covers all the k-type cavities where there is no primary vortex inside the cavity. By increasing the T/W from 0 up to 0.146 drag coefficient goes up

and reaches its maximum at $T/W = 0.146$. After this point, C_d goes down by increasing the cavity ratio. Therefore, Type I is the area that the maximum drag coefficient coincides with the lowest hydraulic capacity. Industrial refiners can hardly be categorized in this group. Transition between Type I and Type II takes place at different cavity ratios which directly proportional to the Reynolds number.

- Type II: This type includes all cavity ratios that have just one primary vortex and relatively has the lowest drag coefficient. Depending on the Reynolds number, the specific ratio that the number of primary vortices changes from one to two can be varying between 2.5 to 4. At higher Reynolds numbers the mainstream flow induces higher shear at the top of the cavity increasing momentum transfer to the cavity fluid. The primary vortex formed in the cavity then has elevated angular momentum and is able to sustain its form for larger aspect ratios at higher Reynolds numbers as depicted in Figure 5.2.

- Type III: All cavity ratios that have more than one vortex are categorized in this group. In this area, increasing the cavity ratio makes slight changes in the drag coefficient while provides higher hydraulic capacity. On the other hand, fibres may trap in the lower main vortices which makes some fibres leaving refiner untreated.

As a result, among all types of refiner cavities, Type I cavities lead to high energy consumption and low hydraulic capacity and Type III cavities could result in unsuccessful refining action. So the only desirable category to fulfill the refining mission with the minimum drag coefficient is suggested as Type II.

5.3 Conclusion

We ran two-dimensional simulations of the flow between two moving and stationary cavities to evaluate the effect of cavity depth on flow field at the cross-section of LC refiner. All the simulation in this chapter were performed for the steady flow field. We identified three characteristic flow fields for cavity depth variation based on the number of vortices formed within the cavity and the drag coefficient.

Type I covers all the k-type cavities where there is no primary vortex inside the cavity. In this flow field, the maximum drag coefficient coincide with the lowest hydraulic capacity which make these range of cavity ratios unqualified for the refining purpose. Type II includes all cavity ratios that have just one primary vortex and relatively has the lowest drag coefficient in the d-type cavities. Type II cavities were suggested for the refining purpose. In this range of cavities, drag coefficient is minimum while we have more fibers successfully treated. All cavity ratios that have more than one vortex are categorized in Type III. Despite Type III provides maximum hydraulic capacity, fibres may trap in the lower main vortices which makes some fibres leaving refiner untreated.

Chapter 6

Summary of Thesis and Future Research Direction

6.1 Summary of contributions

The main contributions of this thesis can be summarized in three categories: New empirical correlation to estimate no-load power in low consistency refining, the effect of gap size on the time-dependent flow field in refiner, and the effect of groove depth on refiner flow field.

1. **New empirical correlation to estimate no-load power**

   The experimental data were collected over a wide range of affecting parameters on the no-load power consumption in low consistency refiners.

   - A new statistical model was provided for prediction of no-load power, described in terms of two main components: hydraulic and pumping powers.
   - The hydraulic and pumping powers were measured separately and their contributions on the total no-load power were examined for a wide range of gap sizes. Hydraulic power was shown to be the dominant component.
   - In contrast to general belief, no-load power was shown to depend on the plate gap. This implies that knowing the net power at a specific gap requires knowledge of the no-load power at that gap.

2. **Effect of gap size on the time-dependent flow field in refiner**

   A series of unsteady simulations were carried out to investigate the effect of gap size on the cross section of refiner flow field and particle trajectories over a wide range of Reynolds number.

   - We identified two characteristic flow fields, defined by either as steady or unsteady.
   - We found that particles are transported to the region near the leading edges of the bars only under the conditions of unsteady flow.

3. **Effect of groove depth on refiner flow field**

   A series of steady numerical simulations were performed to investigate the effect of groove depth on the cross section of refiner flow field over a wide range of Reynolds number.

   - We found that the aspect ratio of the cavity dictates the number of vortices formed within cavity. With $W/T \to 0$, we find a flow field characterized by multiple vortices with centers aligned on top of each other. As the aspect ratio increases, the number of vortices diminishes.

6.2 Limitations of the study

Although we have made a number of advances, we must also acknowledge some limitations of our experimental and computational studies.

Chapter 3. In terms of experimental work, some major limitations should be listed as:

- Low consistency pulp suspension behaves much like water [93]. In this regard, we applied the same rheological properties for low consistency pulp suspension as water.

- We did not measure the no-load power for very small gaps; i.e. in the order of pulp diameters. At these gaps, the refiner plates clashed when using water. When the fluid accelerated, the internal pressure decreases and the plates are drawn towards another. Usually this is avoided when the gear mechanism for the gap adjustment is accurate enough to hold the rotor in place.

- To develop the total no-load power correlation, we could not find any relationship between the effect of plates design and the pumping power of each plate. It is important to mention that the difference between the pumping powers of the various plates was mostly in the range of experimental error. To calculate the pumping coefficient (K) for all $16''$ plates, we used all the pumping powers for different operating conditions and plate designs and then proposed the correlation only with respect to operating conditions, not the geometrical parameters.

- Each mill no-load power value presents one power value at a random wide gap for the fixed rotational speed and flow rate. This means that we did not have enough data to distinguish the pumping and hydraulic powers. So based on the experimental observations, we considered 90% of the total mill no-load powers as the hydraulic power.

Chapters 4 & 5. In terms of computational study, the main restrictions are as follows:

- It is important to recognize that running the two-dimensional models neglects

some aspects of the flow field in the radial direction as well as the effect of the stationary case around both refiner discs.

- In these chapters, the effect of fibres was neglected and therefore, a pure water flow in the tangential direction was simulated.

6.3 Future research directions

The results in this thesis also provide a strong foundation for future work. This section discusses several lines of research arising from this work which can be pursued.

- To explore the effect of plate design parameters on the no-load power, we have performed two series of experiments with identical plates but different bar and groove widths. A systematic experimental study of other geometrical parameters such as grinding and sectional angles and also groove depth is of practical interest.

- There is a significant disconnect between the experimental study of no-load power and the numerical analysis. It would be great to extend this work to the three-dimensional numerical study to obtain more details of the flow field in the radial direction and its effect on the tangential flow. To accomplish this study, it is better to include the housing around two refiner discs. Numerical approach provides a faster and cost efficient tool to optimize the LC refiner plate design.

- Water has been considered as the fluid between two cavities in our 2D simulations. The next step would be to extend the simulations to investigate the flow field in the case of running water with fibres with various lengths.

- In this thesis, we have focused on the investigation of the no-load power concept

and how the main affecting parameters can change the consumption of this idle power in low consistency refiners. This opens up interesting area to explore how controlling these parameters to minimize the no-load power, affects the refining zone and consequently, the papermaking fibres quality.

Bibliography

[1] R. J. Kerekes, R. M. Soszynski, and T. Doo, "The flocculation of pulp fibres," in *Papermaking Raw Materials: Their Interaction with the Production Process and Their Effect on Paper Properties-Transactions of the Eighth Fundamental Research Symposium*, (Oxford, UK), pp. 265–310, Mechanical Engineering Publications Limited, September 1985.

[2] P. E. Sharpe and J. L. Rodarmel, "Low consistency refiner plate design and selection," *Pulp & paper Canada*, vol. 89, no. 2, pp. 51–57, 1988.

[3] M. Jackson and N. Wild, "Mechanical pulp mills," *Energy Cost Reduction in the Pulp and Paper Industry, Browne, TC tech. ed., Paprican*, p. 15, 1999.

[4] P. Dietemann and J.-C. Roux, "A study of disc refiner running in no-load conditions," *Cellulose chemistry and technology*, vol. 39, no. 5-6, pp. 459–471, 2005.

[5] W. Herbert and P. G. Marsh, "Mechanics and fluid dynamics of a disk refiner," *Tappi J.*, vol. 51, no. 5, pp. 235–239, 1968.

[6] J. Lumiainen, "Is the lowest refining intensity the best in low consistency refining of hardwood pulps?," in *Tappi Press: Papermakers Conference*, (Atlanta), pp. 115–126, 1994.

[7] D. H. Page, "The beating of chemical pulps–the action and the effects," in *Fundamentals of Papermaking, 9th Fundamental Research Symposium*, (Oxford), 1989.

[8] J.-C. Roux, J. F. Bloch, R. Bordin, and P. Nortier, "The net normal force per crossing point: a unified concept for the low consistency refining of pulp suspensions," in *14th Fundamental Research Symposium: Advances in Pulp and Paper Research*, (Oxford), pp. 51–83, 2009.

[9] J. Rihas, "Low consistency refining, theory vs practice," in *3rd International Refining Seminar*, (Atlanta, GA, US), March 1995.

[10] Tappi Stock Preparation Committee, "An introduction to refining variables," *Tappi Journal*, vol. 54, no. 10, pp. 1738–1741, 1971.

[11] T. Lundin, *Tailoring pulp fibre properties in low consistency refining.* Åbo Akademi, 2008.

[12] W. Brecht and W. H. Siewert, "Zur theoretisch-technischen beurteilung des mahlprozesses moderner mahlmaschinen," *Das Papier*, vol. 20, no. 1, pp. 4–14, 1966.

[13] L. Westman, "Idling losses in the low-consistency refining of chemical pulp," *Svensk Papperstidning*, vol. 87, no. 3, pp. R8–R13, 1984.

[14] H. Selder and W. H. Siewert, "Escher wyss fibersorter for the high density screening of recycled fibres," in *Papermakers Conference, Proceedings of the Technical Association of the Pulp and Paper industry*, 1980.

[15] N. Rajabi Nasab, J. A. Olson, J. Heymer, and D. M. Martinez, "Experimental study of low consistency refiner no-load power," in *PAPERCON Conference Proceedings*, (New Orleans, LA), pp. 1539–1551, April 2012.

[16] A. Arjas, J. Huuskonen, and N. Ryti, "Principles of the evaluation of the performance of a beating machine and of the beating result," *Paperi Ja Puu*, vol. 52, no. 4, pp. 269–276, 1970.

[17] D. R. Dalzell, "A comparison of paper mill refining equipment," *Tappi Journal*, vol. 44, no. 4, pp. 241–244, 1961.

[18] K. Ebeling, "A critical review of current theories for the refining of chemical pulps," in *Int. Symposium on Fundamental Concepts of Refining*, (Appleton, WI), pp. 1–34, 1980.

[19] E. Glasl, "Power saving in refining," *Paper Technology and Industry*, vol. 17, no. 5, pp. 200–203, 1976.

[20] P. J. Leider and A. H. Nissan, "Understanding the disk refiner; the mechanical treatment of the fibers," *Tappi J.*, vol. 60, no. 10, pp. 85–89, 1977.

[21] P. J. Leider and J. Rihs, "Understanding the disk refiner; the hydraulic behavior," *Tappi J.*, vol. 60, no. 9, pp. 98–102, 1977.

[22] W. A. Banks, "Design considerations and engineering characteristics of disc refiners," *Paper Technology and Industry*, vol. 8, no. 4, pp. 363–369, 1967.

[23] Finebar refining technology, "Introduction to stock prep refining." `http://www.aikawagroup.com/downloads/Training_Manual.pdf`, 2001.

[24] W. Batchelor, T. Lundin, and P. Fardim, "A method to estimate fiber trapping in low-consistency refining," *Tappi J.*, vol. 5, no. 8, p. 31, 2006.

[25] U.-B. Mohlin, "Refining intensity and gap clearance," in *9th International Refining Conference, Pira*, (Leatherhead, UK), 2006.

[26] U.-B. Mohlin and B. Roos, "Experiences from using a gap sensor in lc-refining," in *International Pulp Refining Seminar*, (Helsinki, Finland), pp. 37–40, June 2007.

[27] A. Luukkonen, *Development of a methodology to optimize low consistency refining of mechanical pulp*. PhD thesis, University of British Columbia, Vancouver, Canada, 2011.

[28] B. Dalpke and R. J. Kerekes, "The influence of fibre properties on the apparent yield stress of flocculated pulp suspensions," *Journal of pulp and paper science*, vol. 31, no. 1, pp. 39–43, 2005.

[29] C. Baker, "Refining and improved paper machine runnability," in *proceedings of 7th PIRA international refining conference & exhibition*, (Stockholm, Sweden), pp. 25–26, 2003.

[30] A. Mroziński, "Modelling of waste-paper stock treatment process in disc refiners," *Journal of POLISH CIMAC*, no. 3, pp. 113–119, 2010.

[31] P. Cooper and E. Reshotko, "Turbulent flow between a rotating disk and a parallel wall," *AIAA Journal*, vol. 13, pp. 573–578, 1975.

[32] A. P. Morse, "Assessment of laminar-turbulent transition in closed disc geometries," *Journal of Turbomachinary*, vol. 113, pp. 131–138, 1991.

[33] J. M. Owen and R. H. Rogers, *Flow and heat transfer in rotating-disc systems*. New York, NY (USA); John Wiley and Sons Inc., 1989.

[34] C. M. Vaughan, *A numerical investigation into the effect of an external flow field on the sealing of a rotor-stator cavity.* PhD thesis, University of Sussex, 1987.

[35] B. Launder, S. Poncet, and E. Serre, "Laminar, transitional, and turbulent flows in rotor-stator cavities," *Annual Review of Fluid Mechanics*, vol. 42, no. 1, pp. 229–248, 2010.

[36] J. W. Daily and R. E. Nece, "Chamber dimension effects on induced flow and frictional resistance of enclosed rotating disks," *Journal of Basic Engineering*, vol. 82, pp. 217–232, 1960.

[37] R. E. Nece and J. W. Daily, "Roughness effects on frictional resistance of enclosed rotating disks," *Journal of Basic Engineering*, vol. 82, pp. 553–562, 1960.

[38] J. W. Daily, W. D. Ernest, and V. V. Asbedian, *Enclosed Rotating Disks with Superposed Throughflow: Mean Steady and Periodic Unsteady Characteristics of the Induced Flow*. Department of Civil Engineering, Massachusetts Institute of Technology, 1964.

[39] J. M. Owen, "An approximate solution for the flow between a rotating and a stationary disk," in *ASME, paper No. 88-GT-293, 33rd Int. Gas Turbine Conference*, (Amsterdam), 1988.

[40] J. L. Goldstein and E. M. Sparrow, "Heat/mass transfer characteristics for flow in a corrugated wall channel," *ASME Transactions Journal of Heat Transfer*, vol. 99, pp. 187–195, 1977.

[41] J. E. O'Brien and E. M. Sparrow, "Corrugated duct heat transfer, pressure drop and flow visualization," *Transactions of the ASME, J. of Heat Transfer*, vol. 104, pp. 410–416, 1982.

[42] G. V. Wang and S. P. Vanka, "Convective heat transfer in periodic wavy passages," *International Journal of Heat and Mass Transfer*, vol. 38, no. 17, pp. 3219–3230, 1995.

[43] S. Selvarajan, E. G. Tulapurkara, and V. V. Ram, "A numerical study of flow through wavy-walled channels," *International journal for numerical methods in fluids*, vol. 26, pp. 519–531, 1998.

[44] I. J. Sobey, "On flow through furrowed channels; part i. calculated flow patterns," *J. Fluid Mech*, vol. 96, pp. 1–26, 1980.

[45] J. Nikuradse, *Laws of flow in rough pipes*. National Advisory Committee for Aeronautics Washington, 1950.

[46] E.-S. Zanoun, F. Durst, and H. Nagib, "Evaluating the law of the wall in two-dimensional fully developed turbulent channel flows," *Physics of Fluids*, vol. 15, pp. 3079–3089, 2003.

[47] J. Jiménez, "Turbulent flows over rough walls," *Annual Review of Fluid Mechanics*, vol. 36, pp. 173–196, 2004.

[48] S. Mokamati, J. A. Olson, D. M. Martinez, and R. W. Gooding, "Experimental study of a turbulent cross-flow near a two-dimensional rough wall with narrow apertures," *AIChE Journal*, vol. 54, no. 10, pp. 2516–2526, 2008.

[49] S. E. Coleman, V. I. Nikora, S. R. McLean, and E. Schlicke, "Spatially averaged turbulent flow over square ribs," *Journal of engineering mechanics*, vol. 133, no. 2, pp. 194–204, 2007.

[50] J. Cui, V. C. Patel, and C.-L. Lin, "Large-eddy simulation of turbulent flow in a channel with rib roughness," *International journal of heat and fluid flow*, vol. 24, no. 3, pp. 372–388, 2003.

[51] S. Leonardi, P. Orlandi, and R. A. Antonia, "Properties of d-and k-type roughness in a turbulent channel flow," *Physics of Fluids*, vol. 19, p. 125101, 2007.

[52] S. Leonardi, P. Orlandi, R. J. Smalley, L. Djenidi, and R. A. Antonia, "Direct numerical simulations of turbulent channel flow with transverse square bars on one wall," *Journal of Fluid Mechanics*, vol. 491, pp. 229–238, 2003.

[53] M. Shafiqul Islam, M. Kaminaga, R. Hino, and M. Monde, "Prediction of turbulent flow structure in a fully developed rib-roughened narrow rectangular channel," *Journal of Thermal Science*, vol. 18, no. 2, pp. 126–136, 2009.

[54] P. Orlandi, S. Leonardi, and R. A. Antonia, "Turbulent channel flow with either transverse or longitudinal roughness elements on one wall," *Journal of Fluid Mechanics*, vol. 561, no. 1, pp. 279–305, 2006.

[55] A. E. Perry, W. H. Schofield, and P. N. Joubert, "Rough wall turbulent boundary layers," *Journal of Fluid Mechanics*, vol. 37, pp. 383–413, 1968.

[56] R. L. Simpson, "A generalized correlation of roughness density effects on the turbulent boundary layer," *AIAA Journal*, vol. 11, pp. 242–244, 1973.

[57] I. Tani, "Turbulent boundary layer development over rough surfaces," in *Perspectives in turbulence studies*, pp. 223–249, Springer, 1987.

[58] P. R. Bandyopadhyay, "Rough-wall turbulent boundary layers in the transition regime," *Journal of Fluid Mechanics*, vol. 180, no. 1, pp. 231–266, 1987.

[59] A. Keshmiri, M. A. Cotton, and Y. Addad, "Numerical simulations of flow and heat transfer over rib-roughened surfaces," in *17th Annual conference of CFD society of Canada*, (Ottawa, Canada), 3rd-5th May 2009.

[60] A. K. Prasad and J. R. Koseff, "Reynolds number and end-wall effects on a lid-driven cavity flow," *Physics of Fluids A: Fluid Dynamics*, vol. 1, p. 208, 1989.

[61] M. D. Deshpande and P. N. Shankar, "Direct numerical simulation of a complex turbulent flow," *Current Science*, vol. 66, no. 10, pp. 767–770, 1994.

[62] F. Pan and A. Acrivos, "Steady flows in rectangular cavities," *Journal of Fluid Mechanics*, vol. 28, no. 4, pp. 643–655, 1967.

[63] M. Hellou and M. Coutanceau, "Cellular stokes flow induced by rotation of a cylinder in a closed channel," *Journal of Fluid Mechanics*, vol. 236, pp. 557–577, 1992.

[64] H. K. Moffatt, "Viscous and resistive eddies near a sharp corner," *Journal of Fluid Mechanics*, vol. 18, no. 1, pp. 1–18, 1964.

[65] Y.-F. Peng, Y.-H. Shiau, and R. R. Hwang, "Transition in a 2-d lid-driven cavity flow," *Computers & Fluids*, vol. 32, no. 3, pp. 337–352, 2003.

[66] C. W. Leong and J. M. Ottino, "Experiments on mixing due to chaotic advection in a cavity," *Journal of Fluid Mechanics*, vol. 209, no. 1, pp. 463–499, 1989.

[67] P. N. Shankar and M. D. Deshpande, "Fluid mechanics in the driven cavity," *Annual Review of Fluid Mechanics*, vol. 32, no. 1, pp. 93–136, 2000.

[68] L. P. Wittberg, M. Björkman, G. Khokhar, U.-B. Mohlin, and A. Dahlkild, "Flow conditions in the grooves of a low-consistency refiner," *Nordic Pulp and Paper Research Journal*, vol. 28, no. 2, pp. 173–183, 2012.

[69] G. Kohkar, *Numerical simulation of the flow in a disc refiner*. PhD thesis, KTH, 2011.

[70] S. Sriram, A. P. Deshpande, and S. Pushpavanam, "Analysis of spatiotemporal variations and flow structures in a periodically driven cavity," *ASME-Journal of Fluid Engineering*, vol. 128, no. 3, p. 413, 2006.

[71] M. J. Vogel, A. H. Hirsa, and J. M. Lopez, "Spatio-temporal dynamics of a periodically driven cavity flow," *Journal of Fluid Mechanics*, vol. 478, pp. 197–226, 2003.

[72] W.-L. Chien, H. Rising, and J. M. Ottino, "Laminar mixing and chaotic mixing in several cavity flows," *Journal of Fluid Mechanics*, vol. 170, no. 1, pp. 355–377, 1986.

[73] D. H. Page, J. Kosky, and D. Booth, "Some initial observations on the action of the beater," *BP & BIRA Bulletin October*, pp. 15–22, 1962.

[74] A. H. Nissan, "Possible mechanism for stapling on bars of disc refiners," *Tappi journal*, vol. 72, no. 1, pp. 132–133, 1989.

[75] V. N. Goncharov, "Force factors in a disk refiner and their effect on the beating process," *Bumazh. Prom*, vol. 5, pp. 12–14, 1971.

[76] T. S. Fox, R. S. Brodkey, and A. H. Nissan, "High-speed photography of stock transport in a disk refiner," *Tappi*, vol. 62, no. 3, pp. 55–58, 1979.

[77] T. S. Fox, "Inside a disk refiner," in *International Symposium on the Fundamentals Concepts of Refining, Appleton*, pp. 281–313, 1980.

[78] G. Kondora and D. Asendrych, "Flow modelling in a low consistency disc refiner," *Nordic Pulp and Paper*, vol. 28, pp. 119–130, March 2013.

[79] J. Antku and C. J. Ludwig, "Optimizing refiner plate bar height will reduce energy consumption," 1986.

[80] H. Siewert and H. Selder, "Energiewirtschaftliche aspekte der ganzstoffmahlung," *Vortragen auf der Informationstagung Energieverbrauch der Vereinigun Pack-und Wellpapappenpapiere*, 1976.

[81] C. J. Biermann, *Handbook of pulping and papermaking*. Academic press, 1996.

[82] D. Gorski, *ATMP Process: Improved Energy Efficiency in TMP Refining Utilizing Selective Wood Disintegration and Targeted Application of Chemicals*. PhD thesis, Mid Sweden University, 2011.

[83] J.-C. Roux and G. Joris, "Angular parameters beyond specific edge load," *TAPPSA Journal*, July 2005.

[84] A. Elahimehr, J. A. Olson, D. M. Martinez, and J. Heymer, "Estimating the area and number of bar crossings in refiner plates," *Nordic Pulp and Paper Journal*, 2013.

[85] A. Poullikkas, "Surface roughness effects on induced flow and frictional resistance of enclosed rotating disks," *Journal of fluids engineering*, vol. 117, no. 3, pp. 526–528, 1995.

[86] G. T. Csanady, *Theory of turbomachines*. McGraw-Hill, 1964.

[87] A. J. Stepanoff, *Centrifugal and Axial Flow Pumps*. 1962.

[88] O. M. Mesalhy, S. S. A. Aziz, and M. M. El-Sayed, "Flow and heat transfer over shallow cavities," *International Journal of Thermal Sciences*, vol. 49, no. 3, pp. 514–521, 2010.

[89] Fluent, "Fluent 6.2 Tutorial guide," 2005.

[90] Fluent, "Chapter 22. Using the solver," 2001.

[91] I. B. Celik, U. Ghia, and P. J. Roache, "Procedure for estimation and reporting of uncertainty due to discretization in cfd applications," *Journal of fluids Engineering-Transactions of the ASME*, vol. 130, no. 7, 2008.

[92] H. Friesing, "Measurement of the drag associated with recessed surfaces: cutouts of rectangular and elliptical planform," *Z.W.B.F.B., No. 628*, 1936.

[93] T. Timonen and J. Halttunen, "Effect of variations in a pulp flow on sampling and process measurements," in *In: Ilic, D., Borsic, M., & Butorac, J.(eds). XVII IMEKO World Congress. Metrology in the 3rd Millennium. Book of Summaries. Proceedings. June 22-27, 2003, Dubrovnik, Croatia. HMD-Croatian Metrology Society, Zagreb, Croatia.*

Appendix A

Experimental Details

In chapter 3, we measured the total no-load power in a 16″ low consistency refiner when running with water. As explained, first, we measured the mechanical power, $Power_M$, to know the losses due to the shaft and bearings friction. Thus, we ran refiner in the absence of water for different gap sizes and rotational speeds and recorded the values of $Power_M(G, \omega)$.

Plate 1: $BEL = 5.59 km/rev$		
$Gap(mm)$	$\omega(rpm)$	$Power_M(kW)$
2.02	205.74	0.37
2.04	496.82	0.41
1.99	597.3	0.58
1.99	798.78	0.93
1.98	1000.54	1.35
1.98	1202.11	1.85
1.98	1403.85	2.47
1.99	1504.86	2.81
9.09	498.85	0.49
9.08	599.4	0.66
9.08	800.87	1.05
9.09	1001.25	1.48
9.09	1194.44	1.97
9.09	1404.92	2.54
9.09	1505.57	2.85

Plate 3: $BEL = 0.99 km/rev$		
$Gap(mm)$	$\omega(rpm)$	$Power_M(kW)$
2.06	403.66	0.26
2.06	504.89	0.43
2.06	605.38	0.58
2.05	796.06	0.97
2.05	997.78	1.45
2.05	1098.91	1.67
2.04	1199.53	1.91
9.03	404.86	0.30
9.00	505.62	0.46
9.01	595.39	0.65
9.02	998.81	1.53
9.00	1099.4	1.79
9.00	1200.44	2.02
9.03	203.69	0.27
9.01	304.31	0.28

Table A.1: Values of mechanical power measured for Plate 1 and Plate 3 as shown in Figure 3.2

In the next step, the hydraulic power, $Power_n^*$, was calculated. So, refiner was run with water, while no flow was allowed to pump through the refiner and the values of $Power_{NL}$ were measured for various gap sizes and rotational speeds. By subtracting the mechanical power from the total no-load power measured in this step, the values of $Power_n^*$ were estimated.

$$Power_n^*(G,\omega) = Power_{NL}(G,\omega,Q=0) - Power_M(G,\omega) \tag{A.1}$$

Plate 1: $BEL = 5.59 km/rev$			
$\omega(rpm)$	$Gap(mm)$	$Power_{NL}(kW)$	$Power_n^*(kW)$
400.55	1.01	1.43	1.04
497.03	1.05	2.54	2.02
597.75	1.04	4.10	3.42
799.38	0.99	9.33	8.27
398.08	1.98	1.41	1.03
497.08	1.94	2.54	2.02
600.00	1.92	4.11	3.42
799.37	1.87	9.32	8.26
1000.91	1.98	17.77	16.27
1101.89	1.94	23.07	21.32
400.23	5.05	1.43	1.05
496.59	5.03	2.53	2.01
600.00	5.02	4.12	3.44
800.00	5.02	9.30	8.24
1000.80	4.98	17.48	15.98
1101.35	4.94	22.88	21.12
398.13	8.08	1.41	1.03
497.04	8.08	2.53	2.01
600.00	8.07	4.11	3.43
799.06	8.06	9.21	8.16
1000.60	8.03	17.59	16.09
1101.57	7.99	22.90	21.15
398.06	8.98	1.41	1.03
496.85	8.95	2.53	2.01
600.00	8.95	4.11	3.42
799.20	8.96	9.21	8.15
1000.73	8.93	17.52	16.02
1101.52	8.90	22.75	20.99

Table A.2: Values of hydraulic power measured for Plate 1

Plate 2: $BEL = 2.74km/rev$			
$\omega(rpm)$	$Gap(mm)$	$Power_{NL}(kW)$	$Power_n^*(kW)$
1396.63	8.96	38.72	43.71
1203.73	8.89	24.29	26.94
999.48	8.88	14.10	15.25
806.57	8.95	7.72	8.05
602.62	8.99	3.55	3.46
1394.00	8.00	38.50	43.46
1201.00	8.00	24.40	27.08
999.00	7.88	14.20	15.37
798.00	7.95	7.73	8.08
603.40	7.80	3.47	3.36
1396.00	5.00	38.40	43.33
1202.00	5.00	24.60	27.32
1001.00	5.00	14.14	15.29
799.00	5.02	7.76	8.11
602.00	4.80	3.47	3.37
1394.67	0.57	38.00	42.85
1202.19	0.51	24.89	27.67
999.08	0.48	14.09	15.23
797.42	0.49	7.80	8.17
601.83	0.45	3.50	3.40

Table A.3: Values of hydraulic power measured for Plate 2

Plate 3: $BEL = 0.99km/rev$			
$\omega(rpm)$	$Gap(mm)$	$Power_{NL}(kW)$	$Power_n^*(kW)$
502.88	0.96	2.42	1.90
604.82	0.93	4.00	3.32
799.40	0.86	8.62	7.77
503.77	1.92	2.41	1.88
607.46	1.94	4.07	3.42
802.00	1.89	8.71	8.04
997.14	1.84	16.01	15.21
1097.81	1.77	21.30	19.55
1198.74	1.74	27.41	25.40
502.98	5.02	2.41	1.88
605.89	5.01	4.03	3.41
805.64	4.97	8.60	8.08
996.35	4.92	16.14	15.24
1097.08	4.88	21.12	19.38
1198.08	4.90	27.20	25.19
502.59	8.04	2.42	1.90
607.53	8.04	4.04	3.35
805.25	8.02	8.60	8.17
995.99	7.97	16.03	15.04
1096.96	7.94	21.50	19.76
502.34	9.04	2.40	1.87
605.78	9.06	4.00	3.31
794.10	9.03	8.26	7.78
995.77	9.00	16.16	14.77
1096.69	8.97	21.06	19.32

Table A.4: Values of hydraulic power measured for Plate 3

Plate 4: $BEL = 2.01 km/rev$			
$\omega(rpm)$	$Gap(mm)$	$Power_{NL}(kW)$	$Power_n^*(kW)$
596.38	1.02	3.42	3.21
799.87	1.28	7.98	8.10
1003.82	1.15	14.98	15.76
1196.15	1.08	24.61	26.45
1400.04	0.97	37.89	41.29
1502.26	0.97	46.51	50.99
597.24	2.98	3.49	3.29
800.57	2.93	7.93	8.04
1004.62	3.11	15.08	15.88
1197.24	2.63	24.84	26.71
1401.00	2.57	38.47	41.96
1502.86	2.51	46.58	51.06
598.05	4.42	3.50	3.30
801.54	4.34	8.07	8.21
1005.12	4.26	15.24	16.06
1197.66	4.19	25.21	27.15
1401.33	4.13	38.79	42.33
1503.41	4.08	48.10	52.84
600.00	4.86	3.54	3.34
802.05	4.81	8.04	8.16
1005.73	4.76	15.21	16.03
1197.96	4.67	25.20	27.13
1402.11	4.64	38.70	42.23
1503.63	4.59	48.11	52.85
599.17	7.86	3.56	3.36
802.63	7.83	8.04	8.17
1004.00	7.80	15.25	16.07
1198.58	7.75	25.26	27.20
1403.11	7.68	38.84	42.39
1504.30	7.65	48.09	52.82
600.05	8.93	3.58	3.38
803.35	8.88	8.04	8.17
1005.00	8.83	15.21	16.02
1199.56	8.78	25.14	27.05
1403.30	8.72	38.80	42.34
1505.62	8.72	48.09	52.83

Table A.5: Values of hydraulic power measured for Plate 4

Plate 5: $BEL = 10.1km/rev$			
$\omega(rpm)$	$Gap(mm)$	$Power_{NL}(kW)$	$Power_n^*(kW)$
591.67	8.98	3.77	3.10
680.73	9.07	5.65	4.82
793.05	9.06	8.45	7.41
880.59	9.03	11.57	10.35
984.01	8.99	15.77	14.30
492.96	7.99	2.41	1.89
591.63	8.03	3.79	3.12
680.66	7.95	5.70	4.87
792.88	7.95	8.52	7.48
880.58	8.01	11.70	10.47
983.82	7.93	15.92	14.46
680.04	7.12	5.74	4.91
792.87	6.95	8.71	7.67
880.37	7.04	11.78	10.56
983.66	7.00	15.77	14.31
492.75	5.93	2.39	1.88
592.08	6.06	3.89	3.22
679.60	5.97	5.74	4.92
792.78	6.01	8.75	7.71
983.24	6.10	15.88	14.42
492.49	5.00	2.38	1.87
591.78	4.99	3.90	3.23
680.25	5.11	5.60	4.78
792.46	5.00	8.62	7.58
881.68	5.00	11.50	10.27
983.42	5.16	15.75	14.29
492.28	2.05	2.38	1.86
592.48	2.07	3.83	3.16
681.37	2.04	5.66	4.84
792.09	1.98	8.70	7.66
983.59	2.01	15.32	13.86
491.80	0.92	2.37	1.85
592.75	1.09	3.81	3.14
682.05	1.01	5.75	4.92
791.92	1.00	8.80	7.76
882.18	1.10	11.55	10.32
983.40	1.04	15.62	14.16

Table A.6: Values of hydraulic power measured for Plate 5

Plate 6: $BEL = 12.9km/rev$			
$\omega(rpm)$	$Gap(mm)$	$Power_{NL}(kW)$	$Power_n^*(kW)$
495.21	9.00	2.23	1.72
593.56	9.00	3.81	3.14
680.84	9.05	5.63	4.81
793.23	9.03	8.15	7.11
882.94	9.07	11.08	9.85
983.88	9.07	14.80	13.34
495.21	8.00	2.24	1.72
593.27	8.02	3.80	3.13
680.92	8.02	5.64	4.81
793.12	8.09	8.15	7.11
883.20	7.97	11.08	9.84
983.73	8.02	14.79	13.33
495.21	6.00	2.25	1.74
593.19	6.03	3.84	3.16
793.30	6.02	8.27	7.22
983.49	6.06	14.90	13.44
495.21	4.96	2.26	1.74
593.04	4.99	3.87	3.19
793.39	5.02	8.24	7.20
983.50	5.09	15.06	13.60
495.21	2.98	2.25	1.73
592.91	2.53	3.78	3.10
983.65	2.99	15.06	13.60
495.21	2.03	2.26	1.74
592.95	1.92	3.83	3.16
793.46	2.09	8.27	7.22
983.02	2.05	15.02	13.56
495.21	1.09	2.25	1.73
592.65	1.03	3.84	3.17
793.48	1.01	8.17	7.13

Table A.7: Values of hydraulic power measured for Plate 6

Finally, we measured $Power_{NL}$ for different gap sizes, rotational speeds and flow rates when there was flow pumped through the refiner and by subtracting the mechanical power, $Power_n$ which covers both hydraulic and pumping powers, was measured.

$$Power_n(G, \omega, Q) = Power_{NL}(G, \omega, Q) - Power_M(G, \omega) \tag{A.2}$$

where $Power_n = Power_n^* + Power_P$

Table A.8: Values of $Power_{NL}$ and $Power_n$ measured for Plate 1

Plate 1: $BEL = 5.59 km/rev$				
$\omega(rpm)$	$FlowRate(lpm)$	$Gap(mm)$	$Power_{NL}(kW)$	$Power_n(kW)$
596.07	503.79	8.06	4.44	3.76
596.46	509.97	9.05	4.43	3.76
798.21	518.23	5.00	10.13	9.08
593.93	600.21	0.98	4.99	4.32
594.52	604.84	2.03	4.93	4.26
605.85	625.03	3.98	4.99	4.30
596.06	600.09	5.04	4.81	4.13
595.67	596.97	8.05	4.52	3.84
597.20	589.20	9.05	4.57	3.89
797.85	619.80	1.98	10.83	9.78
796.35	605.78	3.91	10.44	9.39
798.31	592.43	5.01	10.27	9.21
796.95	595.00	8.05	9.92	8.87
798.81	591.94	9.04	9.97	8.91
492.89	817.31	1.17	3.23	2.72
504.75	807.60	2.13	3.29	2.75
504.83	796.51	4.01	3.29	2.76
495.39	807.53	5.07	3.10	2.58
494.83	818.79	8.09	3.00	2.48
497.71	803.59	9.07	3.08	2.56
593.80	791.33	1.11	5.24	4.56
594.55	804.77	2.10	5.14	4.47
594.64	795.68	4.00	5.07	4.39
596.09	802.48	5.07	5.00	4.32
607.13	805.29	8.10	5.13	4.43
598.49	805.33	9.10	4.89	4.21
796.24	796.44	1.05	11.32	10.27
797.72	809.70	2.02	11.17	10.12

Continued on next page

Table A.8 – continued from previous page

$\omega(rpm)$	$FlowRate(lpm)$	$Gap(mm)$	$Power_{NL}(kW)$	$Power_n(kW)$
800.14	790.81	3.97	11.11	10.06
797.71	795.45	5.06	10.53	9.48
797.55	790.19	8.10	10.32	9.27
800.27	790.96	9.10	10.36	9.30
504.26	1015.02	1.23	3.59	3.06
504.96	1008.62	2.17	3.55	3.02
504.97	1005.56	4.06	3.34	2.80
506.06	1004.52	5.11	3.41	2.88
505.84	998.41	8.14	3.35	2.82
498.02	994.45	9.12	3.23	2.71
605.07	1007.73	1.20	5.61	4.92
605.54	996.40	2.14	5.58	4.88
594.73	999.93	4.05	5.28	4.61
595.87	1009.94	5.09	5.20	4.52
595.47	1007.21	8.13	5.13	4.45
598.63	1006.06	9.12	5.11	4.43
795.80	1013.27	1.12	11.84	10.79
797.17	991.96	2.05	11.70	10.65
801.25	989.61	4.04	11.34	10.28
797.75	992.86	5.10	11.09	10.03
804.45	1008.19	8.13	11.09	10.03
800.07	1005.48	9.13	11.09	10.04
998.86	994.51	8.12	19.93	18.44
1001.97	993.93	9.12	19.99	18.49
504.75	1209.49	2.20	3.59	3.05
505.18	1201.02	4.08	3.56	3.03
506.00	1201.33	5.13	3.57	3.03
505.80	1203.27	8.13	3.54	3.00
498.55	1210.66	9.13	3.36	2.84
605.41	1183.18	1.23	5.95	5.25
605.56	1199.61	2.20	5.79	5.09
595.00	1192.13	4.07	5.45	4.78
595.85	1208.15	5.12	5.41	4.74
595.60	1211.38	8.13	5.25	4.57
599.25	1194.59	9.14	5.24	4.56
795.84	1194.55	1.14	12.07	11.03
798.41	1210.19	2.17	12.20	11.15
802.20	1204.71	4.06	11.72	10.66
797.65	1209.22	5.14	11.23	10.18

Continued on next page

Table A.8 – continued from previous page

$\omega(rpm)$	$FlowRate(lpm)$	$Gap(mm)$	$Power_{NL}(kW)$	$Power_n(kW)$
797.25	1217.52	8.14	11.19	10.14
800.38	1212.14	9.15	11.19	10.14
999.03	1194.25	5.14	20.96	19.46
999.16	1191.04	8.15	20.59	19.09
1002.14	1189.98	9.17	20.59	19.08

Table A.9: Values of $Power_{NL}$ and $Power_n$ measured for Plate 2

Plate 2: $BEL = 2.74km/rev$				
$\omega(rpm)$	$FlowRate(lpm)$	$Gap(mm)$	$Power_{NL}(kW)$	$Power_n(kW)$
1198.82	1404.16	5.15	33.42	31.41
1001.93	1402.42	9.05	19.94	18.43
994.61	1402.26	5.02	20.62	19.14
997.94	1401.92	4.08	21.05	19.56
797.50	1408.25	9.06	10.83	9.78
802.19	1416.15	5.02	11.36	10.30
801.89	1398.76	4.07	11.50	10.44
1160.72	1196.86	6.12	29.50	27.60
1197.83	1201.25	5.03	32.63	30.62
1001.29	1210.33	9.04	19.28	17.78
1002.35	1196.66	8.15	19.19	17.68
999.69	1198.65	6.01	19.58	18.08
1005.41	1197.34	5.03	20.34	18.82
1000.26	1196.05	4.05	20.43	18.93
797.39	1198.27	9.03	10.52	9.47
798.26	1199.15	8.03	10.62	9.56
806.74	1196.24	6.01	10.88	9.81
801.88	1198.70	5.03	11.09	10.03
796.48	1199.07	4.07	11.01	9.96
604.55	1205.14	9.02	5.01	4.32
602.59	1194.14	8.03	5.01	4.32
602.70	1196.70	6.01	5.09	4.40
602.02	1198.51	5.00	5.12	4.43
1195.32	1006.82	8.10	31.15	29.14
1204.06	1008.42	6.10	31.48	29.46
1198.72	1007.93	5.01	32.28	30.26

Continued on next page

Table A.9 – continued from previous page

$\omega(rpm)$	$FlowRate(lpm)$	$Gap(mm)$	$Power_{NL}(kW)$	$Power_n(kW)$
1205.22	1011.40	4.03	32.53	30.50
1198.31	996.94	1.98	33.80	31.79
1000.88	999.26	9.02	18.93	17.43
1002.57	1000.69	8.11	18.94	17.44
999.96	1013.31	6.12	19.60	18.10
994.42	1008.26	5.04	19.68	18.19
1005.46	1003.02	4.14	20.62	19.11
796.98	1002.16	9.01	10.03	8.98
798.53	1006.62	8.11	9.99	8.93
796.92	999.51	6.11	10.36	9.31
802.13	999.50	5.05	10.76	9.70
799.02	998.80	4.20	10.80	9.75
604.17	996.94	9.01	4.80	4.11
600.57	1000.85	8.10	4.74	4.05
603.01	1004.75	6.11	4.75	4.06
598.38	999.19	5.05	4.89	4.21
600.17	1004.59	4.21	4.99	4.30
1204.21	789.36	6.05	31.31	29.28
1197.55	807.15	4.98	31.42	29.41
1206.73	805.56	3.89	33.04	31.00
1000.62	804.42	8.98	18.40	16.89
1002.90	799.37	8.10	18.41	16.90
999.87	804.59	6.09	18.53	17.03
1005.13	796.65	5.02	19.45	17.94
1002.88	801.84	3.98	19.71	18.20
796.54	797.67	8.98	10.05	9.00
798.91	806.34	8.09	10.07	9.02
807.09	810.92	6.10	10.06	8.99
801.04	804.84	5.04	10.47	9.41
798.87	795.20	4.08	10.50	9.45
595.31	798.95	8.10	4.48	3.80
603.01	799.42	6.10	4.57	3.88
596.83	800.80	5.06	4.50	3.83
595.42	797.76	4.13	4.73	4.05
1000.60	606.42	6.02	18.50	16.99
1004.12	601.22	4.86	18.92	17.41
1003.74	604.02	4.10	19.24	17.73
800.11	606.97	4.99	10.03	8.98
596.55	609.06	5.03	4.42	3.74

Continued on next page

Table A.9 – continued from previous page

$\omega(rpm)$	$FlowRate(lpm)$	$Gap(mm)$	$Power_{NL}(kW)$	$Power_n(kW)$
595.86	605.26	4.10	4.56	3.88

Table A.10: Values of $Power_{NL}$ and $Power_n$ measured for Plate 3

Plate 3: $BEL = 0.99km/rev$				
$\omega(rpm)$	$FlowRate(lpm)$	$Gap(mm)$	$Power_{NL}(kW)$	$Power_n(kW)$
504.39	610.34	5.01	2.84	2.31
502.04	611.42	8.09	2.79	2.26
599.02	616.85	2.02	4.57	3.89
605.90	611.91	5.01	4.64	3.95
602.94	608.25	8.06	4.39	3.70
602.91	598.18	9.12	4.29	3.60
800.77	621.36	1.96	9.50	8.45
805.28	612.67	8.05	9.57	8.50
793.98	595.72	9.11	9.04	7.99
503.66	796.40	2.06	3.05	2.52
501.88	806.46	8.08	2.84	2.31
495.69	798.25	9.13	2.75	2.23
599.25	796.51	2.02	4.80	4.12
597.17	806.82	5.02	4.67	3.99
602.79	807.12	8.09	4.59	3.90
603.40	806.98	9.15	4.53	3.84
800.89	811.76	1.98	9.93	8.88
798.90	796.38	4.99	10.02	8.97
804.88	808.37	8.09	9.84	8.77
793.62	799.86	9.14	9.41	8.37
995.67	815.94	8.09	17.62	16.13
502.37	1007.35	8.09	3.07	2.54
495.71	1005.54	9.16	2.89	2.37
601.63	1016.19	2.11	5.08	4.39
592.02	996.31	8.11	4.71	4.04
603.27	999.74	9.17	4.72	4.03
801.82	990.45	2.03	10.29	9.23
799.22	1002.95	5.04	10.24	9.19
794.21	1008.38	8.12	10.20	9.16
793.81	991.95	9.17	9.73	8.69

Continued on next page

Table A.10 – continued from previous page

$\omega(rpm)$	$FlowRate(lpm)$	$Gap(mm)$	$Power_{NL}(kW)$	$Power_n(kW)$
500.24	1188.00	2.12	3.30	2.78
508.58	1191.95	5.07	3.32	2.78
600.75	1198.22	2.12	5.22	4.53
801.82	1217.66	2.10	10.73	9.67
799.49	1216.07	5.07	10.80	9.75

Table A.11: Values of $Power_{NL}$ and $Power_n$ measured for Plate 4

Plate 4: $BEL = 2.01 km/rev$				
$\omega(rpm)$	$FlowRate(lpm)$	$Gap(mm)$	$Power_{NL}(kW)$	$Power_n(kW)$
596.08	610.42	2.22	4.50	3.82
795.77	603.80	4.39	9.84	8.80
797.32	596.91	5.24	9.71	8.66
796.74	605.55	8.21	9.26	8.21
796.36	604.48	9.06	9.28	8.23
1000.33	601.21	4.31	18.58	17.08
1001.87	600.55	5.18	18.10	16.60
1197.96	591.12	2.18	31.63	29.62
1205.17	601.51	4.23	30.50	28.47
1195.32	597.47	5.12	29.46	27.45
1402.95	590.55	2.10	48.37	45.76
1398.76	607.05	4.12	46.68	44.08
604.04	811.95	2.01	4.69	4.00
602.97	790.87	4.07	4.55	3.86
595.43	799.82	4.96	4.44	3.76
803.77	798.51	4.02	10.50	9.44
799.35	795.59	4.93	10.10	9.05
798.03	795.08	8.04	9.62	8.56
796.74	798.78	9.09	9.58	8.53
1004.11	798.35	4.88	19.12	17.61
1001.68	798.52	9.07	17.66	16.16
1195.24	809.67	2.11	31.92	29.92
1206.00	798.77	3.93	31.80	29.77
1201.09	807.44	4.83	30.80	28.78
604.95	1010.60	2.15	4.94	4.25
604.04	1007.12	4.03	4.68	3.99

Continued on next page

Table A.11 – continued from previous page

$\omega(rpm)$	$FlowRate(lpm)$	$Gap(mm)$	$Power_{NL}(kW)$	$Power_n(kW)$
595.21	1001.48	4.97	4.47	3.79
1001.51	999.55	4.20	19.92	18.41
1004.34	1009.51	4.94	19.69	18.18
1002.49	1005.34	8.07	18.51	17.00
1001.45	1002.51	9.11	18.46	16.96
1194.50	1009.50	4.12	32.36	30.36
1197.50	998.06	4.90	31.46	29.45
1195.10	1003.98	9.10	29.72	27.72
605.38	1190.08	2.18	5.16	4.47
604.05	1203.31	4.03	4.94	4.25
596.32	1198.09	5.02	4.74	4.07
604.33	1196.02	9.11	4.72	4.03
798.35	1196.36	7.95	10.45	9.40
797.30	1204.15	9.11	10.39	9.33
994.12	1209.60	5.02	19.70	18.21
1003.19	1214.40	7.96	19.49	17.98
1001.82	1193.72	9.12	19.22	17.71
1195.43	1195.39	3.96	33.40	31.40
1198.38	1205.51	4.98	32.67	30.65
1199.39	1195.37	7.96	31.63	29.62
1195.95	1200.45	9.13	31.13	29.13
1401.61	1200.61	1.95	53.17	50.56
1400.38	1203.49	4.09	51.04	48.43
1402.50	1211.61	4.94	49.58	46.97
1399.91	1196.17	9.13	47.87	45.27
1606.55	1191.57	1.91	75.13	71.84
1605.45	1191.50	4.07	72.93	69.64
1595.73	1197.47	4.94	69.80	66.55
596.16	1400.04	2.01	5.09	4.41
593.83	1400.15	4.25	4.99	4.32
596.22	1402.36	5.04	4.97	4.29
604.82	1409.85	7.96	4.89	4.19
604.25	1411.11	9.11	4.97	4.28
797.38	1396.98	9.13	10.72	9.67
1002.84	1401.74	7.98	19.99	18.48
1001.93	1408.91	9.17	19.91	18.41
1195.77	1395.91	4.24	33.94	31.94
1198.44	1414.89	5.04	33.66	31.64
1195.85	1401.46	7.99	31.97	29.97

Continued on next page

Table A.11 – continued from previous page

$\omega(rpm)$	$FlowRate(lpm)$	$Gap(mm)$	$Power_{NL}(kW)$	$Power_n(kW)$
1195.71	1407.16	9.17	32.11	30.10
1400.34	1395.50	4.17	51.94	49.34
1402.76	1407.59	5.03	51.51	48.90
1400.56	1395.14	8.22	48.37	45.77
1399.99	1398.12	9.18	48.19	45.58
1607.11	1399.46	1.92	78.93	75.64
1605.44	1399.50	4.15	74.47	71.19
1607.63	1396.41	5.16	73.87	70.58
1604.80	1400.05	8.24	71.00	67.72

Table A.12: Values of $Power_{NL}$ and $Power_n$ measured for Plate 5

Plate 5: $BEL = 10.1km/rev$				
$\omega(rpm)$	$FlowRate(lpm)$	$Gap(mm)$	$Power_{NL}(kW)$	$Power_n(kW)$
592.26	507.09	0.98	4.43	3.76
592.20	486.65	2.04	4.36	3.69
592.12	474.91	2.59	4.33	3.66
591.89	468.51	3.04	4.30	3.63
592.03	499.54	4.09	4.28	3.61
591.67	493.75	5.03	4.29	3.62
591.58	494.13	5.99	4.26	3.59
591.60	498.02	8.00	4.25	3.58
591.68	500.61	9.00	4.23	3.56
690.57	586.10	0.98	6.82	5.98
690.96	562.98	1.86	6.83	5.99
691.37	550.47	2.46	6.61	5.77
690.03	539.32	2.93	6.61	5.77
691.96	522.20	4.08	6.54	5.70
691.58	512.84	5.01	6.46	5.61
691.50	510.35	6.04	6.37	5.53
692.64	517.41	8.01	6.36	5.51
691.74	520.43	8.98	6.36	5.51
595.56	587.31	1.15	4.61	3.93
595.90	594.90	2.04	4.60	3.92
596.41	594.30	2.53	4.58	3.90
596.03	591.34	3.10	4.47	3.80

Continued on next page

Table A.12 – continued from previous page

$\omega(rpm)$	$FlowRate(lpm)$	$Gap(mm)$	$Power_{NL}(kW)$	$Power_n(kW)$
596.76	583.42	4.11	4.51	3.83
596.27	595.76	5.20	4.32	3.64
596.30	598.03	6.59	4.33	3.65
596.06	599.60	7.88	4.32	3.64
596.27	601.16	9.17	4.32	3.64
694.90	608.01	8.12	6.56	5.70
694.50	609.52	8.96	6.53	5.68
797.32	615.48	1.10	9.81	8.75
796.99	620.89	2.07	10.14	9.09
796.57	608.82	2.49	10.03	8.98
796.50	608.71	3.09	10.03	8.98
796.64	611.52	4.05	9.81	8.76
796.52	600.76	5.11	9.62	8.57
796.55	597.47	5.97	9.59	8.54
796.44	605.41	7.96	9.48	8.43
796.19	611.11	9.04	9.45	8.40
882.73	656.59	1.00	13.29	12.05
982.93	662.31	3.07	18.25	16.79
983.00	638.49	3.96	18.18	16.72
982.65	633.90	4.77	18.09	16.63
982.70	622.00	5.86	17.66	16.20
982.63	625.01	8.10	17.40	15.94
983.06	631.99	8.89	17.40	15.94
892.95	682.14	1.02	13.95	12.70
892.51	692.25	2.55	13.82	12.57
892.27	704.63	2.95	13.88	12.62
892.48	687.68	4.07	13.72	12.47
892.34	685.28	5.04	13.47	12.21
892.51	683.76	6.03	13.50	12.25
892.56	692.82	8.12	13.39	12.14
892.64	698.81	8.97	13.40	12.15
984.23	713.55	1.01	17.70	16.24
592.12	801.64	1.07	4.75	4.08
592.08	786.80	2.07	4.70	4.03
592.56	800.62	2.67	4.70	4.03
592.56	801.17	2.99	4.67	4.00
592.49	799.41	5.05	4.47	3.80
592.76	802.54	6.09	4.47	3.80
593.13	807.24	7.97	4.48	3.81

Continued on next page

Table A.12 – continued from previous page

$\omega(rpm)$	$FlowRate(lpm)$	$Gap(mm)$	$Power_{NL}(kW)$	$Power_n(kW)$
593.21	807.71	8.98	4.47	3.80
684.37	832.55	1.04	7.01	6.18
682.14	815.21	2.08	6.86	6.03
682.44	805.38	2.57	6.81	5.98
681.76	796.71	3.15	6.70	5.88
682.10	792.97	3.99	6.70	5.87
682.21	792.20	5.10	6.51	5.68
682.13	796.04	6.05	6.41	5.58
681.61	800.52	8.07	6.38	5.55
681.04	802.96	9.00	6.33	5.50
791.58	791.45	2.55	10.28	9.25
788.39	781.41	3.16	10.13	9.10
790.67	794.83	4.00	10.05	9.01
790.40	791.90	4.93	9.57	8.53
785.29	792.26	5.98	9.43	8.40
786.81	796.21	8.00	9.36	8.33
787.38	798.39	8.99	9.32	8.29
892.77	796.10	2.54	14.21	12.96
893.17	823.05	3.17	14.20	12.95
893.01	808.85	3.95	14.12	12.86
892.83	801.54	5.01	13.27	12.02
892.95	781.24	6.10	13.21	11.96
892.86	786.32	8.15	13.21	11.96
892.74	784.22	8.99	13.21	11.96
983.25	787.73	2.05	18.70	17.24
983.20	790.30	2.49	18.61	17.15
983.19	791.16	3.00	18.50	17.04
982.80	763.99	4.19	18.16	16.70
982.39	789.95	5.08	17.67	16.21
982.48	788.47	6.02	17.46	16.00
982.80	796.84	8.15	17.38	15.92
982.41	802.00	9.00	17.28	15.82

Table A.13: Values of $Power_{NL}$ and $Power_n$ measured for Plate 6

Plate 6: $BEL = 12.9km/rev$				
$\omega(rpm)$	$FlowRate(lpm)$	$Gap(mm)$	$Power_{NL}(kW)$	$Power_n(kW)$
588.78	317.45	8.03	3.77	3.11
588.96	320.71	9.08	3.78	3.12
588.63	360.05	9.07	3.81	3.15
785.02	426.57	7.97	8.30	7.28
785.86	428.00	9.01	8.31	7.28
489.02	495.79	5.00	2.43	1.92
578.85	504.17	8.07	3.73	3.08
578.58	509.12	9.11	3.73	3.08
682.32	514.50	7.91	5.88	5.06
681.47	517.46	9.05	5.79	4.96
787.16	546.10	1.00	9.05	8.02
789.86	499.40	5.05	8.56	7.53
785.79	501.44	6.07	8.43	7.40
785.98	509.16	7.97	8.45	7.42
787.32	512.89	8.99	8.47	7.44
892.07	582.00	1.23	12.55	11.30
892.08	534.77	2.44	12.71	11.46
891.78	517.81	2.98	12.64	11.39
891.75	500.18	4.92	12.05	10.80
589.29	594.57	3.11	4.12	3.46
589.46	597.13	4.96	4.05	3.39
589.20	597.45	6.08	4.01	3.34
589.21	599.31	7.97	4.01	3.34
589.07	601.10	9.01	4.08	3.41
681.65	618.23	7.92	5.93	5.11
682.39	615.43	9.01	5.92	5.10
791.71	609.63	1.14	9.27	8.23
791.38	596.92	5.02	8.70	7.66
790.23	600.88	6.00	8.68	7.64
791.15	606.57	7.93	8.70	7.66
790.95	608.06	9.02	8.71	7.67
881.12	657.12	1.10	12.58	11.36
881.16	620.11	2.51	12.44	11.21
881.34	609.80	2.92	12.37	11.15
880.95	600.13	4.03	11.86	10.64
880.85	597.82	4.94	11.67	10.44

Continued on next page

Table A.13 – continued from previous page

$\omega(rpm)$	$FlowRate(lpm)$	$Gap(mm)$	$Power_{NL}(kW)$	$Power_n(kW)$
880.85	601.11	5.95	11.76	10.53
880.74	610.55	7.92	11.72	10.50
881.42	617.08	9.04	11.72	10.50
982.19	610.61	2.15	16.61	15.15
982.26	580.18	2.97	16.75	15.30
982.40	579.79	4.03	16.18	14.73
982.46	587.92	5.09	16.08	14.62
982.02	593.13	6.01	15.91	14.45
589.03	820.26	5.97	4.20	3.53
589.01	815.42	8.03	4.18	3.51
588.77	816.31	9.07	4.18	3.51
689.65	799.36	8.01	6.21	5.36
689.40	799.17	9.02	6.21	5.37
785.76	829.87	1.06	9.50	8.48
786.75	804.84	2.44	9.49	8.46
786.19	803.92	2.97	9.24	8.21
789.61	805.84	4.02	8.94	7.91
786.78	809.50	4.98	8.88	7.85
788.80	811.52	6.07	8.86	7.83
789.22	813.76	7.98	8.81	7.78
787.28	813.31	9.05	8.81	7.78
881.06	812.04	1.05	12.99	11.76
880.65	783.64	1.97	12.92	11.70
880.95	790.12	2.50	12.93	11.70
880.45	788.08	2.98	12.56	11.33
881.23	789.03	6.02	11.94	10.71
880.68	791.23	8.05	11.84	10.61
881.09	793.58	9.01	11.84	10.61
981.40	814.55	2.11	17.32	15.87
981.59	787.19	3.10	16.71	15.25
981.48	778.92	3.92	16.30	14.84
981.66	777.03	4.94	16.25	14.79
981.79	775.78	6.08	16.29	14.83
981.72	786.13	7.94	16.28	14.82

Appendix B

Comparison of Water and Pulp

In addition to water, we measured the values of no-load power for our 16″ LC refiner when running by pulp with two different consistencies of $C = 1.5\%$ and 3.5% to be able to compare the no-load powers measured by water and mechanical pulp:

(a) Values of hydraulic power

Plate 2: $BEL = 2.74km/rev$					
Water		Pulp, $C = 1.5\%$		Pulp, $C = 3.5\%$	
$\omega(rpm)$	$Power_n^*(kW)$	$\omega(rpm)$	$Power_n^*(kW)$	$\omega(rpm)$	$Power_n^*(kW)$
1203.73	26.71	583.37	3.21	608.08	3.42
999.48	16.32	784.90	7.82	700.93	5.00
806.57	7.98	985.94	14.69	796.98	8.03
602.62	3.43	1187.27	25.63	997.76	15.11
500.52	2.15			1197.56	25.62

(b) Values of $Power_n$

Plate 2: $BEL = 2.74km/rev$					
Water		Pulp, $C = 1.5\%$		Pulp, $C = 3.5\%$	
$\omega(rpm)$	$Power_n(kW)$	$\omega(rpm)$	$Power_n(kW)$	$\omega(rpm)$	$Power_n(kW)$
1000.78	15.48	794.23	7.73	603.47	3.10
796.48	7.92	985.18	14.55	701.20	5.20
603.79	3.26	1199.53	24.57	809.20	7.64
501.81	1.57			1003.75	14.26

Table B.1: Values of $Power_n^*$ and $Power_n$ measured for water and pulp with consistencies of 1.5% and 3.5% for Plate 2 when $Q = 600lpm$

Appendix C

Pulp Properties

In chapter 3, we also measured some pulp properties for the pulp suspension of $C = 3.5\%$ to determine the starting point of refiner loading (G_l). The chosen properties were freeness, fibre length and tensile:

Plate 2: $BEL = 2.74 km/rev$, $C = 3.5\%$ and $Q = 500 lpm$					
$\omega = 800 rpm$		$\omega = 1000 rpm$		$\omega = 1200 rpm$	
Gap (mm)	$Freeness$ $(mlCSF)$	Gap (mm)	$Freeness$ $(mlCSF)$	Gap (mm)	$Freeness$ $(mlCSF)$
8.93	385.9	9.02	385.9	8.96	385.9
6.07	385.9	6.07	385.9	6.02	385.9
2.48	375.2	2.55	372.5	2.50	370.7
1.49	368.4	1.48	366	1.29	364.2
0.76	363	0.73	348.2	0.69	350.35
0.28	357.3	0.30	307.2	0.30	288.65
0.09	335.6	0.09	271.85	0.12	246.6
0.02	293.7	0.04	255.6	0.01	208.45

Table C.1: Freeness of fibres at various gap sizes for Plate 2 when $Q = 500 lpm$ as shown in Figure 3.6

Plate 2: $BEL = 2.74km/rev$, $C = 3.5\%$ and $Q = 500lpm$					
$\omega = 800rpm$		$\omega = 1000rpm$		$\omega = 1200rpm$	
Gap (mm)	$FibreLength$ (mm)	Gap (mm)	$FibreLength$ (mm)	Gap (mm)	$FibreLength$ (mm)
8.93	1.93	9.02	1.93	8.97	1.93
6.07	1.93	6.07	1.93	6.02	1.928
2.48	1.90	2.55	1.93	2.50	1.95
1.49	1.81	1.48	1.92	1.29	1.87
0.76	1.76	0.73	1.89	0.70	1.82
0.28	1.73	0.30	1.83	0.30	1.58
0.09	1.64	0.09	1.46	0.12	1.30
0.02	1.55	0.04	1.37	0.01	1.24

Table C.2: Length-weighted (L_W) average length of fibres at various gap sizes for pulp suspension of $C = 3.5\%$ for Plate 2 when $Q = 500lpm$ as shown in Figure 3.7

Plate 2: $BEL = 2.74km/rev$, $C = 3.5\%$ and $Q = 500lpm$					
$\omega = 800rpm$		$\omega = 1000rpm$		$\omega = 1200rpm$	
Gap (mm)	$TensileIndex$ $(N.m/g)$	Gap (mm)	$TensileIndex$ $(N.m/g)$	Gap (mm)	$TensileIndex$ $(N.m/g)$
8.93	38.28	9.02	38.28	8.97	38.28
6.07	38.28	6.07	38.28	6.02	38.28
2.48	38.29	2.55	37.78	2.50	38.65
1.49	38.20	1.48	39.34	1.29	41.03
0.76	42.20	0.73	39.42	0.70	40.17
0.28	41.46	0.30	39.66	0.30	42.87
0.09	40.26	0.09	41.56	0.12	41.44
0.02	41.63	0.04	42.64	0.01	43.71

Table C.3: Tensile index at various gap sizes for pulp suspension of $C = 3.5\%$ for Plate 2 when $Q = 500lpm$ as shown in Figure 3.8